Chasing charge transfer in organic systems

by

Daniel E. Wilcox

A dissertation submitted in partial fulfillment
of the requirements for the degree of
Doctor of Philosophy
(Physics)
in the University of Michigan
2015

Doctoral Committee:

Associate Professor Jennifer P. Ogilvie, Chair
Professor Stephen R. Forrest
Professor Eitan Geva
Professor Mark E. Newman
Associate Professor Max Shtein

2015

Acknowledgments

My wife Carolyn has been tirelessly supportive throughout my graduate career. I couldn't have gotten anywhere without her; I continue to depend on her every day. I cannot begin to describe my awe for her loving kindness and long-term supportiveness. My research advisor Jennifer Ogilvie has also been unfailingly encouraging. I am deeply grateful for her commitment to her students, her writing skills, her scientific insight, and her vision for the future.

TABLE OF CONTENTS

LIST OF FIGURES

LIST OF TABLES

LIST OF APPENDICES

LIST OF ABBREVIATIONS

2DES two-dimensional electronic spectroscopy

BBO β-barium borate

BPhen bathophenanthroline

CEP carrier-envelope phase

CRT chirp reversal technique

DBP tetraphenyldibenzoperiflanthene

DFG difference frequency generation

DOPA degenerate optical parametric amplifier

EFISH electric field induced second harmonic

ESA excited state absorption

FGR Fermi's golden rule

FOD fourth order dispersion

FROG frequency resolved optical gating

GD group delay

GDD group delay dispersion

GSB ground state bleach

HOMO highest occupied molecular orbital

LUMO lowest unoccupied molecular orbital

MIIPS multiphoton intrapulse interference phase scan

MIR mid-infrared

NIR near-infrared

OD optical density

PCBM [6,6]-Phenyl C_{61} butyric acid methyl ester

PL photo-luminescence

SE stimulated emission

SFG sum frequency generation

SHG second harmonic generation

SHG-FROG second harmonic generation frequency resolved optical gating

SPEAR spectral phase of electric field by analytic reconstruction

SPIDER spectral interferometry for direct electric field reconstruction

SubPc boron subphthalocynanine chloride

TA transient absorption

TOD third order dispersion

TRSHG time-resolved second harmonic generation

XFROG cross-correlation frequency resolved optical gating

Chapter 1

Introduction

Inter- and intramolecular charge transfer are important processes in biology, chemistry, and physics. All redox reactions require intermolecular charge transfer between molecules. Several life-sustaining biological reactions, such as photosynthesis and the Krebs cycle, depend on intermolecular charge transfer [1, 2]. Most solar-energy-harvesting systems, either natural or artificial, rely on photoinduced charge transfer and separation (except for solar thermal technologies). Improved understanding of photoinduced charge transfer processes may help guide the development of technologies such as organic photovoltaics, dye-sensitized solar cells, and photoelectrochemical cells. These technologies hold promise as part of our renewable energy future: for example, a few key advantages of organic photovoltaics over other technologies include low weight, bendability/flexibility, semitransparency, and integrability into other products [3–5]. Charge transfer and separation are some of the key processes contributing to organic photovoltaic efficiency [6]. With the goal of better understanding the device physics of organic photovoltaics, this dissertation develops a sensitive spectroscopic method for measuring charge transfer, as well as several pulse characterization techniques for enhancing the time resolution of the method. I then apply the method to two model organic photovoltaic systems to study their photoinduced charge transfer and charge separation processes.

In this introductory chapter, I begin by giving some brief background on organic photovoltaics. I then outline theories of charge transfer that are relevant for describing organic photovoltaics. To provide background for the experimental methods, I next explain how nonlinear optical spec-

troscopy may be used to study charge transfer, with a brief introduction to nonlinear optics, and with emphasis on the particular spectroscopy I developed in this thesis. Finally, I give some background in ultrafast optical pulses and pulse measurements, which are important for achieving high time resolution in nonlinear spectroscopies.

1.1 Organic photovoltaics

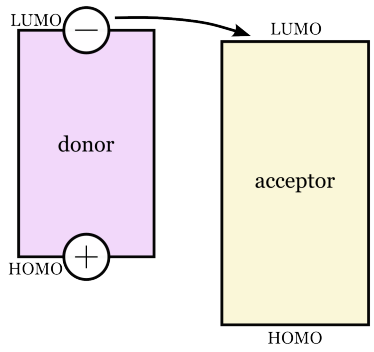

Figure 1.1: Diagram of an electron donor and an electron acceptor employed in an organic photovoltaic heterojunction. The vertical axis represents energy. The electron will tend to move to the LUMO of the electron acceptor, while the hole will tend to move to the HOMO of the electron donor. This creates a polaron pair charge transfer state, which has a lower binding energy than the initial Frenkel exciton. This picture is a simplification; Section 1.1 discusses the complexities in more detail.

In organic semiconductors, the electron-hole binding energy is typically large compared to the thermal energy $k_{\mathrm{B}}T$, where k_{B} is Boltzmann's constant and T is the temperature. When an organic photovoltaic absorbs light it usually generates a *Frenkel exciton*—where the electron and hole are localized to a single molecule—with a binding energy on the order of one electron volt ($\sim$1 eV) [3]. In a Frenkel exciton, the hole may be visualized as occupying the highest occupied molecular orbital (HOMO) of the molecule, and the electron as occupying the lowest unoccupied molecular orbital (LUMO) of the molecule, as seen in Figure 1.1. However, the energy levels and molecular orbitals associated with the HOMO and LUMO are modified by the electron-hole Coulomb attraction and by intra- and intermolecular relaxation processes. The energy of the hole is thus higher than the HOMO level and the energy of the electron is lower than the LUMO level.

A Frenkel exciton must therefore be viewed as a holistic state of an organic semiconductor.

A *heterojunction* is employed to help the electron and hole separate from each other [4]. Using two kinds of organic semiconducting molecules in the device—an electron *donor* and an electron *acceptor*—it becomes energetically favorable for a Frenkel exciton located on either kind of molecule to separate such that the donor has the hole and the acceptor has the electron. See Figure 1.1: the electron acceptor has a HOMO and LUMO that are respectively lower in energy than the HOMO and LUMO of the electron donor. Thus the electron tends to move to the LUMO of the electron acceptor, and the hole tends to move to the HOMO of the electron donor.

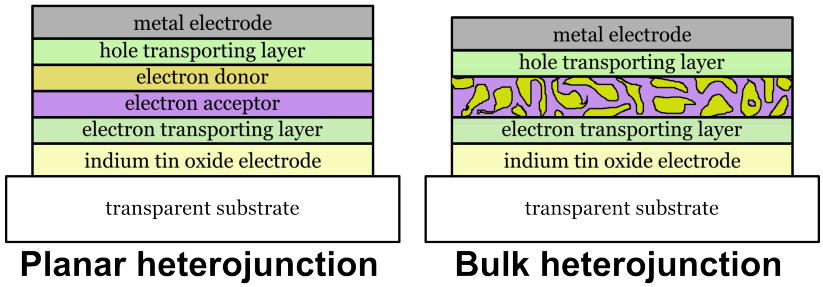

Figure 1.2: Depiction of common organic photovoltaic device geometries. Films are deposited onto a transparent substrate, through which the device is illuminated. Indium tin oxide (ITO) or another transparent conductive material forms the anode, while a metal such as aluminum forms the cathode. Transparent buffer layers—electron- and hole-transporting layers—prevent Frenkel excitons from reaching the electrodes, and prevent electrons (holes) from reaching the cathode (anode). Planar heterojunctions have separate films of electron donor and electron acceptor molecules as the active layers. Bulk heterojunctions use a mixed active layer of donor and acceptor molecules, which typically phase-separate as shown.

There are two device geometries that are particularly common for organic photovoltaics. A *planar heterojunction* uses separate layers of donor and acceptor molecules, while a *bulk heterojunction* uses a single layer of mixed donor and acceptor molecules, as depicted in Figure 1.2. Planar heterojunctions keep the electrons and the holes in separate layers, reducing *geminate* recombination between free charge carriers (meaning free electrons and holes). However, they tend to be exciton-diffusion-limited because the Frenkel excitons must diffuse a few nanometers to the interface before they can generate charges. Bulk heterojunctions do not require long diffusion lengths, thus promoting the generation of charges, at the cost of increased geminate recombination

because both types of carriers are present in the same layer. Currently, many of the best devices use the bulk heterojunction geometry, offering power conversion efficiencies in excess of 10% [5].

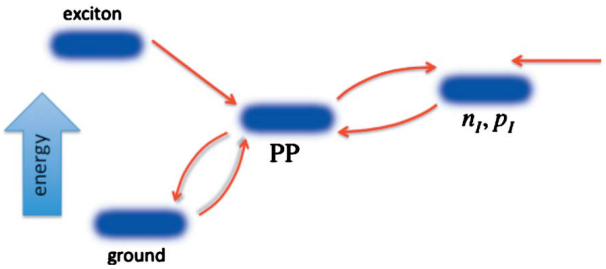

Figure 1.3: Representation of the Giebink model of an ideal-diode organic photovoltaic, adapted from [6]. The vertical axis represents energy. (Frenkel) excitons created by absorbed light diffuse to the interface to create polaron pair states (PP) with some effective current. The PP states may dissociate to create free carriers, contributing to the interfacial electron n_I and hole p_I densities, or they may recombine to the ground state. External current may also contribute to the electron and hole densities, which can recombine to create polaron pairs. Meanwhile, the ground state will spontaneously convert to a polaron pair state at some very low equilibrium rate.

The Giebink model [6] describes several important processes in organic photovoltaics, as depicted in Figure 1.3. Light absorption creates Frenkel excitons, which diffuse to an interface between electron donor and acceptor molecules. The exciton splits into a *polaron pair* where the hole is on the donor and the electron is on the acceptor, but the charges are still Coulombically bound. The binding energy is much reduced compared to the Frenkel exciton. At that point, the polaron pair can recombine (contributing to loss) or it can separate into free charges. Devices have a built-in electric field coming from the work functions of the electrodes [4], which together with thermal fluctuations helps separate the polaron pair into free charges. Once the charges are free, they may contribute to external device current.

1.2 Theories of charge transfer

In the Giebink model, the conversion step between Frenkel excitons and polaron pair states is a charge transfer process. There are many theories of charge transfer, but a qualitative picture is often shared, as depicted in Figure 1.4. The Hamiltonian for this system, involving two electronic

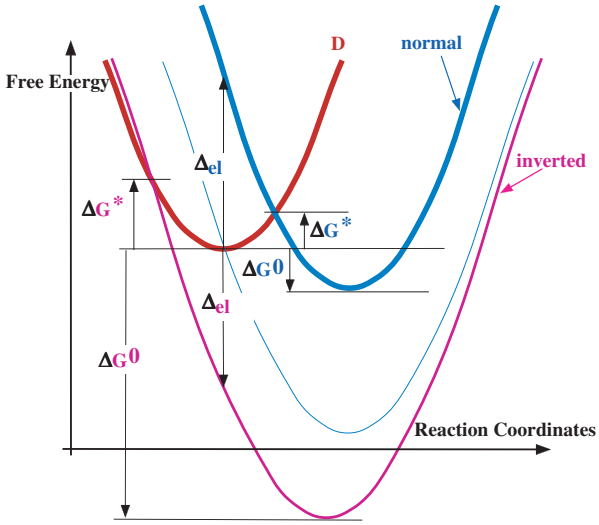

Figure 1.4: Diagram of charge transfer reactions, reproduced from [7]. The red curve labeled 'D' represents the energy of the system when the electron is still on the electron donor, as a function of the nuclear coordinates. The heavy blue curve labeled 'normal' represents the energy of the system when the electron is on the electron acceptor, for systems in the *normal* Marcus regime. The thin pink curve labeled 'inverted' represents the energy of the system when the electron is on the electron acceptor, for systems in the *inverted* Marcus regime. Then thinnest blue curve represents the boundary between the inverted and normal regimes. Δ_{el} is an indicator of the type of Marcus regime; the normal Marcus regime has $\Delta_{\text{el}} > 0$ while the inverted regime has $\Delta_{\text{el}} < 0$.

states, (adapted from [8]) is:

$$\hat{H} = |CT\rangle\hat{H}_{CT}\langle CT| + |D\rangle(\Delta G^0 + \hat{H}_D)\langle D| + |CT\rangle V_{CT-D}\langle D| + |D\rangle V_{D-CT}\langle CT|. \qquad (1.1)$$

Here, $|D\rangle$ is the donor state—the exciton state in the Giebink model—and $|CT\rangle$ is the charge transfer (or acceptor) state—the polaron pair state in the Giebink model. $\hat{H}_{CT}$ is the nuclear Hamiltonian of the CT state in the diabatic representation, and $\hat{H}_D$ is the nuclear Hamiltonian of the D state. $V_{CT-D} = V^*_{D-CT}$ is the electronic coupling coefficient, and ΔG^0 is the relative energy gap between the D state and the CT state. The nuclear Hamiltonians $\hat{H}_D$ and $\hat{H}_{CT}$ are often taken to be parabolic (i.e. normal vibrational modes), where the D curve corresponds to $\hat{H}_D$ and the 'normal' or 'inverted' curve corresponds to $\hat{H}_{CT}$. In photoinduced charge transfer reactions, the D state corresponds to an excited state created by light absorption. At nonzero temperatures, the nuclear configuration will tend to fluctuate randomly around the minimal-energy point (the equilibrium

configuration). Here $x_{\text{eq.}}^{D}$ represents the equilibrium configuration of the D state, and $x_{\text{eq.}}^{CT}$ the equilibrium of the CT state. The difference between these two values is $\Delta x_{\text{eq.}}$. The fluctuation around equilibrium enables the D state to reach an intersection with the CT state, allowing a transition to the CT state, which can then relax to its equilibrium configuration $x_{\text{eq.}}^{CT}$. The intersection is located ΔG^{*} above the D-state's minimal energy point; it is thus an energy barrier. The charge transfer state's minimal-energy point is located ΔG^{0} below the D-state's minimal energy point.

Marcus theory [7, 9] is a very widely-used theory of electron transfer, for which Marcus received the 1992 Nobel Prize in Chemistry [10]. It uses a semi-classical picture where the nuclear degrees of freedom are treated in a classical manner. The electronic degrees of freedom are treated somewhat quantum-mechanically, where the electronic energy levels vary with the nuclear degrees of freedom. The Marcus theory rate equation is

$$k_{CT\leftarrow D} = \frac{|V_{D-CT}|^2}{\hbar}\sqrt{\frac{\pi}{k_{\text{B}}TG_r}}\exp\left[-\frac{(\Delta G^0 - G_r)^2}{4k_{\text{B}}TG_r}\right]. \tag{1.2}$$

Here, k_{B} is Boltzmann's constant, T is the temperature, and G_r is a reorganization energy given by

$$G_r = \frac{1}{2}\sum_{\alpha=1}^{N}\omega_\alpha^2\Delta x_{\alpha,\,\text{eq.}}^2, \tag{1.3}$$

where ω_α is the frequency of a given vibrational mode, and $\Delta x_{\alpha,\,\text{eq.}}$ is the distance between the minimal-energy points for vibrational mode α [8, 11]. The rate equation can be simplified by observing that it is an activated process over the energy barrier ΔG^{*}, with the activation energy given by

$$\Delta G^{*} = \frac{(\Delta G^0 - G_r)^2}{4G_r}. \tag{1.4}$$

Therefore, the rate equation reduces to

$$k_{CT\leftarrow D} = \frac{|V_{D-CT}|^2}{\hbar}\sqrt{\frac{\pi}{k_{\text{B}}TG_r}}\exp\left[-\frac{\Delta G^{*}}{k_{\text{B}}T}\right]. \tag{1.5}$$

The activated-process prediction of Marcus theory implies that increasing ΔG^{*} decreases the

charge transfer rate because the thermal fluctuations will reach the intersection point less frequently.

Figure 1.4 diagrams two kinds of systems treated by Marcus theory: those in the *normal* Marcus regime, and those in the *inverted* Marcus regime. I first focus on systems in the normal regime. The charge transfer state is represented by the 'normal' curve in Figure 1.4 (heavy blue). The defining characteristic of the normal Marcus regime is that the reorganization energy G_r is greater than the transition energy ΔG^0:

$$G_r > \Delta G^0. \tag{1.6}$$

Perhaps more intuitively, in the normal regime the D–CT intersection lies between the two equilibria $x_{\text{eq.}}^{CT}$ and $x_{\text{eq.}}^{D}$, as shown in Figure 1.4. This is because $G_r > \Delta G^0$ implies that the inter-equilibrium distance $\Delta x_{\text{eq.}} > \sqrt{2\Delta G^0/\omega^2}$. In general, when $\Delta x_{\text{eq.}} = \sqrt{2\Delta G^0/\omega^2}$ then $G_r = \Delta G^0$ and so $\Delta G^* = 0$, meaning the D–CT intersection is at the D-state equilibrium $x_{\text{eq.}}^{D}$. This dividing line between the normal and inverted regime is depicted in Figure 1.4 by the thin blue curve. The transition may be visualized by an excitation energy $\Delta_{\text{el}} \equiv G_r - \Delta G^0$, which is the vertical distance from the equilibrium of the D curve to the CT curve. $\Delta_{\text{el}} > 0$ within the normal regime, and is zero for the thin blue curve.

If there are two systems in the normal Marcus regime, identical in every respect except in equilibrium separation $\Delta x_{\text{eq.}}$, then the system with reduced $\Delta x_{\text{eq.}}$ will also have reduced ΔG^* and so the reaction will be faster. Alternatively, if there are two systems in the normal Marcus regime, identical except that one has a larger transition energy ΔG^0, the one with larger ΔG^0 will have smaller ΔG^* and so the rate will be faster.

Charge transfer systems in the inverted Marcus regime are represented by the 'inverted' curve in Figure 1.4 (pink). The defining characteristic of the inverted Marcus regime is that the reorganization energy G_r is less than the transition energy ΔG^0:

$$G_r < \Delta G^0, \tag{1.7}$$

or equivalently the excitation energy $\Delta_{\text{el}} < 0$. Alternatively, in the inverted regime the D–CT intersection lies to one side of the two equilibria $x_{\text{eq.}}^{CT}$ and $x_{\text{eq.}}^{D}$, as shown in Figure 1.4. The inverted regime thus exhibits $\Delta x_{\text{eq.}} < \sqrt{2\Delta G^0/\omega^2}$. If there are two systems in the inverted Marcus regime, identical in every respect except in $\Delta x_{\text{eq.}}$, then the system with reduced $\Delta x_{\text{eq.}}$ will have increased ΔG^* and so the reaction will be slower. Meanwhile, if there are two systems in the inverted Marcus regime, identical except for their ΔG^0, the one with larger ΔG^0 will have larger ΔG^* and so the rate will be slower. Thus systems in the inverted Marcus regime have very different qualitative behavior compared to systems in the normal Marcus regime.

Moving on to a more advanced theory of charge transfer, our collaborators Lee et al. introduced us to a theory based on Fermi's golden rule (FGR) [8, 12, 13] because they were concerned that the approximations made in Marcus theory may be violated in the case of organic photovoltaics, or more generally in the case of intermolecular charge transfer [8, 11]. The theory treats all degrees of freedom fully quantum-mechanically; this includes the possibility of nuclear tunneling, for example. Systems in the inverted Marcus regime are especially likely to have contributions to the charge transfer rate originating from such tunneling, since the nuclear degrees of freedom are very similar between the D state and the charge transfer state. The FGR theory predicts a rate constant of

$$k_{CT\leftarrow D} = \frac{|V_{D-CT}|^2}{\hbar}\int_{-\infty}^{\infty} \mathrm{d}t\, e^{i\Delta G^0 t} \exp\left\{\sum_{\alpha=1}^{N} S_\alpha\left[-(2n_\alpha+1) + (n_\alpha+1)e^{-i\omega_\alpha t} + n_\alpha e^{i\omega_\alpha t}\right]\right\}, \tag{1.8}$$

where $n_\alpha = 1/(e^{\hbar\omega_\alpha/k_{\text{B}}T}-1)$ is the expected vibrational-mode occupancy and where

$$S_\alpha = \frac{\omega_\alpha}{\hbar}\Delta x_{\alpha,\,\text{eq.}}^2 \tag{1.9}$$

is the Huang-Rhys factor [8].

Marcus theory can be derived from the FGR theory, using a combination of high-temperature and short-time limits. If either limit becomes suspect for a given system, then Marcus theory as a whole is suspect. The high-temperature limit is $k_{\text{B}}T \gg \hbar\omega_\alpha$, where ω_α is the relevant normal-mode

frequency or frequencies. At room temperature, this limit is suspect if there are any vibrational modes over ∼200 wavenumbers that are important to the reaction process. However, Lee et al. [8] report that in most cases the high-temperature limit of their FGR theory gives very similar results to their full theory. The short-time limit approximates the summand elements with a second-order Taylor expansion about $t = 0$:

$$-(2n_\alpha + 1) + (n_\alpha + 1)e^{-i\omega_\alpha t} + n_\alpha e^{i\omega_\alpha t} \approx -i\omega_\alpha t - \frac{1}{2}(2n_\alpha + 1)\omega_\alpha^2 t^2. \tag{1.10}$$

This short-time limit is valid when the integral is dominated by contributions near $t = 0$. Lee et al. report that this limit is not applicable in many systems in the inverted regime [8]. They attributed this to the possibility of nuclear tunneling in the inverted regime. In general, charge transfer recombination, or back electron transfer, is commonly in the inverted Marcus regime [11, 12] because ΔG^0 is large but G_r is relatively small. In these cases Marcus theory can give wildly incorrect rates due to nuclear tunneling [12]. Since charge recombination is a major loss mechanism in the Giebink model [6] for organic solar cells, the more general FGR rates are desirable.

1.3 Nonlinear optics

Since charge transfer processes typically take place on the femtosecond to nanosecond timescales, it is difficult to study them using electrical methods. However, a wide variety of ultrafast nonlinear optical spectroscopic methods have adequate time resolution to study these processes. Nonlinear optics focuses on phenomena that only arise when very intense light interacts with matter: the light is so intense that new phenomena occur. No nonlinear optical phenomena were ever observed before the invention of the laser [14, 15] which enabled unprecedentedly high optical intensities. The field of nonlinear optics was born over 50 years ago: Peter Franken's lab here at the University of Michigan first demonstrated second harmonic generation, and many other nonlinear phenomena were observed shortly thereafter [14, 15].

Light is an oscillating electric field; as it passes through materials—glass, water, air, organic

photovoltaics—it causes an oscillating electric dipole moment in the material. This response, known as polarization density, or simply polarization P, is usually measured in units of electric dipole per unit volume. The polarization P has a back-action on the electric field E:

$$\nabla^2 E - \frac{1}{c^2}\frac{\partial^2 E}{\partial t^2} = \frac{1}{\epsilon_0 c^2}\frac{\partial^2 P}{\partial t^2}. \tag{1.11}$$

For almost all everyday-life situations, it is sufficient to represent P as a linear function of the electric field E:

$$P = \epsilon_0 \chi E. \tag{1.12}$$

where ϵ_0 is the permittivity of free space, and χ is known as the susceptibility; it is both a tensor and frequency-dependent in general. For simplicity, I will ignore its tensorial nature and frequency dependence. Once the laser was invented, it became possible to generate sufficiently intense electric fields E to observe higher-order, nonlinear corrections to the above expression for the polarization P. Within the perturbative regime, we may Taylor-expand P in powers of E:

$$P = \epsilon_0 \left[\chi^{(1)} E + \chi^{(2)} E^2 + \chi^{(3)} E^3 + \ldots\right], \tag{1.13}$$

where $\chi^{(1)}$ is the first-order susceptibility, $\chi^{(2)}$ is the second-order susceptibility, and so on. In general, each successively higher-order susceptibility is a higher-order tensor. This Taylor expansion describes coupling between different frequencies, or *frequency mixing*. For example, second harmonic generation (SHG) comes from the second-order susceptibility $\chi^{(2)}$. An optical field $E = A\sin(\omega t)$ will have a second-order polarization term proportional to $P \propto E^2 = A^2 \sin^2(\omega t) = A^2 \left[1 - \cos(2 * \omega t)\right]/2$, which has a frequency component 2ω at twice the fundamental frequency ω. Once the polarization P oscillates at 2ω, it acts as a source in the nonlinear

wave equation:

$$\begin{aligned}\nabla^2 E - \frac{1}{c^2}\frac{\partial^2 E}{\partial t^2} &= \frac{1}{\epsilon_0 c^2}\frac{\partial^2 P}{\partial t^2} \\ &= \frac{1}{c^2}\frac{\partial^2}{\partial t^2}\left(\chi^{(1)}E + \chi^{(2)}E^2 + \chi^{(3)}E^3 + \ldots\right).\end{aligned} \tag{1.14}$$

Thus once the polarization P oscillates at 2ω, it acts as a source for new light at 2ω. The material itself therefore radiates light at 2ω, yielding SHG.

Quite a few kinds of frequency mixing are possible, meaning input light may drive output light at a wide variety of frequencies. Here I write the material response P in the time domain, including frequency dependence, but still ignoring the tensor nature of χ:

$$\begin{aligned}P(t) = \quad & \epsilon_0 \int_0^\infty \chi^{(1)}(\tau)E(t-\tau)d\tau \\ & + \epsilon_0 \int_0^\infty \int_0^\infty \chi^{(2)}(\tau_1,\tau_2)E(t-\tau_1)E(t-\tau_2)d\tau_1 d\tau_2 \\ & + \epsilon_0 \int_0^\infty \int_0^\infty \int_0^\infty \chi^{(3)}(\tau_1,\tau_2,\tau_3)E(t-\tau_1)E(t-\tau_2)E(t-\tau_3)d\tau_1 d\tau_2 d\tau_3 \\ & + \ldots\end{aligned} \tag{1.15}$$

Fourier-transforming this equation reveals the many kinds of frequency mixing processes that are possible:

$$\begin{aligned}P(\omega) = \epsilon_0 & \hat{\chi}^{(1)}(\omega)\hat{E}(\omega) \\ & + \epsilon_0 \int_{-\infty}^\infty \int_{-\infty}^\infty \hat{\chi}^{(2)}(\omega_1,\omega_2)\hat{E}(\omega_1)\hat{E}(\omega_2)\delta(\omega-(\omega_1+\omega_2))d\omega_1 d\omega_2 \\ & + \epsilon_0 \int_{-\infty}^\infty \int_{-\infty}^\infty \int_{-\infty}^\infty \hat{\chi}^{(3)}(\omega_1,\omega_2,\omega_3)\hat{E}(\omega_1)\hat{E}(\omega_2)\hat{E}(\omega_3)\delta(\omega-(\omega_1+\omega_2+\omega_3))d\omega_1 d\omega_2 d\omega_3 \\ & + \ldots\end{aligned} \tag{1.16}$$

Here, $\hat{\chi}$ refers to the (non)linear susceptibility in the frequency domain, and $\hat{E}$ refers to the electric field in the frequency domain. In the linear regime, it is clear that polarization components at

ω can only come from electric field components at that same ω. However, the second-order term includes an infinite number of contributions from electric field frequencies ω_1 and ω_2, with the only requirement that the two source frequencies must sum to the resulting frequency: $\omega = \omega_1 + \omega_2$. This leads to the phenomena of sum frequency generation (SFG) and difference frequency generation (DFG) [16]. The third-order term includes even more possibilities for frequency mixing. Thus nonlinear optical phenomena are intimately connected with various kinds of frequency mixing.

The concept of *wave mixing* derives from these optical nonlinearities. The term *three wave mixing* refers to second-order processes (those depending on $\chi^{(2)}$) when ω, ω_1, and ω_2 are three different frequencies, or waves. The interaction between E and P means that all three of those waves are coupled (they mix). Occasionally the term is used referring to the spatial generalization of the above expression for P, where three different spatial frequencies (waves) mix together. Likewise, *four wave mixing* refers to third-order nonlinear processes depending on $\chi^{(3)}$, especially when there are four different spatial or temporal frequencies involved.

1.4 Nonlinear optical methods for studying charge transfer

Nonlinear optical spectroscopies are very general tools for understanding how a material or system behaves [17, 18]. For example, several decades ago Kok et al. used successive short light pulses from a flash-lamp on chloroplasts from plants, correctly predicting the four oxidative states of the oxygen-evolving complex in Photosystem II [19]. In this section, I discuss a few nonlinear spectroscopies, with emphasis on those that can measure photoinduced charge transfer.

1.4.1 Pump probe spectroscopies

In general, nonlinear spectroscopies measure a material's nonlinear susceptibility $\chi^{(n)}$. A very wide class of such spectroscopies may be termed *pump probe*, where an optical pump induces some change in a material, and some kind of probe (optical or otherwise) measures that change. The term pump probe usually refers to time-domain methods with *absorptive* probes. These methods employ

two short pulses of light termed pump and probe, with a controllable time delay t between them as depicted in Figure 1.5. The researcher measures how the pump pulse changes the transmission or reflection of the probe pulse, as a function of t. Pump probe spectroscopy is a third-order nonlinear phenomenon; the material polarization in response to the probe pulse may be written $P = \epsilon_0 \left[\chi^{(1)} + \chi^{(3)}|E_{\text{pump}}|^2\right] E_{\text{probe}}$. Conceptually, this may be thought of as an altered linear susceptibility $\chi^{(1)}_{\text{altered}} = \chi^{(1)} + \chi^{(3)}|E_{\text{pump}}|^2$ and the change in the transmission or reflection of the probe provides a measure of the altered susceptibility. This is often measured as a change ΔOD in the optical density (OD).

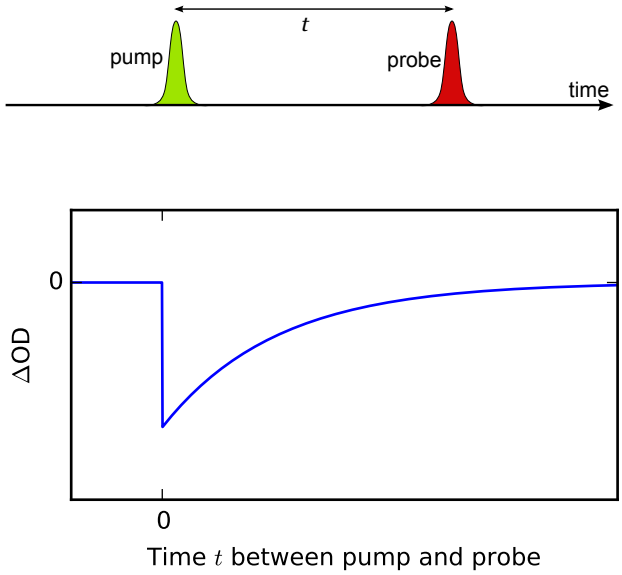

Figure 1.5: Illustration of absorptive pump probe spectroscopy. **Top:** illustration of the pulse ordering in pump probe spectroscopy. Horizontal axis, real time. The pump pulse (yellow) interacts first, followed after some time t by the probe pulse (red) which interrogates the optical density (OD). The pump and probe pulses may be the same optical frequency (degenerate pump probe) or they may be different frequencies (two-color pump probe). **Bottom:** illustration of absorptive pump probe spectroscopy in a dye, showing ΔOD=0 before t=0, showing a sharp decrease at t=0 due to ground state bleach, and a decay back to zero as the molecules relax back down to the ground state.

Consider absorptive pump probe spectroscopy of a solution of dye molecules. Before the pump hits the sample, all of the dye molecules are in the ground state and so they all absorb. After the pump excites some of the molecules, those molecules no longer absorb, and so the OD decreases.

As the molecules gradually return to the ground state, the optical density returns to its original value. This change ΔOD in the optical density is plotted in Figure 1.5. The horizontal axis is the time-delay t between the pump and the probe pulse. The probe pulse interrogates the OD; when the probe pulse precedes the pump ($t < 0$) there is no change, however, change is observed when the probe pulses follows the pump ($t > 0$). The time resolution of this experiment is governed by the time duration of the optical pulses.

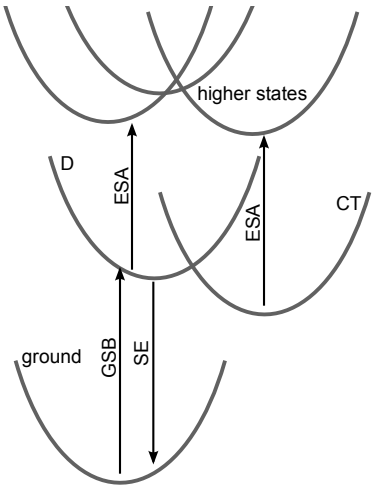

Figure 1.6: Illustration of absorptive signals that may be seen in pump probe in a typical molecular system. Horizontal axis, nuclear coordinate. Thick gray lines, electronic energy levels. Thin black arrows, optical transitions. Several types of signals are visible: ground state bleach (GSB), stimulated emission (SE) with a Stokes shift, and multiple excited state absorptions (ESA).

There are several kinds of signals that may be seen with absorptive pump probe spectroscopy, as seen in Figure 1.6. This shows an energy diagram for a hypothetical molecular system, with several energy levels. The molecules start out in the ground state, and the pump pulse puts some of them in the excited state labeled 'D.' The D-state molecules can transition to the CT state or remain in the D state; in both cases there will be an eventual decay back to ground. Since the pump decreases the number of ground-state molecules, when the probe arrives there are fewer ground-state molecules absorbing light, and so the optical density at the main transition frequency decreases. This negative feature is termed ground state bleach (GSB). Meanwhile, any D-state molecules may undergo stimulated emission (SE) back to the ground state when the probe arrives, also decreasing the optical density. The SE negative feature is typically red-shifted (has lower

energy) compared to the GSB feature due to nuclear relaxation; the shift is called the *Stokes shift*. Molecules in either of the accessible excited states (the D or CT states) can undergo excited state absorption (ESA) to higher-energy states; different ESA transitions can be different frequencies which can be a signature for population in the D versus CT states.

It is often desirable to use many different probe wavelengths to capture as many different types of absorptive signals as possible (there are many possible SE and ESA transitions, for example). Many probe wavelengths may be *multiplexed* at once by using a broadband probe pulse, and spectrally dispersing the probe frequencies onto an array detector. This multiplexed method is often called transient absorption (TA), because the change in the absorption spectrum, induced by the pump pulse, is measured.

Many kinds of non-absorptive probes may be used within the conceptual pump probe umbrella. These non-absorptive pump probe spectroscopies are no longer third-order spectroscopies, but are generally higher order. In all of them, an optical pump pulse excites some of the molecules. Instead of being absorptive (optically linear), the probe might use some optical nonlinearity itself, or use some other mode of detection. For example, much of this dissertation uses a SHG probe, where the probe pulse produces SHG, and changes in the SHG are measured as function of the time-delay between pump and probe pulses. Other types of probes include structural ones, such as X-ray or electron diffraction [20, 21]. As another example, Kok et al. [19] detected molecular oxygen evolution in the gas phase after illuminating with a probe pulse to study the oxygen-evolving complex in chloroplasts.

1.4.2 Using pump probe spectroscopies to measure charge transfer

There are several different ways to investigate charge transfer using spectroscopies within the pump probe umbrella. Several of the most popular methods use absorptive probes, chosen to be resonant with some spectral signature associated with the charge transfer state. The pump pulse excites some of the molecules—creating D states in the language of Figures 1.4 and 1.6. These gradually transition to the charge transfer state CT, and the probe detects this based on the chosen spectral

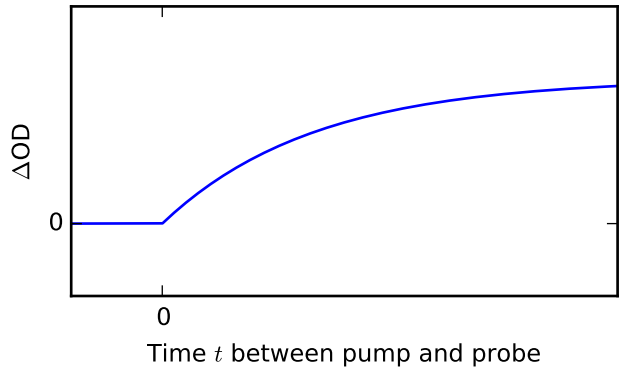

Figure 1.7: Illustration of absorptive pump probe spectroscopy on a charge transfer system, using a probe resonant a spectral signature associated with the charge transfer. Observe ΔOD=0 before t=0, followed by an increase in the charge transfer spectral signature as the excited state relaxes to the charge transfer state. There will be a slow decay back to the ground state (and ΔOD=0) but this is not shown.

signature. In this case the pump probe trace would look something like that in Figure 1.7: after photoexcitation, a slow increase in ΔOD at the probe wavelength occurs as the excited states transition to the charge transfer states. At very long times, ΔOD would return to zero as the charge transfer states decay back to the ground state. This experiment does not actually establish the presence of charge transfer; the charge transfer is inferred by proxy from the spectral signature.

Many researchers use TA spectroscopy to study organic photovoltaics, with a visible pump and a probe bandwidth spanning much of the visible and near-infrared (NIR) [22–26]. The visible pump creates the population of D states. Some time t later, the visible-NIR probe interrogates the SE and ESA in the sample. ESA in the NIR is commonly attributed to charge transfer states [22–25]. For example, C_{60} fullerene derivative anions in solution have absorptions in the NIR [27] and so organic photovoltaic materials using fullerenes as electron acceptors probably have similar absorptions in the charge transfer states. Unfortunately, in real devices the signals aren't nearly as simple as those in Figure 1.7, as seen in [22–26]. There are many spectral signatures of many different phenomena that overlap, all across the visible and NIR; sophisticated analysis and modeling are required to tease apart the phenomena.

Time-resolved microwave and terahertz methods use a visible pump and a GHz- or THz-frequency probe; a nice review of these methods is given in [28]. Most materials are fairly trans-

parent in the GHz and THz, but free carriers usually absorb. Therefore as semiconductors become optically excited by the visible pump, the photogenerated free carriers give a response measured by the probe. The data can be transformed to give the real and imaginary parts of the electrical conductivity, which can be measured as a function of time after photoexcitation. Sophisticated models of carrier scattering are employed, and in organic photovoltaics the morphology plays a critical role as well [28].

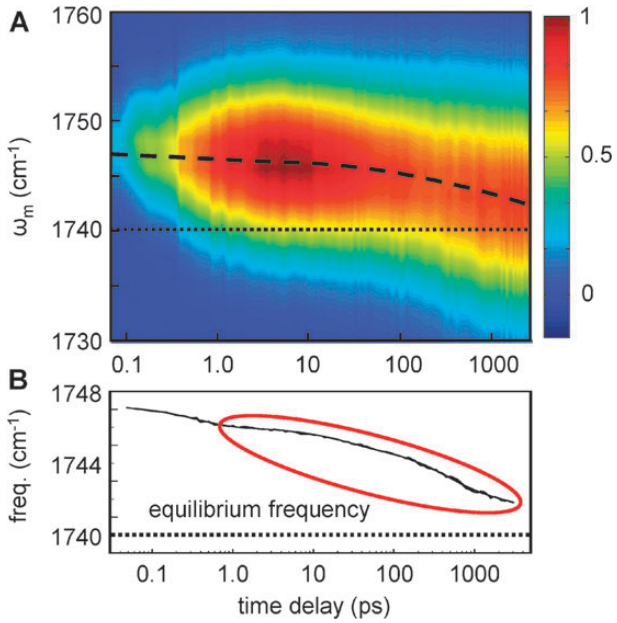

Figure 1.8: Illustration of MIR probing of a charge transfer system, reproduced from [29]. The top subfigure A shows ΔOD as a function of detection frequency and pump probe time delay t. The dashed line guides the eye as to the central frequency changing over time. The bottom subfigure B shows the central frequency as a function of time.

In visible pump, mid-infrared (MIR) probe spectroscopy, an ultrafast visible-light pump pulse creates a population of D states. Some time t later, an ultrafast MIR probe pulse interrogates the vibrational modes of the sample. In some cases, the vibrational frequencies will shift as a function of t, as seen in Figure 1.8. There are two ways that charge transfer can alter the vibrational modes: either the charge transfer state itself can have altered vibrational modes, or an unrelated spectator vibration can be shifted due to the vibrational Stark effect. Pensack et al. [29, 30] reported that the electron acceptor [6,6]-Phenyl C_{61} butyric acid methyl ester (PCBM)—a functionalized

fullerene—has a carbonyl stretch vibrational mode that shifts by several wavenumbers once PCBM accepts the electron from an electron donor. Baiz et al. [31] reported a vibrational-mode shift of almost 20 wavenumbers in a probe molecule, due to charge transfer in a neighboring molecule. The neighboring molecule's charge transfer created an electric field, which Stark-shifted the probe molecule's vibrations.

Moving to non-absorptive probes, time-resolved photo-luminescence (PL) can also be used to observe charge transfer [30, 32, 33]. In this approach a visible pump pulse creates the population of excited states, as before. In the common case where the charge transfer state is long-lived, much of the PL comes from the charge transfer state, especially in the NIR. Bernardo et al. [32] used a streak camera to time-resolve the NIR PL from a small-molecule organic photovoltaic, achieving time resolution on the order of 100 ps. Chen et al. [33] used a Kerr gate to achieve $\sim$200 fs time resolution on the PL from a polymer-based organic photovoltaic film. It is unfortunate that many systems have charge transfer states that do not have an appreciable dipole-allowed transition to the ground state, so PL does not work for those systems.

All nonlinear spectroscopies use proxies to observe the charge transfer: they look at the SE and ESA, the time-resolved conductivity, vibrational modes, or the PL. In many cases, these are good proxies, where most or all of the observed signal comes from the charge transfer state. The time-resolved conductivity is likely an especially good proxy, because free carriers represent what's being observed. Quite recently, a few groups have started to use an ultrafast measurement of electric field in the sample as a proxy [34–36]. This is a visible pump, second harmonic probe spectroscopy, where a visible pump pulse creates the population of excited states, as before. Some time t later, a non-resonant or quasi-resonant probe pulse, often in the NIR, interrogates the electric field in the sample. The signal is actually the second harmonic of the probe pulse. This works by the phenomenon of electric field induced second harmonic (EFISH): a third order nonlinear optical phenomenon, where a quasi-static (non-oscillating) electric field E_{DC} enables the material polarization to oscillate at the second harmonic of a probe pulse: $P = \epsilon_0 \chi^{(3)} E_{\text{DC}} E_{\text{probe}}^2$, where E_{probe} is the probe pulse and $\chi^{(3)}$ is the third-order nonlinear susceptibility. Charge transfer creates the

quasi-static field E_{DC}, leading to the observed EFISH. Since this field E_{DC} is likely a particularly good proxy for charge transfer, time-resolved second harmonic generation (TRSHG) can unambiguously resolve the charge transfer as a function of time. This is a *cascaded* nonlinear optical signal; the pump pulse creates the E_{DC} through a second order nonlinearity ($P_{\text{DC}} \propto \chi^{(2)}|E_{\text{pump}}|^2$) which then interacts with the probe pulse and the third order nonlinearity to produce the EFISH signal. The cascading makes this spectroscopy effectively fourth order in the input fields: second order in E_{pump} and second order in E_{probe}.

1.4.3 Using pump probe TRSHG to measure charge transfer

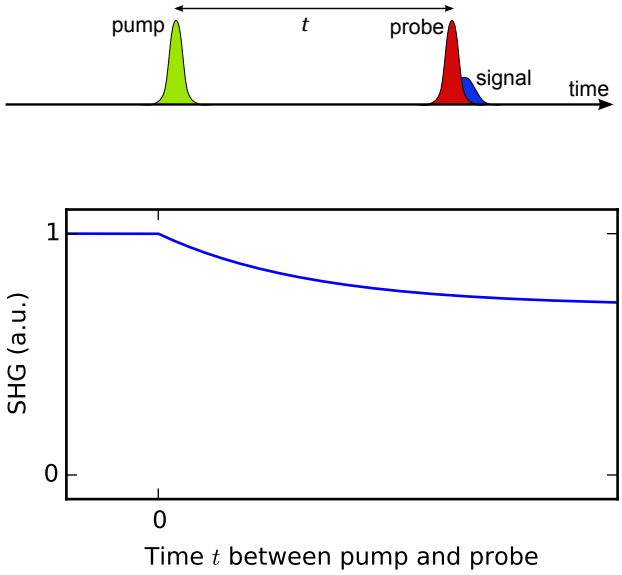

Figure 1.9: Illustration of TRSHG pump probe spectroscopy on a charge transfer system. **Top:** illustration of TRSHG spectroscopy pulse ordering. Horizontal axis, real time. The pump pulse (yellow) interacts first, followed by a probe pulse (red) after some time t. The probe pulse creates a SHG signal (blue). The pump, probe, and signal frequencies are typically all different. **Bottom:** illustration of TRSHG signals on a charge transfer system. The SHG is constant (normalized to unity) when the probe precedes the pump ($t < 0$), but falls—or rises (not shown)—for $t > 0$ as the charges separate. There will be a slow decay back to the ground state (and a corresponding return to unity SHG) but this is not shown.

There are two main sample geometries that exploit EFISH to measure charge transfer and charge separation in organic photovoltaics. One possibility employs a planar heterojunction as

depicted in Figure 1.2, without the electrodes and buffer layers [34, 35]. In this case, there is a small intrinsic second-order susceptibility $\chi^{(2)}$ leading to SHG even when the probe precedes the pump ($t < 0$). After photoexcitation ($t > 0$), the charge transfer states across the bilayer interface create an electric field which gives SHG signal through EFISH. Depending on the relative phases of $\chi^{(2)}$ and $\chi^{(3)}$ the SHG may either increase or decrease after photoexcitation. Figure 1.9 depicts this process, where the observed rate corresponds to the charge transfer.

The other sample geometry uses a bulk heterojunction with buffer layers and external electrodes [36]. There is a strong built-in electric field throughout the sample, which is directly detected by the SHG probe. After photoexcitation, free carriers are formed, which tend to migrate to oppose the built-in field. Figure 1.9 depicts this process; in the bulk heterojunction case the SHG tends to fall after photoexcitation since the carrier movement decreases the electric field. Since charges may continue to move as free carriers to oppose the built-in field, this experiment actually measures a time-dependent mobility after photoexcitation [36].

1.5 Theory of ultrafast pulses, dispersion, and ultrafast measurements

All of the above spectroscopic methods rely on short pulses of light for their time resolution. The shorter the pulses, the better the time resolution. Most of the methods described above may be termed *ultrafast*, meaning the pulses of light are shorter than $\sim$1 ps in duration. Since there are many claims of charge transfer happening in $<$100 fs [26, 34, 35, 37] it is desirable that the time resolution of the experiment (the time duration of the pulses) be much better than that, around 10–30 fs. Investigating claims of vibronic enhancement of charge transfer needs especially short pulses, around 10 fs [26, 37].

There are two key ideas to ultrafast pulses. First, the Fourier time-frequency relationships prove that if you want a pulse that is short in time, then it needs to be broad in frequency. A monochromatic light beam is infinitely long in time, and an infinitely short pulse in time requires

equal contributions from all frequencies. Second, just having a broadband pulse does not make it short: the phases of the different frequencies must be synchronized, or mode-locked. When all the phases interfere constructively, the pulse will be short. In the case of sunlight, the light is very broadband but the phases are totally random—sunlight is not pulsed at all. In general, we may represent an electromagnetic pulse $\hat{E}(\omega)$ using a combination of its spectral amplitude $|\hat{E}(\omega)|$ and its spectral phase $\phi(\omega)$:

$$\hat{E}(\omega) = |\hat{E}(\omega)| \exp(-i\phi(\omega)). \tag{1.17}$$

We use the term *transform limited* or *compressed* to refer to pulses that are as short as their spectra allow; when the spectral phase $\phi(\omega)$ is zero, $\hat{E}(\omega)$ corresponds to a transform limited pulse. Some trivial nonzero adjustments in ϕ are also OK: a phase $\phi(\omega) + \phi_0 + \phi_1\omega$ will yield the same pulse duration as $\phi(\omega)$, for arbitrary ϕ_0 and ϕ_1. The constant term ϕ_0 will alter the carrier-envelope phase (CEP), and the linear term $\phi_1\omega$ will alter the time-delay of the pulse, but the time duration will not be affected.

It is common to Taylor-expand the phase $\phi(\omega)$ of a pulse around its central frequency ω_0:

$$\phi(\omega) = \phi_0 + \phi_1(\omega - \omega_0) + \frac{1}{2}\phi_2(\omega - \omega_0)^2 + \frac{1}{6}\phi_3(\omega - \omega_0)^3 + \ldots, \tag{1.18}$$

where

$$\phi_i \equiv \left.\frac{d^i}{d\omega^i}\phi(\omega)\right|_{\omega=\omega_0}. \tag{1.19}$$

ϕ_1 is also known as the group delay (GD), since it simply adjusts the time-delay of the pulse. ϕ_2 is known as group delay dispersion (GDD), since different frequencies acquire different time-delays. This is the phenomenon of *chirp*, where the instantaneous frequency of a pulse varies over the course of time, much like an audible chirp. ϕ_3 is known as third order dispersion (TOD), ϕ_4 is known as fourth order dispersion (FOD), and so on.

If a transform limited pulse passes through material, it becomes longer, due to the dispersion it acquires as it propagates—it is no longer transform limited. All materials have a frequency-dependent index of refraction $n(\omega)$; after propagation through a length ℓ of material the pulse

will acquire a phase $\phi(\omega) = \omega \ell n(\omega)/c$ where c is the speed of light in vacuum. The frequency dependence of n ensures there are second- and higher-order derivatives of $\phi(\omega)$, leading to GDD, TOD, and so on.

A variety of methods have been devised to counteract the dispersion acquired by propagating through material. Prism compressors and grating compressors [38] exhibit a net negative GDD, compensating for the positive GDD elsewhere in the optical setup. So long as the bandwidth is not too large—so TOD doesn't matter—these work wonderfully for compressing the pulses [38]. More recently, chirped mirrors using multilayer optical interference have been created with a net negative GDD [38]. Chirped mirrors can be used with very large bandwidths, without introducing additional TOD, but their phase functions tend to be ripply. The ripples can be viewed as very high order dispersion, reducing pulse symmetry and lengthening the pulse slightly. Some researchers use a *pulse shaper* which can apply an arbitrary spectral phase (and/or amplitude) to an ultrafast pulse, and therefore can be used to compensate arbitrary dispersion to high orders. There are two dominant geometries; the 4-f geometry disperses the laser frequencies onto a spatial light modulator [39], while the acousto-optic programmable dispersive filter [40, 41] employs a fully collinear geometry where a programmable acoustic wave controls the spectral amplitude and spectral phase of a diffracted output.

No matter what method is used to counteract the dispersion, some kind of pulse measurement is necessary to characterize the time resolution of nonlinear spectroscopies. The pulse measurement quantifies the spectral phase $\phi(\omega)$, and then the pulse shaper, prism compressor, or chirped mirrors can be set to compensate that phase. All ultrafast pulse measurement methods are based on optical nonlinearities. Fundamentally, this is because all optical detectors are square-law devices: they respond to the intensity of the light but not the phase. There are no light detectors with few-femtosecond time resolution. As discussed above in the example of sunlight, knowledge of the phase is critical to knowing the time duration of the pulse. Using nonlinear optical methods, it is possible to measure the relative phases between the different frequencies in pulses, which is enough information to determine pulse duration. There are several classes of ultrafast pulse measurement

methods. A few of the most common methods are frequency resolved optical gating (FROG) [42], spectral interferometry for direct electric field reconstruction (SPIDER) [43–45], and multiphoton intrapulse interference phase scan (MIIPS) [46–49].

1.5.1 FROG

There are several variations of FROG; one example is second harmonic generation frequency resolved optical gating (SHG-FROG). In SHG-FROG an unknown test pulse is split in two, and then recombined in a material with a second-order nonlinearity. The SHG spectrum coming from the two pulses is measured in a spectrometer, as a function of the time-delay between the two pulses. If the time-delay between the two is τ, we may write an expression for the SHG-FROG signal:

$$E_{\text{SHG-FROG}}(t,\tau) \propto E(t)E(t-\tau). \tag{1.20}$$

This comes from the above definition of nonlinear polarization in Equation 1.15, assuming χ is essentially impulsive and frequency-independent [42]. What is measured in the spectrometer comes from the Fourier transform,

$$I_{\text{SHG-FROG}}(\omega,\tau) \propto \left| \int_{-\infty}^{\infty} \propto E(t)E(t-\tau)\exp(-i\omega t)dt \right|^2 \tag{1.21}$$

Measuring this as a function of the detection frequency ω and the time-delay τ between pulse replicas gives a spectrogram $I_{\text{SHG-FROG}}(\omega,\tau)$; numerical algorithms have been developed to invert the spectrogram to yield the spectral amplitude and phase of the pulse [42]. For FROG to be accurate, the spectrometer needs to be well-calibrated and the delay-stage producing τ needs to be calibrated in relative terms, but these requirements are easy to meet. The biggest advantage of FROG methods is that they provide very direct measures of pulse duration. Effects like spatial chirp [50] or phase noise [51] can cause other methods to falsely report a very short pulse, when FROG would reveal the true longer pulse duration.

1.5.2 SPIDER

There are many versions of SPIDER [43–45], but they all work by making two nonlinear replicas of the test pulse, with slightly different frequencies and time-delays. For example, sum frequency generation between a very narrowband pulse with central frequency Ω and the test pulse with central frequency ω_0 will produce a (weak) replica of the test pulse, with central frequency $\Omega + \omega_0$. Using two different narrowband pulses, with frequencies $\Omega + \Delta/2$ and $\Omega - \Delta/2$, will yield two replicas of the test pulse, with central frequencies $\Omega + \Delta/2 + \omega_0$ and $\Omega - \Delta/2 + \omega_0$. If the two narrowband pulses are almost the same frequency ($|\Delta|$ is small), then the replicas will interfere, with spectral shear. A time delay τ is added to one of the replicas. Therefore the signal field may be represented as

$$\hat{E}_{\text{SPIDER}}(\omega) = \hat{E}(\omega - \Omega - \Delta/2) + \hat{E}(\omega - \Omega + \Delta/2)\exp(-i\omega\tau), \tag{1.22}$$

where in this expression ω takes on values near $\Omega + \omega_0$. With a change of variable $\nu = \omega - \Omega$, the detected spectral intensity becomes

$$\begin{aligned} I_{\text{SPIDER}}(\nu + \Omega) &\propto \left|\hat{E}_{\text{SPIDER}}(\nu + \Omega)\right|^2 \\ &\propto \left|\hat{E}(\nu - \Delta/2)\right|^2 + \left|\hat{E}(\nu + \Delta/2)\right|^2 + \hat{E}(\nu - \Delta/2)\hat{E}^*(\nu + \Delta/2)\exp(i(\nu + \Omega)\tau) \\ &\quad + \hat{E}^*(\nu - \Delta/2)\hat{E}(\nu + \Delta/2)\exp(-i(\nu + \Omega)\tau). \end{aligned} \tag{1.23}$$

Using the techniques of spectral interferometry [52–54] a quickly-oscillating interference term can be separated from the others:

$$I_{\text{SI}}(\nu + \Omega) = \hat{E}^*(\nu - \Delta/2)\hat{E}(\nu + \Delta/2)\exp(-i(\nu + \Omega)\tau). \tag{1.24}$$

I now explicitly rewrite the unknown pulse $\hat{E}(\nu)$ in terms of its amplitude $|\hat{E}(\nu)|$ and phase $\phi(\nu)$:

$$I_{\text{SI}}(\nu+\Omega) = \left|\hat{E}^*(\nu-\Delta/2)\hat{E}(\nu+\Delta/2)\right| \exp\left[-i(\nu+\Omega)\tau - i\phi(\nu-\Delta/2) + i\phi(\nu+\Delta/2)\right]. \tag{1.25}$$

Computing the complex argument (the phase) and dividing by Δ starts to look like the first derivative of the phase $\phi'(\nu)$—the spectral GD, meaning the group delay as a function of frequency—plus a linear term:

$$\frac{\arg\{I_{\text{SI}}(\nu+\Omega)\}}{\Delta} = -\frac{(\nu+\Omega)\tau}{\Delta} + \frac{\phi(\nu+\Delta/2) - \phi(\nu-\Delta/2)}{\Delta}. \tag{1.26}$$

In particular, taking the limit of small Δ yields that spectral GD plus a linear term:

$$\lim_{\Delta\to 0} \frac{\arg\{I_{\text{SI}}(\nu+\Omega)\}}{\Delta} = -\frac{(\nu+\Omega)\tau}{\Delta} + \phi'(\nu). \tag{1.27}$$

Assuming τ/Δ is well-calibrated, the linear term can be easily removed. Precise knowledge of Ω is not required, since a constant term in the spectral GD $\phi'(\nu)$ does not affect the pulse duration. Speed is SPIDER's biggest advantage: in principle only one laser pulse is necessary, and the above computations are very fast. There are two main disadvantages to SPIDER: first, there are quite a few parameters that need to be carefully adjusted to make things work. τ needs to be large enough to avoid contamination between the terms in the spectral interferometry, while small enough that the spectrometer's resolution is not an issue. Δ needs to be small enough to make the limit in Equation 1.27 applicable, but large enough to get good S/N on the difference $\phi(\nu+\Delta/2) - \phi(\nu-\Delta/2)$. Making matters worse, some implementations of SPIDER couple τ and Δ, where a change in τ also changes Δ. Second, SPIDER requires precise knowledge of τ/Δ in absolute terms, which is not easy to achieve in many implementations.

1.5.3 MIIPS

MIIPS was designed from the ground up to be used with a pulse shaper. On the other hand, FROG and SPIDER were designed to be built with conventional optics; separate optics like prism/grism compressors or chirped mirrors are required to adjust the spectral phase to make it zero. However, a pulse shaper can perform both duties: it can measure the pulse and adjust its phase. Thus MIIPS was designed for simultaneous measurement and correction of the spectral phase. This saves the researcher a lot of time, by reducing optics and alignment time. The pulse shaper applies a series of sinusoidal phase functions $f_j(\omega) = \alpha \sin(\gamma\omega - \delta_j)$, yielding the following pulse shapes:

$$\hat{E}_j(\omega) = |\hat{E}(\omega)| \exp\left[-i\phi(\omega) - i\alpha \sin(\gamma\omega - \delta_j)\right], \tag{1.28}$$

which have total phase $\varphi_j(\omega) = \phi(\omega) + f_j(\omega)$. The second harmonic spectrum of each resulting pulse is recorded with a spectrometer:

$$I_j(\omega) \propto \left| \int_{-\infty}^{\infty} E_j^2(t) \exp(-i\omega t) dt \right|^2. \tag{1.29}$$

As discussed in [47], this may be rewritten as a convolution:

$$I_j(2\omega) \propto \left| \int_{-\infty}^{\infty} \left|\hat{E}(\omega+\Omega)\right| \left|\hat{E}(\omega-\Omega)\right| \exp\left[i\varphi(\omega+\Omega) + i\varphi(\omega-\Omega)\right] d\Omega \right|^2. \tag{1.30}$$

This convolution will tend to maximize when the phase term $\varphi(\omega+\Omega)+\varphi(\omega-\Omega)$ is approximately zero, corresponding to a compressed pulse or a compressed portion of a pulse. Therefore it is expected the spectrum for a given ω will be maximized when $\varphi''(\omega) = \phi''(\omega) + f''(\omega) \approx 0$. By scanning the values δ_j and choosing the $\delta_m(\omega)$ that maximizes $I_j(2\omega)$ for a particular frequency ω, we can use that as a heuristic estimate for $\phi''(\omega)$. Specifically,

$$\phi''(\omega) \approx \alpha\gamma^2 \sin(\gamma\omega - \delta_m(\omega)). \tag{1.31}$$

Now, the GDD $\phi''(\omega) + f''(\omega)$ is equal to zero for two values of δ between 0 and 2π, so there are actually two δ-values named $\delta_m^{(1)}$ and $\delta_m^{(2)}$ that maximize $I_j(2\omega)$. Averaging the two corresponding heuristic estimates gives a better heuristic, in practice:

$$\phi''(\omega) \approx \frac{1}{2}\alpha\gamma^2 \left[\sin(\gamma\omega - \delta_m^{(1)}(\omega)) + \sin(\gamma\omega - \delta_m^{(2)}(\omega))\right]. \tag{1.32}$$

The pulse shaper is then set to compensate the measured phase, and then the pulse shaper runs the MIIPS algorithm again starting from the corrected phase. After several iterations, the process converges to a fully-compensated phase, corresponding to a very short pulse. MIIPS has the advantage of being particularly accurate: it has been used for impressively precise measurements of materials' dispersion [48].

1.6 Outline of this dissertation

I now outline the remainder of this dissertation. I first develop TRSHG as a spectroscopy a bit further. In organic photovoltaics, exciton-exciton annihilation can be very strong because the distance between excitons is so small. To avoid this problem, very low pump fluences are used; this decreases signal strength. Coupled with the fact that SHG as a phenomenon is already weak, TRSHG signals from organic photovoltaics become extremely low. It is therefore desirable to add optical heterodyne detection to TRSHG, decreasing sensitivity to read noise, dark current, and stray light. Heterodyne detection also allows both the amplitude and the phase of the SHG to be directly detected, which can aid physical understanding; for example, providing information about molecular orientations or the direction of charge transfer. Chapter 2 contains "Heterodyne-detected and ultrafast time-resolved second-harmonic generation for sensitive measurements of charge transfer" (doi:10.1364/OL.39.004274) describing such a heterodyne-detected version of TRSHG spectroscopy [55].

A prototypical organic photovoltaic planar heterojunction employs boron subphthalocyanine chloride as the electron donor and C_{60} as the electron acceptor. We investigate charge transfer in

this system using a combination of TRSHG and our collaborators' theory of electron transfer based on FGR. This work is described in Chapter 3, which contains "Ultrafast charge-transfer dynamics at the boron subphthalocyanine chloride / C_{60} heterojunction: Comparison between experiment and theory" (as it was first submitted to the *Journal of Physical Chemistry Letters*).

The Forrest group recently reported a particularly efficient organic photovoltaic [56, 57] based on tetraphenyldibenzoperiflanthene as the electron donor and C_{70} as the electron acceptor. It employed the bulk heterojunction geometry. They were surprised that the maximal efficiency was reached at a donor:acceptor mixing ratio of 1:8 rather than a more even mixture. We investigated this system and its concentration dependence using a novel two-dimensional heterodyne-detected TRSHG technique, in Chapter 4: "Concentration dependence of ultrafast carrier dynamics in tetraphenyldibenzoperiflanthene / C_{70} bulk heterojunctions" (not yet submitted to any journal).

The next two chapters focus on ultrafast pulse measurements using a pulse shaper. A method to adapt FROG, using a pulse shaper as the only active element, is developed. This is helpful because no extra optics or alignment are necessary. However, some extra signals are generated, requiring separation of the FROG signals from the other signals. Chapter 5, "Fast second harmonic generation frequency resolved optical gating using only a pulse shaper" (doi:10.1364/OL.38.002980) [58], discusses a SHG-FROG implemented using only a pulse shaper, using a phase cycling method to remove unwanted signals.

It is difficult to determine which pulse compression method is the best for any particular application. Pulse energies, bandwidth, repetition rates, and many other experimental considerations factor into the decision. For the most part, if a pulse shaper is already in use, I believe using a pulse-shaper-only method makes the most sense, because a researcher's time is a precious commodity. Complicating the decision of which pulse compression method is best, very few direct comparisons between pulse measurement methods have been performed, and none at all in the pulse-shaper-only regime. To address this problem, Chapter 6 contains "Comparison of pulse compression methods using only a pulse shaper" (doi:10.1364/JOSAB.31.001544) [59]. It performs an explicit comparison between several different pulse-shaper-only methods. It also introduces a new

method named spectral phase of electric field by analytic reconstruction (SPEAR), and includes it in the comparison. It is perhaps surprising that the best methods, at least within pulse-shaper-only contexts, do not include the widely-used methods FROG, SPIDER, and MIIPS.

Finally, Chapter 7 summarizes the main scientific results in this dissertation, and discusses future directions for research.

References

[1] Robert E. Blankenship. *Molecular Mechanisms of Photosynthesis*. Wiley-Blackwell, (2002).

[2] John M. Lowenstein. *Methods in Enzymology, Volume 13: Citric Acid Cycle*. Academic Press, (1969).

[3] Stephen R. Forrest. The path to ubiquitous and low-cost organic electronic appliances on plastic. *Nature*, **428**:911–8, (2004).

[4] Harald Hoppe and Niyazi Serdar Sariciftci. Organic solar cells: An overview. *Journal of Materials Research*, **19**:1924–1945, (2004).

[5] M. C. Scharber and N. S. Sariciftci. Efficiency of bulk-heterojunction organic solar cells. *Progress in Polymer Science*, **38**:1929–1940, (2013).

[6] N. C. Giebink, G. P. Wiederrecht, M. R. Wasielewski, and S. R. Forrest. Ideal diode equation for organic heterojunctions. I. Derivation and application. *Physical Review B*, **82**:155305, (2010).

[7] S. Aubry. A nonadiabatic theory for electron transfer and application to ultrafast catalytic reactions. *Journal of Physics: Condensed Matter*, **19**:255204, (2007).

[8] Myeong H. Lee, Barry D. Dunietz, and Eitan Geva. Calculation from first principles of intramolecular golden-rule rate constants for photo-induced electron transfer in molecular donoracceptor systems. *The Journal of Physical Chemistry C*, **117**:23391–23401, (2013).

[9] R. A. Marcus. On the theory of oxidation-reduction reactions involving electron transfer. I. *The Journal of Chemical Physics*, **24**:966, (1956).

[10] Nobelprize.org. All Nobel Prizes in Chemistry. URL `http://www.nobelprize.org/nobel_prizes/chemistry/laureates/`.

[11] Paul F. Barbara, Thomas J. Meyer, and Mark A. Ratner. Contemporary issues in electron transfer research. *The Journal of Physical Chemistry*, **100**:13148–13168, (1996).

[12] Myeong H. Lee, Eitan Geva, and Barry D. Dunietz. Calculation from first-principles of golden rule rate constants for photoinduced subphthalocyanine/fullerene interfacial charge transfer and recombination in organic photovoltaic cells. *The Journal of Physical Chemistry C*, **118**:9780–9789, (2014).

[13] Myeong H. Lee, Barry D. Dunietz, and Eitan Geva. Donor-to-donor vs donor-to-acceptor

interfacial charge transfer states in the phthalocyanine–fullerene organic photovoltaic system. *The Journal of Physical Chemistry Letters*, **5**:3810–3816, (2014).

[14] P. A. Franken, A. E. Hill, C. W. Peters, and G. Weinreich. Generation of optical harmonics. *Physical Review Letters*, **7**:118–119, (1961).

[15] P. A. Franken and J. F. Ward. Optical harmonics and nonlinear phenomena. *Reviews of Modern Physics*, **35**:23–39, (1963).

[16] Robert W. Boyd. *Nonlinear Optics*. Academic Press, third edition, (2008).

[17] Shaul Mukamel. *Principles of Nonlinear Optical Spectroscopy*. Oxford University Press, (1999).

[18] Leonas Valkunas, Darius Abramavicius, and Tomás Mancal. *Molecular Excitation Dynamics and Relaxation: Quantum Theory and Spectroscopy*. Wiley-VCH, (2013).

[19] Bessel Kok, Bliss Forbush, and Marion McGloin. Cooperation of charges in photosynthetic O_2 evolution—I. A linear four step mechanism. *Photochemistry and Photobiology*, **11**:457–475, (1970).

[20] Hyotcherl Ihee, Vladimir A. Lobastov, Udo M. Gomez, Boyd M. Goodson, Ramesh Srinivasan, Chong-Yu Ruan, and Ahmed H. Zewail. Direct imaging of transient molecular structures with ultrafast diffraction. *Science*, **291**:458–62, (2001).

[21] H. Ihee, M. Lorenc, T. K. Kim, Q. Y. Kong, M. Cammarata, J. H. Lee, S. Bratos, and M. Wulff. Ultrafast x-ray diffraction of transient molecular structures in solution. *Science*, **309**:1223–7, (2005).

[22] James Kirkpatrick, Panagiotis E. Keivanidis, Annalisa Bruno, Fei Ma, Saif A. Haque, Arkady Yarstev, Villy Sundstrom, and Jenny Nelson. Ultrafast transient optical studies of charge pair generation and recombination in poly-3-hexylthiophene(P3ht):[6,6]phenyl C61 butyric methyl acid ester (PCBM) blend films. *The Journal of Physical Chemistry B*, **115**:15174–80, (2011).

[23] Fabian Etzold, Ian A. Howard, Nina Forler, Don M. Cho, Michael Meister, Hannah Mangold, Jie Shu, Michael Ryan Hansen, Klaus Müllen, and Frédéric Laquai. The effect of solvent additives on morphology and excited-state dynamics in PCPDTBT:PCBM photovoltaic blends. *Journal of the American Chemical Society*, **134**:10569–83, (2012).

[24] Sanjeev Singh and Zeev Vardeny. Ultrafast transient spectroscopy of polymer/fullerene blends for organic photovoltaic applications. *Materials*, **6**:897–910, (2013).

[25] Ajay Ram Srimath Kandada, Giulia Grancini, Annamaria Petrozza, Stefano Perissinotto, Daniele Fazzi, Sai Santosh Kumar Raavi, and Guglielmo Lanzani. Ultrafast energy transfer in ultrathin organic donor/acceptor blend. *Scientific Reports*, **3**:2073, (2013).

[26] Sarah Maria Falke, Carlo Andrea Rozzi, Daniele Brida, Margherita Maiuri, Michele Amato, Ephraim Sommer, Antonietta De Sio, Angel Rubio, Giulio Cerullo, Elisa Molinari, and Christoph Lienau. Coherent ultrafast charge transfer in an organic photovoltaic blend. *Science*, **344**:1001–5, (2014).

[27] Dirk M. Guldi and Maurizio Prato. Excited-state properties of C_{60} fullerene derivatives. *Accounts of Chemical Research*, **33**:695–703, (2000).

[28] Ronald Ulbricht, Euan Hendry, Jie Shan, Tony F. Heinz, and Mischa Bonn. Carrier dynamics in semiconductors studied with time-resolved terahertz spectroscopy. *Reviews of Modern Physics*, **83**:543–586, (2011).

[29] Ryan D. Pensack, Kyle M. Banyas, Larry W. Barbour, Maureen Hegadorn, and John B. Asbury. Ultrafast vibrational spectroscopy of charge-carrier dynamics in organic photovoltaic materials. *Physical Chemistry Chemical Physics : PCCP*, **11**:2575–91, (2009).

[30] Ryan D. Pensack and John B. Asbury. Ultrafast probes of charge transfer states in organic photovoltaic materials. *Chemical Physics Letters*, **515**:197–205, (2011).

[31] Carlos R. Baiz and Kevin J. Kubarych. Ultrafast vibrational Stark-effect spectroscopy: exploring charge-transfer reactions by directly monitoring the solvation shell response. *Journal of the American Chemical Society*, **132**:12784–5, (2010).

[32] B. Bernardo, D. Cheyns, B. Verreet, R. D. Schaller, B. P. Rand, and N. C. Giebink. Delocalization and dielectric screening of charge transfer states in organic photovoltaic cells. *Nature Communications*, **5**:3245, (2014).

[33] Kai Chen, Alex J. Barker, Matthew E. Reish, Keith C. Gordon, and Justin M. Hodgkiss. Broadband ultrafast photoluminescence spectroscopy resolves charge photogeneration via delocalized hot excitons in polymer:fullerene photovoltaic blends. *Journal of the American Chemical Society*, **135**:18502–12, (2013).

[34] L. G. Kaake, A. Jailaubekov, K. J. Williams, and X.-Y. Zhu. Probing ultrafast charge separation at organic donor/acceptor interfaces by a femtosecond electric field meter. *Applied Physics Letters*, **99**:083307, (2011).

[35] Askat E. Jailaubekov, Adam P. Willard, John R. Tritsch, Wai-Lun Chan, Na Sai, Raluca Gearba, Loren G. Kaake, Kenrick J. Williams, Kevin Leung, Peter J. Rossky, and X.-Y. Zhu. Hot charge-transfer excitons set the time limit for charge separation at donor/acceptor interfaces in organic photovoltaics. *Nature Materials*, **12**:66–73, (2013).

[36] D. Amarasinghe Vithanage, A. Devižis, V. Abramavičius, Y. Infahsaeng, D. Abramavičius, R. C. I. MacKenzie, P. E. Keivanidis, A. Yartsev, D. Hertel, J. Nelson, V. Sundström, and V. Gulbinas. Visualizing charge separation in bulk heterojunction organic solar cells. *Nature Communications*, **4**:2334, (2013).

[37] Yin Song, Scott N. Clafton, Ryan D. Pensack, Tak W. Kee, and Gregory D. Scholes. Vibrational coherence probes the mechanism of ultrafast electron transfer in polymer-fullerene blends. *Nature Communications*, **5**:4933, (2014).

[38] Andrew M. Weiner. *Ultrafast Optics*. John Wiley & Sons, Inc., Hoboken, NJ, USA, (2009).

[39] A. M. Weiner. Femtosecond pulse shaping using spatial light modulators. *Review of Scientific Instruments*, **71**:1929, (2000).

[40] Pierre Tournois. Acousto-optic programmable dispersive filter for adaptive compensation of group delay time dispersion in laser systems. *Optics Communications*, **140**:245–249, (1997).

[41] F. Verluise, V. Laude, Z. Cheng, Ch. Spielmann, and P. Tournois. Amplitude and phase control of ultrashort pulses by use of an acousto-optic programmable dispersive filter: pulse compression and shaping. *Optics Letters*, **25**:575, (2000).

[42] Rick Trebino. *Frequency-Resolved Optical Gating: The Measurement of Ultrashort Laser*

Pulses. Springer, (2002).

[43] C. Iaconis and I. A. Walmsley. Spectral phase interferometry for direct electric-field reconstruction of ultrashort optical pulses. *Optics Letters*, **23**:792, (1998).

[44] Peter Baum, Stefan Lochbrunner, and Eberhard Riedle. Zero-additional-phase SPIDER: full characterization of visible and sub-20-fs ultraviolet pulses. *Optics Letters*, **29**:210, (2004).

[45] Ian A. Walmsley and Christophe Dorrer. Characterization of ultrashort electromagnetic pulses. *Advances in Optics and Photonics*, **1**:308, (2009).

[46] Vadim V. Lozovoy, Igor Pastirk, and Marcos Dantus. Multiphoton intrapulse interference. IV. Ultrashort laser pulse spectral phase characterization and compensation. *Optics Letters*, **29**: 775, (2004).

[47] Bingwei Xu, Jess M. Gunn, Johanna M. Dela Cruz, Vadim V. Lozovoy, and Marcos Dantus. Quantitative investigation of the multiphoton intrapulse interference phase scan method for simultaneous phase measurement and compensation of femtosecond laser pulses. *Journal of the Optical Society of America B*, **23**:750, (2006).

[48] Yves Coello, Bingwei Xu, Tricia L. Miller, Vadim V. Lozovoy, and Marcos Dantus. Group-velocity dispersion measurements of water, seawater, and ocular components using multiphoton intrapulse interference phase scan. *Applied Optics*, **46**:8394, (2007).

[49] Yves Coello, Vadim V. Lozovoy, Tissa C. Gunaratne, Bingwei Xu, Ian Borukhovich, Chienhung Tseng, Thomas Weinacht, and Marcos Dantus. Interference without an interferometer: a different approach to measuring, compressing, and shaping ultrashort laser pulses. *Journal of the Optical Society of America B*, **25**:A140, (2008).

[50] Selcuk Akturk, Xun Gu, Pablo Gabolde, and Rick Trebino. The general theory of first-order spatio-temporal distortions of Gaussian pulses and beams. *Optics Express*, **13**:8642, (2005).

[51] Justin Ratner, Günter Steinmeyer, Tsz Chun Wong, Randy Bartels, and Rick Trebino. Coherent artifact in modern pulse measurements. *Optics Letters*, **37**:2874–6, (2012).

[52] L. Lepetit, G. Chériaux, and M. Joffre. Linear techniques of phase measurement by femtosecond spectral interferometry for applications in spectroscopy. *Journal of the Optical Society of America B*, **12**:2467, (1995).

[53] L. Lepetit and M. Joffre. Two-dimensional nonlinear optics using Fourier-transform spectral interferometry. *Optics Letters*, **21**:564–6, (1996).

[54] Christophe Dorrer, Nadia Belabas, Jean-Pierre Likforman, and Manuel Joffre. Spectral resolution and sampling issues in Fourier-transform spectral interferometry. *Journal of the Optical Society of America B*, **17**:1795, (2000).

[55] Daniel E. Wilcox, Matthew E. Sykes, Andrew Niedringhaus, Max Shtein, and Jennifer P. Ogilvie. Heterodyne-detected and ultrafast time-resolved second-harmonic generation for sensitive measurements of charge transfer. *Optics Letters*, **39**:4274, (2014).

[56] Xin Xiao, Jeramy D. Zimmerman, Brian E. Lassiter, Kevin J. Bergemann, and Stephen R. Forrest. A hybrid planar-mixed tetraphenyldibenzoperiflanthene/C_{70} photovoltaic cell. *Applied Physics Letters*, **102**:073302, (2013).

[57] Xin Xiao, Kevin J. Bergemann, Jeramy D. Zimmerman, Kyusang Lee, and Stephen R. For-

rest. Small-molecule planar-mixed heterojunction photovoltaic cells with fullerene-based electron filtering buffers. *Advanced Energy Materials*, **4**:1301557, (2014).

[58] Daniel E. Wilcox, Franklin D. Fuller, and Jennifer P. Ogilvie. Fast second-harmonic generation frequency-resolved optical gating using only a pulse shaper. *Optics Letters*, **38**:2980, (2013).

[59] Daniel E. Wilcox and Jennifer P. Ogilvie. Comparison of pulse compression methods using only a pulse shaper. *Journal of the Optical Society of America B*, **31**:1544, (2014).

Chapter 2

Heterodyne-detected and ultrafast time-resolved second harmonic generation for sensitive measurements of charge-transfer

Photo-induced charge transfer is a key step in light-harvesting systems. Organic photovoltaics, biological photosynthesis, many fluorescent proteins, and many photoelectrochemical systems all crucially depend on the conversion process that begins with light absorption and its generation of charge transfer states. In all of these systems, molecules absorb light, creating an exciton that moves to an interface between electron donor and acceptor molecules, driving charge transfer and eventually charge separation. The charge-transfer and separation steps are critical to system performance because the charge carriers are spatially proximate and Coulombically bound, enhancing the probability of recombination. In organic photovoltaics for example, theory predicts that the charge-transfer rate, charge separation rate, and charge recombination rate all crucially affect device performance [1]. Because these processes occur on femtosecond to nanosecond timescales, they are difficult to measure using electrical methods. However, ultrafast laser spectroscopy sensitive to charge transfer can achieve the required time resolution.

Traditional methods for studying charge transfer using ultrafast spectroscopy include pump-probe (also called transient absorption or photoinduced absorption) and time-resolved fluorescence (or photoluminescence) [2–6]. These methods use proxies for charge-transfer: they track spectral signatures believed to be due to charge-transfer or charge-separated states. For example,

near-infrared transient absorption in organic photovoltaics is commonly ascribed to charge transfer states [2–4]. These spectroscopies generate signal throughout the bulk of the device, which must be distinguished from the charge-transfer and charge-separation signals specific to the interface [7]. Due to symmetry considerations, second-harmonic-generation (SHG) when used with amorphous or centrosymmetric materials only occurs at interfaces [8]. Therefore ultrafast time-resolved second-harmonic-generation spectroscopy (TRSHG) [7, 9–12] has the advantage of being interface-specific. It is sensitive to several time-resolved surface phenomena, including charge-transfer using electric field induced second harmonic (EFISH) generation [7, 9–12].

Organic photovoltaics produce extremely small amounts of SHG; they do not withstand much laser fluence. Stray light, read noise, detector dark current, and shot noise must be addressed with care. Optical heterodyne detection helps with these issues [13] by interfering the signal field with a reference field, or local oscillator (LO). This increases signal amplitude, reducing the influence of read noise and dark current. The impact of stray light is reduced because it is not coherent with the LO. It also allows for phase-sensitive detection of the nonlinear response, which can aid physical understanding; for example, providing information about molecular orientations or the direction of charge transfer [14, 15]. Many implementations of heterodyne-detected surface SHG have been done in the time domain [16, 17], measuring the intensity of the LO interfering with the signal as a function of their relative time-delay. Other implementations have been done in the frequency domain [14, 15, 18], where a multi-channel spectrometer records the spectral intensity of the LO interfering with the signal at a fixed relative time-delay (spectral interferometry). This frequency-domain implementation has been used for TRSHG; Wilson et al. [14] tracked thermally-induced changes in the surface SHG of pure silicon with $\sim$1 s time-resolution. I present a frequency-domain heterodyne-detected TRSHG with ultrafast time resolution, using a pump-probe configuration. I briefly describe the theory of spectral interferometry in optical heterodyne contexts and how it applies to TRSHG. I then experimentally demonstrate how S/N scales with LO strength, and demonstrate a time-resolved trace using an archetypal boron subphthalocyanine chloride / fullerene heterojunction.

I perform spectral interferometry by linearly mixing the nonlinear signal field E_{SHG} with a time-delayed LO field E_{LO} that is mutually coherent with the signal, and measure the resulting spectral intensity [19]. The relative spectral phase between E_{SHG} and E_{LO} can be modeled as $\phi(\omega) = \phi_0 + \tau(\omega - \omega_0) + \phi_2(\omega - \omega_0)^2/2$ where ϕ_0 is a constant phase, ω_0 is some central frequency, τ is the time-delay between the two fields, and ϕ_2 is the group delay dispersion (causing negligible pulse-broadening). The interference is detected using a spectrometer, yielding $I(\omega) = |E_{\text{LO}}(\omega) + E_{\text{SHG}}(\omega)\exp(-i\phi(\omega))|^2$. Expanding this expression yields four terms; the one equal to $|E_{\text{SHG}}(\omega)|^2$ is negligible because it is much weaker than the other terms. The remaining three terms are separable using a Fourier transform [19], yielding two independent terms $I_0(\omega) = |E_{\text{LO}}(\omega)|^2$ and $I_1(\omega) = E^*_{\text{LO}}(\omega)E_{\text{SHG}}(\omega)\exp(-i\phi(\omega))$. $E_{\text{LO}}(\omega)$ is taken to be purely real by defining it to be the reference against which phases are measured. The nonlinear signal E_{SHG} can be written as $E_{\text{SHG}} = \chi^{(2)}_{\text{eff}} E^2_{\text{probe}}$ where $\chi^{(2)}_{\text{eff}}$ is the effective nonlinear susceptibility of the sample leading to second-harmonic-generation, and the LO can be written $E_{\text{LO}} = AE^2_{\text{probe}}$ where A is the effective nonlinear susceptibility of the local-oscillator-generating optic. These expressions are valid in the regime where the probe's spectral phase is approximately the same at both the sample and the local-oscillator-generating crystal. Therefore $\chi^{(2)}_{\text{eff}} = AE_{\text{SHG}}/E_{\text{LO}}$ leading to a single-shot direct measurement of $\chi^{(2)}_{\text{eff}}$ by dividing by $I_0(\omega)$: $\chi^{(2)}_{\text{eff}} = AI_1(\omega)\exp(i\phi(\omega))/I_0(\omega)$. This division allows for some laser-noise removal beyond that described by Levenson and Eesley [13] because the laser noise of the probe is divided out. In practice, A and ϕ_0 are unknown, but τ and ϕ_2 are known to high precision using the spectral phase of $I_1(\omega)$. Meanwhile, in the present experiments the spectral dependence of $\chi^{(2)}_{\text{eff}}$ is negligible. Therefore I define a measured signal $S = \tilde{I}_1/\tilde{I}_0$ proportional to $\chi^{(2)}_{\text{eff}}$, where $\tilde{I}_1 = \int_{\omega_{\text{min}}}^{\omega_{\text{max}}} I_1(\omega)\exp\left(i\tau(\omega - \omega_0) + \frac{i}{2}\phi_2(\omega - \omega_0)^2\right) d\omega$ and $\tilde{I}_0 = \int_{\omega_{\text{min}}}^{\omega_{\text{max}}} I_0(\omega)\, d\omega$. Time-resolved SHG measures the changing $S(t)$ as a function of the time-delay t between a pump pulse creating excited molecules and a probe pulse creating SHG. I mention two extensions of this measurement. First, broadband probe pulses can generate helpful frequency-dependent information about $\chi^{(2)}_{\text{eff}}(\omega)$. Second, establishing an absolute phase relationship between the measured signal S and the nonlinear susceptibility $\chi^{(2)}_{\text{eff}}$ can aid in relating microscopic models

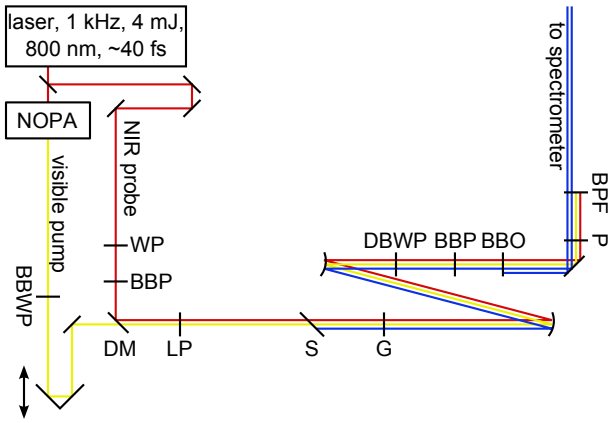

Figure 2.1: Diagram of the heterodyne-detected TRSHG setup. Collinear beams are visually offset for clarity. The visible pump beam (yellow) is time-delayed relative to the 800 nm NIR probe beam (red) with a hollow retroreflector on a motor-controlled stage. The combined beams interact with the sample, generating a 400 nm signal (blue). A second 400 nm beam, the LO (blue), is generated in a nonlinear crystal. The pump and probe are filtered out before the spectrometer. NOPA, non-collinear optical parametric amplifier. BBWP, broad-band (achromatic) half-waveplate designed for 400-700 nm. WP, half-waveplate for 800 nm. BBP, broad-band wire grid polarizer. DM, ultrafast dichroic mirror reflecting 800 nm and transmitting 550-700 nm. LP, long-pass filter with 500 nm cutoff. S, sample oriented 45 degrees to the pump and probe beams. G, removable glass to introduce variable time-delay between signal and local oscillator. DBWP, dual-band waveplate with full-wave retardance at 400 nm and half-wave retardance at 800 nm. BBO, 10-micron-thick beta barium borate crystal, oriented to prevent phase-matching. P, dielectric thin-film polarizer for 400 nm. BPF, bandpass filter centered at 400 nm.

of the surface with measured results [16]. Both of these extensions are discussed in depth by Wilson et al. [18].

The experimental setup is depicted in Figure 2.1. A Spectra-Physics Mai Tai SP™ oscillator seeded a Spectra-Physics Spitfire Pro™ regenerative amplifier yielding 4 mJ, ∼40 fs pulses at 1 kHz centered at 800 nm. This powered a home-built double-pass noncollinear optical parametric amplifier [20] yielding broadband pump pulses tunable over much of the visible spectrum. A portion of the regenerative amplifier's output was the probe pulse. I controlled the relative delay between the pump and probe pulses using a hollow retroreflector on a motorized delay stage. The two beams were collinearly combined with an ultrafast dichroic mirror, and interacted with the sample at 45 degrees using a 5–10 mm diameter round beam with a 2–10 μJ/cm^2 pump fluence and a 50–100 μJ/cm^2 probe fluence. Such large spot sizes allow for acceptable signal strength when using

the extremely low laser fluences and repetition rates required to avoid laser-induced damage and nonlinear kinetics of the organic films being studied. For comparison, many previous experiments had laser fluences and/or laser repetition rates many times larger than the present study [10, 11]. Both pump and probe were *p*-polarized. After the sample, the collinear beams' size was optionally reduced with a Galilean telescope. A controllable-power LO was generated using a dual-band waveplate followed by a polarizer and a beta barium borate (BBO) crystal. The waveplate was full-wave at 400 nm but half-wave near 800 nm and constructed from magnesium fluoride, which is centrosymmetric, preventing second harmonic generation (Karl Lambrecht Corp.). The waveplate and polarizer transmitted a variable amount of 800 nm probe but almost all of the 400 nm signal. A 10 μm-thick BBO generated the LO from the transmitted probe; it was oriented to prevent phase-matching to reduce the amount of LO. A controllable time-delay of $\sim$1 ps between signal and LO was generated, using removable glass windows. The beam was then polarized again, filtered to remove most of the non-400 nm light, focused into a spectrometer (Horiba Jobin-Yvon iHR-320), and detected by a CCD (Princeton Instruments PIXIS-100B with UV coating). The time-resolution of the setup was $\sim$200 fs as measured by a second-order cross-correlation between the pump and probe pulses using a $10\,\mu$m thickness BBO placed at the sample position. This time resolution could easily be improved by compressing the pump pulse, which was not done here to avoid compressor losses. Samples were prepared on an ultra-smooth c-cut sapphire wafer (Precision Micro-Optics LLC) with a 20 nm film of C_{60} capped by 3 nm of boron subphthalocyanine chloride (SubPc). Films were deposited onto room-temperature substrates using vacuum thermal evaporation at a pressure below 5×10^{-7} Torr and at deposition rates of 1 Å/s and 0.5 Å/s for C_{60} and SubPc, respectively. Samples were encapsulated under a pure nitrogen atmosphere using a thin BK7 window and solvent-free UV-cured epoxy to prevent oxygen and moisture induced degradation. The SHG from the non-organic interfaces was negligible.

To demonstrate how the signal-to-noise (S/N) scales with LO power, the S/N at twenty-nine different LO strengths was measured as depicted in Figure 2.2. There are three regimes: a read-noise-dominated regime where the S/N scales with the square root of the LO power, a shot-noise-

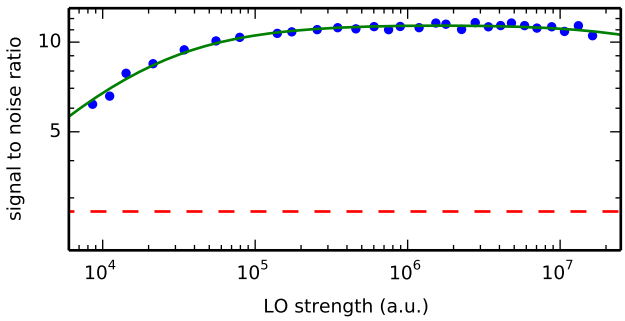

Figure 2.2: Comparison of signal-to-noise with respect to local-oscillator strength on a log-log plot. Blue dots, measured signal-to-noise for different local-oscillator strengths; green solid line, fitted curve to the measured data based on equation 17 of [13]; red dashed line, theoretical signal-to-noise of 2.7 for a similar experiment without a local-oscillator and without stray light. Left side of measured data, read-noise-dominated regime; middle of measured data, shot-noise-dominated regime; right side of measured data, onset of 1/f-noise-dominated regime. Compare to Figure 1 of [13].

dominated regime where the S/N does not vary, and the onset of a 1/f-noise-dominated regime where the S/N scales with the inverse square root of the LO power. This compares favorably with Figure 1 of [13] depicting heterodyned measurements' S/N scaling with LO power. Also depicted is the theoretical S/N of 2.7 for a similar experiment lacking a local-oscillator and without stray light; it was calculated by dividing the SHG signal intensity by the known photodetector read noise. The S/N of any particular TRSHG setup is strongly dependent on photodetector read noise, stray light, photodetector dark current, and whether the measurement is spectrally resolved; using heterodyne detection makes it easier to avoid problems from read noise, stray light, and dark current [13].

As a heterodyned TRSHG demonstration, I scanned the time-delay between pump and probe, measuring the heterodyned signal $S(t)$, as plotted in Figure 2.3. I used a 580 nm pump wavelength to excite the SubPc. Fitting a bi-exponential curve to the complex data finds two rates, $\sim 2\,\mathrm{ps}^{-1}$ and $\sim 0.1\,\mathrm{ps}^{-1}$. The two exponentials both decrease the amplitude, but they change the phase in opposite directions. This may be explained by two dominant SubPc-C_{60} configurations at the interface, with different local environments and therefore different EFISH responses. To understand these results better, I am performing further experimental and theoretical studies on the SubPc-

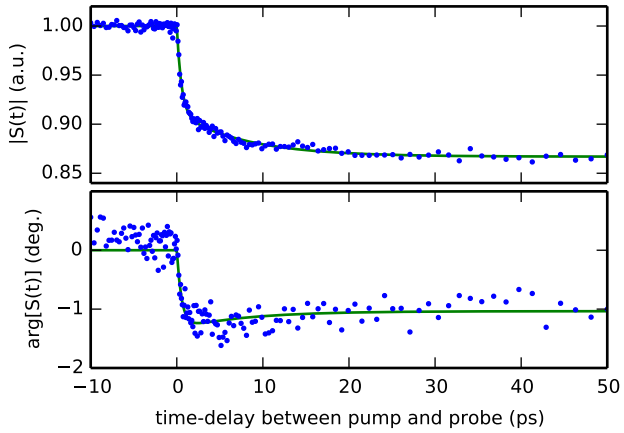

Figure 2.3: Typical measured TRSHG trace $S(t)$, measured relative to the second-harmonic field in the absence of a pump. Top, absolute value; bottom, relative phase in degrees. Blue dots, measured data; green solid line, fitted bi-exponential curve. Fractional noise in absolute signal is less than one percent, and relative noise in measured phase is less than one degree.

C_{60} system. For comparison, [7] reported a $> 10\,\mathrm{ps}^{-1}$ charge-transfer rate in a similar organic photovoltaic system (copper phthalocyanine-C_{60}) using a traditional TRSHG experiment.

In principle the pump could cause phase and amplitude changes in the transmitted probe, and therefore the LO. However, the films' optical density is $\lesssim$0.1, and the pump excites only $\sim$0.1% of the molecules. The pump therefore changes the optical density by $\lesssim 10^{-4}$, changing the LO amplitude by $\lesssim$0.02%, which is much less than the noise floor. The index of refraction of organic films is usually $\sim$2, and since few of the molecules are excited the index of refraction of the film is likely to change by $\lesssim$0.05%. The excited portion of the film is likely $<$5 nm thick, and so the phase-change in the LO due to the pump is $\lesssim$0.005 degrees, which again is much less than the noise floor.

In summary, I have demonstrated a simultaneous phase- and ultrafast time-resolved surface second-harmonic-generation spectrometer in a pump-probe configuration. I employed optical heterodyne detection and spectral interferometry to reduce sensitivity to stray light, to control the noise characteristics, and provide phase resolution. I expect heterodyne-detected TRSHG measurements will be very useful in the study of charge-transfer in organic photovoltaics, and more generally in many kinds of time-resolved surface phenomena [7, 9–12]. It will be particularly use-

ful in systems like organic photovoltaics where the interfacial processes of interest are typically masked by bulk material response.

Acknowledgments

The original version of this chapter may be found at the following reference: Daniel E. Wilcox, Matthew E. Sykes, Andrew Niedringhaus, Max Shtein, and Jennifer P. Ogilvie. Heterodyne-detected and ultrafast time-resolved second-harmonic generation for sensitive measurements of charge transfer. *Optics Letters*, **39**:4274–4277, (2014). http://dx.doi.org/10.1364/OL.39.004274

References

[1] N. C. Giebink, G. P. Wiederrecht, M. R. Wasielewski, and S. R. Forrest. Ideal diode equation for organic heterojunctions. I. Derivation and application. *Physical Review B*, **82**:155305, (2010).

[2] James Kirkpatrick, Panagiotis E. Keivanidis, Annalisa Bruno, Fei Ma, Saif A. Haque, Arkady Yarstev, Villy Sundstrom, and Jenny Nelson. Ultrafast transient optical studies of charge pair generation and recombination in poly-3-hexylthiophene(P3ht):[6,6]phenyl C61 butyric methyl acid ester (PCBM) blend films. *The Journal of Physical Chemistry B*, **115**:15174–80, (2011).

[3] Fabian Etzold, Ian A. Howard, Nina Forler, Don M. Cho, Michael Meister, Hannah Mangold, Jie Shu, Michael Ryan Hansen, Klaus Müllen, and Frédéric Laquai. The effect of solvent additives on morphology and excited-state dynamics in PCPDTBT:PCBM photovoltaic blends. *Journal of the American Chemical Society*, **134**:10569–83, (2012).

[4] Sanjeev Singh and Zeev Vardeny. Ultrafast transient spectroscopy of polymer/fullerene blends for organic photovoltaic applications. *Materials*, **6**:897–910, (2013).

[5] Ajay Ram Srimath Kandada, Giulia Grancini, Annamaria Petrozza, Stefano Perissinotto, Daniele Fazzi, Sai Santosh Kumar Raavi, and Guglielmo Lanzani. Ultrafast energy transfer in ultrathin organic donor/acceptor blend. *Scientific Reports*, **3**:2073, (2013).

[6] B. Bernardo, D. Cheyns, B. Verreet, R. D. Schaller, B. P. Rand, and N. C. Giebink. Delocalization and dielectric screening of charge transfer states in organic photovoltaic cells. *Nature Communications*, **5**:3245, (2014).

[7] L. G. Kaake, A. Jailaubekov, K. J. Williams, and X.-Y. Zhu. Probing ultrafast charge sep-

aration at organic donor/acceptor interfaces by a femtosecond electric field meter. *Applied Physics Letters*, **99**:083307, (2011).

[8] Robert W. Boyd. *Nonlinear Optics*. Academic Press, third edition, (2008).

[9] C. V. Shank, R. Yen, and C. Hirlimann. Femtosecond-time-resolved surface structural dynamics of optically excited silicon. *Physical Review Letters*, **51**:900–902, (1983).

[10] Juliette M. Lantz and Robert M. Corn. Time-resolved optical second harmonic generation measurements of picosecond band flattening processes at single crystal TiO2 electrodes. *The Journal of Physical Chemistry*, **98**:9387–9390, (1994).

[11] X. Shi, E. Borguet, A. N. Tarnovsky, and K. B. Eisenthal. Ultrafast dynamics and structure at aqueous interfaces by second harmonic generation. *Chemical Physics*, **205**:167–178, (1996).

[12] Askat E. Jailaubekov, Adam P. Willard, John R. Tritsch, Wai-Lun Chan, Na Sai, Raluca Gearba, Loren G. Kaake, Kenrick J. Williams, Kevin Leung, Peter J. Rossky, and X.-Y. Zhu. Hot charge-transfer excitons set the time limit for charge separation at donor/acceptor interfaces in organic photovoltaics. *Nature Materials*, **12**:66–73, (2013).

[13] M. D. Levenson and G. L. Eesley. Polarization selective optical heterodyne detection for dramatically improved sensitivity in laser spectroscopy. *Applied Physics*, **19**:1–17, (1979).

[14] P. T. Wilson, Y. Jiang, O. A. Aktsipetrov, E. D. Mishina, and M. C. Downer. Frequency-domain interferometric second-harmonic spectroscopy. *Optics Letters*, **24**:496–8, (1999).

[15] K. J. Veenstra, A. V. Petukhov, A. P. de Boer, and Th. Rasing. Phase-sensitive detection technique for surface nonlinear optics. *Physical Review B*, **58**:R16020–R16023, (1998).

[16] R. K. Chang, J. Ducuing, and N. Bloembergen. Relative phase measurement between fundamental and second-harmonic light. *Physical Review Letters*, **15**:6–8, (1965).

[17] K. Kemnitz, K. Bhattacharyya, J. M. Hicks, G. R. Pinto, and K. B. Eisenthal. The phase of second-harmonic light generated at an interface and its relation to absolute molecular orientation. *Chemical Physics Letters*, **131**:285–290, (1986).

[18] P. T. Wilson, Y. Jiang, R. Carriles, and M. C. Downer. Second-harmonic amplitude and phase spectroscopy by use of broad-bandwidth femtosecond pulses. *Journal of the Optical Society of America B*, **20**:2548, (2003).

[19] L. Lepetit, G. Chériaux, and M. Joffre. Linear techniques of phase measurement by femtosecond spectral interferometry for applications in spectroscopy. *Journal of the Optical Society of America B*, **12**:2467, (1995).

[20] E. Riedle, M. Beutter, S. Lochbrunner, J. Piel, S. Schenkl, S. Spörlein, and W. Zinth. Generation of 10 to 50 fs pulses tunable through all of the visible and the NIR. *Applied Physics B*, **71**:457–465, (2000).

[21] James McIver, Changmin Lee, Darius Torchinsky, and Nuh Gedik. Ultrafast time- and phase-resolved second harmonic generation. In *APS March Meeting*, page BAPS.2013.MAR.Z23.10, (2013). URL `http://meetings.aps.org/link/BAPS.2013.MAR.Z23.10`.

Chapter 3

Ultrafast charge-transfer dynamics at the boron subphthalocyanine chloride / C_{60} heterojunction: Comparison between experiment and theory

Photoinduced charge-transfer is a key component of many chemically-, biologically- and technologically-relevant processes, including photocatalysis, photovoltaics and photosynthesis. In the case of organic photovoltaics, light absorption by the electron donor or acceptor layer eventually triggers the creation of a charge separated state across the donor/acceptor interface, which upon dissociation of the interfacial electron-hole pair gives rise to an electrical current. Similarly, photosynthetic reactions correspond to transforming the energy of the absorbed photons into that of charge separated states, which can drive life-sustaining reactions such as water splitting [1].

A variety of experimental methods have been used to measure charge-transfer rates. For example, ultrafast transient absorption (also called pump-probe or photoinduced absorption) and time-resolved fluorescence (or photoluminescence) spectroscopies have been used to track spectral signatures attributed to charge-transfer or charge separated states [2–6]. Near infrared transient absorption in organic photovoltaic systems is commonly attributed to charge-transfer states [2–4]. Unfortunately, charge-transfer states are often dark [7]. Furthermore, the signal obtained via such methods as transient absorption pump-probe spectroscopy correspond to a third-order optical response, which is dominated by the bulk material. This makes it difficult to resolve contributions from interfacial charge-transfer and charge separation processes [8].

Recently, a number of groups have employed time-resolved second harmonic generation (TR-SHG) as a more direct way of probingcharge-transfer dynamics in organic photovoltaic materials [8–10]. Importantly, the second harmonic generation (SHG) signal vanishes in centrosymmetric materials [11], thereby making it insensitive to bulk processes, and highly sensitive to processes that occur at the donor/acceptor interface, where the centrosymmetry is broken. TRSHG can be used to provide an interface-specific measure of charge-transfer using electric field induced second harmonic generation (EFISH) [8]. The latter is a four-wave mixing nonlinear optical phenomenon, where a quasi-static electric field E_{DC} allows an optical signal P^{NL} to be produced as the second harmonic of a probe pulse: $P^{\mathrm{NL}} = \chi^{(3)} E_{\mathrm{DC}} E^2_{\mathrm{probe}}$. Charge-transfer at the interface then creates the quasi-static field E_{DC}, which leads to a measurable EFISH signal.

The electronic structure of excited charge-transfer states of complex molecular systems can be calculated by high quality many-body expansion methods, for example using the GW approximation with the Bethe-Salpeter (BSE) equation [12–15]. However, the prohibitive computational cost of such techniques requires using more feasible alternatives such as time-dependent density functional theory (TD-DFT). Indeed, implemented with recently developed range-separated hybrid (RSH) functionals [16–21], TD-DFT was shown to reproduce GW-BSE energies [13, 22]. Furthermore, combining TD-DFT/RSH with a description of the electrostatic environment as a polarizable dielectric continuum was recently shown to yield charge-transfer states whose energies are in good agreement with experiment [23–25].

Most computational studies on charge-transfer rates in organic photovoltaic materials [26–29] are based on the semiclassical Marcus picture of photoinduced charge-transfer [30–32]. However, Marcus theory relies on a number of simplifying assumptions that do not hold in general when considering organic semiconducting materials [33–35]. Marcus theory can be derived from the more general fully quantum-mechanical Fermi's golden rule (FGR) expression for the charge-transfer rate constant [36–40]. However, doing so requires imposing both the high-temperature and short time limits. Importantly, since charge-transfer in organic photovoltaic materials may occur in the (far) inverted regime, nuclear tunneling can become a dominant mechanism for electronic transi-

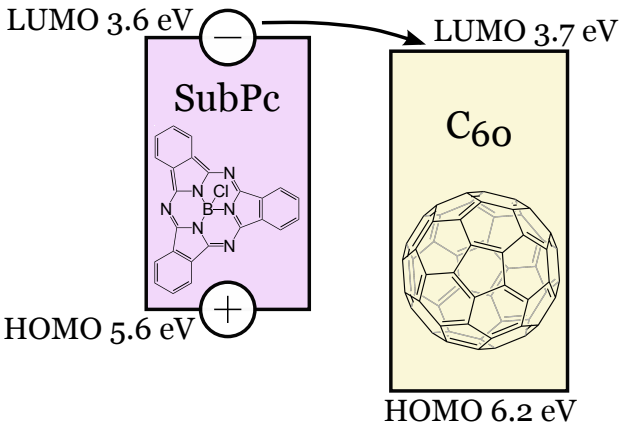

Figure 3.1: Depiction of the charge-transfer process under investigation. Boron subphthalocyanine chloride (SubPc) absorbs light, creating a bound electron-hole pair, or exciton. In proximity to a C_{60} molecule, the electron is donated to the C_{60}, generating a charge-transfer state.

tions due to enhanced overlap between the nuclear wavefunctions [41, 42]. Furthermore, the above mentioned short-time expansion may not be valid. Indeed, my collaborators Lee et al. have recently demonstrated the importance in using the less approximate fully quantum-mechanical FGR expression for calculating charge-transfer rates. The calculated FGR rate constants thus obtained were found to be in good agreement with corresponding experimental values, whereas the classical Marcus rate constants were found to significantly underestimate the experimental values [33–35].

In this chapter, I study a model system of an organic photovoltaic heterojunction, in which boron subphthalocyanine chloride (SubPc) and C_{60} function as the electron donor and acceptor, respectively. Upon photoexcitation, the SubPc transfers an electron to the C_{60}, generating a charge-transfer state. To directly observe the charge-transfer, I used my recently-developed heterodyne-detected TRSHG (hTRSHG) spectroscopy [43]. Adding heterodyne detection to TRSHG decreases sensitivity to read noise, dark current, and stray light. It also allows both the amplitude and the phase of the SHG to be directly detected, which can aid physical understanding; for example, providing information about molecular orientations or the direction of charge-transfer [43].

A detailed description of my hTRSHG setup was published previously [43]. For this experiment, a 580 nm pump pulse created a subpopulation of excited molecules, after which an 800 nm

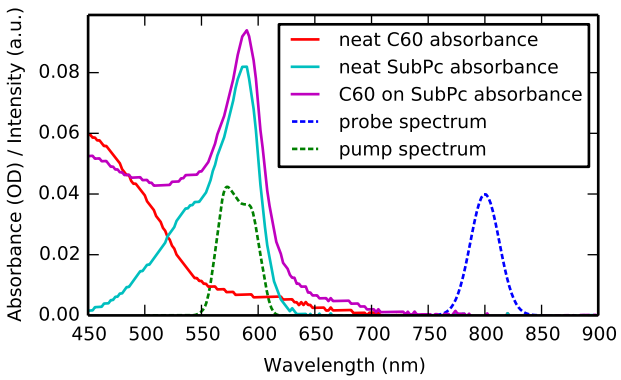

Figure 3.2: Laser spectra and samples' absorbance. The probe pulse, centered at 800 nm, is well-separated from main absorption. The pump pulse, centered at 580 nm, maximizes absorption from the SubPc.

probe pulse was used to probe the electric field at the interface, and thereby charge-transfer, as a function of the time-delay between pump and probe pulses. I found that very low laser fluences were necessary to avoid higher-order processes such as exciton-exciton annihilation and laser-induced aging, as discussed in detail in the supporting information given in Appendix A. I therefore reduced the probe fluence to 50 μJ/cm^2 and the pump fluence to 2 μJ/cm^2; I estimate that under these conditions the pump excites $\sim$0.1% of the SubPc molecules. Three types of samples were prepared on an ultra-smooth c-cut sapphire wafer (Precision Micro-Optics LLC): (1) A 3 nm film of SubPc capped by 20 nm of C_{60}; (2) A neat 20 nm film of C_{60}; (3) A neat 3 nm film of SubPc. Films were deposited onto room-temperature substrates using vacuum thermal evaporation at a pressure below 5×10^{-7} Torr and at deposition rates of 1 Å/s and 0.5 Å/s for C_{60} and SubPc, respectively. Samples were encapsulated under a pure nitrogen atmosphere using a BK7 window and solvent-free UV-cured epoxy to prevent oxygen- and moisture-induced degradation.

Figure 3.2 shows the pump and probe laser spectra, and the samples' linear absorption spectra. The 580 nm pump wavelength primarily excites the SubPc molecules. The probe pulse is well-separated from absorption and so primarily interacts nonlinearly, producing SHG. Here I report two representative sets of bilayer charge-transfer data, taken on different days, with fresh samples. A separate hTRSHG trace was taken with the probe pulse in the *s* and *p* polarizations. I best-fit the

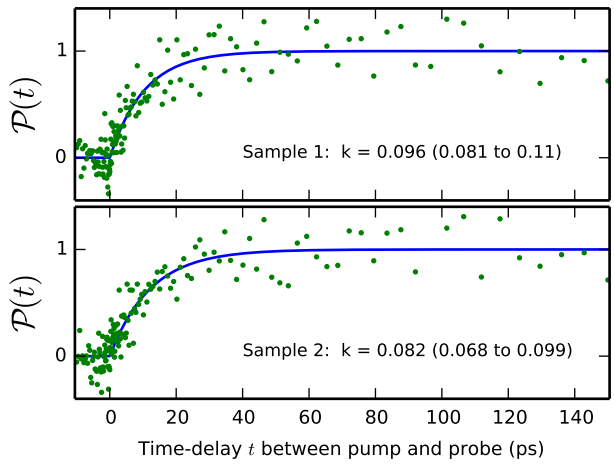

Figure 3.3: Measured and fitted principal projection $\mathcal{P}$ of the hTRSHG data. Green dots, measured data. Blue line, fitted single-exponential curve. The measurement was repeated on different days with fresh samples; the fitted charge-transfer rate k is shown in ps^{-1} with 95% confidence intervals. Top subfigure, bilayer sample 1; bottom subfigure, bilayer sample 2. Data from neat films not shown due to absence of dynamics.

data using a single-exponential model, with the same rate k for both polarizations:

$$S_i(t) = A_i + B_i\,\theta(t)\,\left[1 - \exp(-kt)\right]. \tag{3.1}$$

Here, $S_i(t)$ represents the measured complex hTRSHG signal as a function of polarization i and pump-probe relative time delay t. A_i represents the ground-state signal ($t < 0$) and B_i represents the change in SHG due to the presence of the pump, in the limit of large t. Both A_i and B_i are complex and depend on the polarization i. $\theta(t)$ is the Heaviside step function. k is the (real) rate constant, and does not depend on polarization. I used the `curve_fit` function in the open-source `scipy.optimize` module [44] to perform the fitting. The unknowns in the fit were A_i, B_i, and k. The measured data and their fits are shown in Figure 3.3 by plotting the principal projection $\mathcal{P}$ of the data onto the $\vec{A}$–$\vec{B}$ line, as defined in the supporting information given in Appendix A. This projection starts at 0 before time-zero, and converges to 1 in the limit of large pump-probe time-delay. I found that this projection captured the majority of the information in the data; the data-components orthogonal to this projection were dominated by noise. The fitted time-constants and associated confidence intervals for the bilayer films are shown in Figure 3.3, indicating that

the charge-transfer rate is $k \sim 0.1\,\mathrm{ps}^{-1}$, reasonably consistently across the two bilayer films. This rate is likely an average charge-transfer rate, since different individual molecules in different local environments are expected to have different charge-transfer rates. Control studies of neat films showed no changes in the SHG due to the pump, indicating that no charge-transfer occurred.

For the theoretical calculations, my collaborators Lee et al. considered two representative molecular models of likely interfacial configurations based on optimized donor-acceptor dimers in a dielectric continuum model, namely the hollow and on-top configurations, shown in the inset of Figure 3.4 [45]. The irregular shape of SubPc suggests that interfacial donor-acceptor geometries in actual thin films might deviate from optimal geometries, where they are expected to be less tightly packed. I therefore expect the calculated charge-transfer rates to serve as upper bounds to experimentally measured rates.

The photoinduced charge transfer involves coupling a dark charge transfer state to an absorbing bright state. In the system considered here, the electron is transferred from SubPc to C_{60} as illustrated by the detachment and attachment electron densities shown in Figure 3.4. However, it should be noted that some of the donor-excited states of the on-top configuration already exhibit charge-transfer character due to some delocalization across the donor and acceptor regions.

Since a TRSHG measurement tracks the electric field at the interface, a comparison between the experimental and computational results can be made by following the time-dependent electric dipole moment $\mu(t)$,

$$\mu(t) = \sum_i \mu_i P_i(t). \tag{3.2}$$

Here, $P_i(t)$ is the evolving occupancy of excited state i, and the electric dipole moment μ_i for state i is given by $\mu_i = q^i_{\mathrm{D}}|\mathbf{r}^i_{\mathrm{D}} - \mathbf{r}^i_{\mathrm{A}}|$, where $q^i_{\mathrm{D}}(= -q^i_{\mathrm{A}})$ is the total Mulliken charge on donor (D) molecule obtained from the TD-DFT calculation and $\mathbf{r}^i_{\mathrm{D/A}}$ is the center of charge of D/A molecules defined by

$$\mathbf{r}^i_{\mathrm{D/A}} = \frac{\sum_{j\in \mathrm{D/A}} |q^i_j|\mathbf{r}^i_j}{\sum_{j\in \mathrm{D/A}} |q^i_j|}. \tag{3.3}$$

The excited states' occupancies, $P_i(t)$, were obtained by solving a Master equation under the

assumption that the initial state is dominated by states that absorb within the pump bandwidth:

$$\dot{P}_i(t) = \sum_{j \neq i} \left[-k_{ji} P_i(t) + k_{ij} P_j(t) \right], \text{ where } P_i(t=0) \equiv \frac{|OS_i|}{\sum_j |OS_j|}, \sum_i P_i(t) = 1. \tag{3.4}$$

Here, k_{ji} is the FGR rate constant for the electronic transition from state i to state j, and OS_i is the oscillator strength of excited state i. My collaborators Lee et al. used an effective oscillator strength of zero ($OS_i = 0$) for all of the charge-transfer states, including the bright ones, since my pump laser pulse was relatively narrowband and not resonant with the charge-transfer states.

The FGR rate constant for an electronic transition from the electronic state b to a is given by [36–40]:

$$k_{a \leftarrow b} = \frac{|V_{ba}|^2}{\hbar^2} \int_{-\infty}^{\infty} dt e^{i\omega_{ba}t} F(t), \tag{3.5}$$

where $F(t) = \exp\left[\sum_{\alpha=1}^{N} \left[-S_\alpha(2n_\alpha + 1) + S_\alpha[(n_\alpha + 1)e^{-i\omega_\alpha t} + n_\alpha e^{i\omega_\alpha t}]\right]\right]$. Here, V_{ba}, $\omega_{ba} = (E_b - E_a)/\hbar$, $\{\omega_\alpha\}$ and $\left\{n_\alpha = [e^{\frac{\hbar\omega_\alpha}{k_B T}} - 1]^{-1}\right\}$ are the electronic coupling coefficient, transition frequency, normal-mode frequencies and thermal equilibrium occupancies, respectively. The Huang-Rhys factor S_α [46] represents the electron-vibration coupling strength, which is obtained by projecting the displacement between the initial and final equilibrium geometries onto the normal modes of the ground state.

Density functional theory (DFT) was employed for the ground-state, time-dependent density functional theory (TD-DFT) for excited states, and charge-constrained density functional theory (C-DFT) [47] for determining the CT state geometry and energy as affected by the electrostatic environment [45]. All the calculations were performed with the 6-31G* basis set. Geometry optimization of the ground and the CT states was based on the ωB97X-D dispersion-corrected functional, designed for accurately describing non-covalent interactions [48, 49]. The optimal geometries of the π-π^* excited state were assumed to be the same as the ground state optimal geometry. TD-DFT gas-phase calculations were based on the range-separated hybrid functional of Baer-Neuhauser-Livshits (BNL) [17, 18], designed to accurately describe CT states by employing a tunable range-separation parameter γ [17–21, 23]. My collaborators Lee et al. employed the

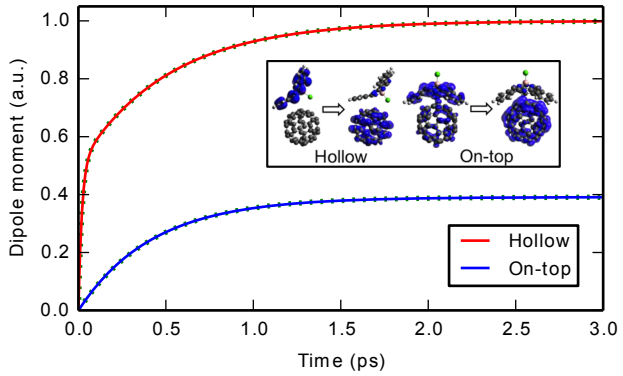

Figure 3.4: Calculated electric dipole moment $\mu(t)$ as a function of time for two SubPc/C_{60} interface configurations. Red solid line, hollow configuration; blue solid line, on-top configuration. Green dotted lines, best-fit curves. Inset shows the detachment and attachment of electron densities upon photoexcitation, indicating the electron transfer from SubPc to C_{60}. The hollow best-fit curve was bi-exponential, with a 51 ps^{-1} component and a 2.0 ps^{-1} component. The on-top best-fit curve was single-exponential, showing an average charge-transfer rate of 2.3 ps^{-1}.

$J^2(\gamma)$ range-separation parameter tuning scheme [50]. Finally, the electronic coupling coefficient between electronic states, V_{ba}, was obtained via the fragment-charge difference (FCD) method [51]. The effect of the solid-state environment was modeled by treating it as a dielectric medium when performing the geometry optimization of the ground and the CT states. The value of the dielectric constant used was 4.2, which is close to the value of this parameter in SubPc (3.9) [52] and C_{60} (4.0-4.5) [53–56]. To this end, my collaborators Lee et al. employed the conductor-like polarizable continuum model (CPCM) [57] with the switching/Gaussian (SWIG) method [58–60] for surface discretization.

The FGR rate constants for the electronic transitions from the bright excited states to the (bright or dark) charge-transfer states are in the range of 0.02–27 ps^{-1} for the hollow configuration and 0.1–2.7 ps^{-1} for the on-top configuration [45]. In Figure 3.4 I plot the resulting total dipole moment $\mu(t)$, normalizing with respect to the steady-state dipole moment for the hollow configuration. The hollow configuration had a stronger dipole moment compared to the on-top configuration, due to its stronger charge-transfer character and longer donor-acceptor separation. By fitting the dipole moment kinetics to multi-exponential curves, two exponential components with rate constants of 51 ps^{-1} and 2.0 ps^{-1} were indicated in the case of the hollow configuration. Only a single expo-

nential with a 2.3 ps^{-1} rate constant was indicated in the case of the on-top configuration.

The FGR and classical Marcus theory charge-transfer rate constants are roughly comparable in this system [45], which is reasonable considering the charge-transfer reaction is only barely in the inverted region [45]. However, the recombination transitions from the CT states back to the ground state occur in the far-inverted region [45]. In the hollow configuration, the recombination FGR rate constants range approximately from 10^5 to 10^8 s^{-1}, which is orders of magnitude faster than the corresponding classical Marcus theory rate constants [45]. Since I did not detect charge recombination within the time scale of my experiment, I can establish a lower bound for the charge recombination rate constant at approximately 10^3 s^{-1}, based on the laser repetition rate (500 Hz) and the fact that I did not observe an EFISH background for $t < 0$. Thus, the calculated FGR recombination rate constants are at least consistent with experiment.

As expected, the $k \sim 2$ ps^{-1} FGR charge-transfer rate constants are somewhat faster than the corresponding experimentally measured value, $k \sim 0.1 ps^{-1}$. This result is consistent with the view that the calculated FGR rate constants represent an upper bound for the experimentally measured rate constants. First, I note that variations in measured charge-transfer rate constants were observed from one sample to another, where differences of a factor of three were observed. Second, the irregular shape of SubPc suggests that interfacial donor-acceptor geometries in actual thin film samples would most likely deviate from the dimer optimal geometries on which the calculations were performed. Third, charge-transfer for the hollow configuration was found to follow bi-exponential kinetics, with fast ($\sim$50 ps^{-1}) and slow ($\sim$2 ps^{-1}) components, while charge-transfer in the on-top configuration could be described by a single $\sim$2 ps^{-1} rate constant. Thus, a faster CT process can be attained with samples in which the interface is dominated by the hollow configuration and where the photoexcitation is tuned to selectively populate the relevant excited states.

In summary, I compared experimentally measured and theoretically predicted charge-transfer rate constants for the SubPc/C_{60} electron donor/acceptor system used in organic photovoltaics. My combined experimental and computational study represents a first step towards understanding the

complex relationship between molecular interfacial structure and charge transfer dynamics. The experimentally measured value was $k \sim 0.1\,\mathrm{ps}^{-1}$, while the computational value was $k \sim 2\mathrm{ps}^{-1}$. Considering the approximations underlying the theoretical model and experimental uncertainties regarding sample preparation and spectroscopic measurements, I believe that the agreement between experiment and theory is reasonable. In addition, it is likely that charge-transfer rate constants calculated using optimal dimer geometries represent an upper bound for the experimentally measured rate constants. In particular, I find a fundamental difference in the dynamics between the two optimal geometries considered, namely a bi-exponential behavior in the hollow geometry and a single exponential in the on-top geometry. Thus, measurements of the dipole moment can be used to resolve the dominant form of the molecular interface in an organic photovoltaic sample. Further advances of our understanding of charge-transfer dynamics in such systems towards improving the agreement between experiment and theory would require improving both the characterization of the interface structure and the modeling of the charge-transfer rates. Work towards achieving those objectives is underway.

Acknowledgments

The original version of this chapter may be found at the following reference: Daniel E. Wilcox, Myeong H. Lee, Matthew E. Sykes, Andrew Niedringhaus, Eitan Geva, Barry D. Dunietz, Max Shtein, and Jennifer P. Ogilvie. Ultrafast charge-transfer dynamics at the boron subphthalocyanine chloride / C_{60} heterojunction: Comparison between experiment and theory. As first submitted to *The Journal of Physical Chemistry Letters*, (2014).

References

[1] Robert E. Blankenship. *Molecular Mechanisms of Photosynthesis*. Wiley-Blackwell, (2002).

[2] James Kirkpatrick, Panagiotis E. Keivanidis, Annalisa Bruno, Fei Ma, Saif A Haque, Arkady Yarstev, Villy Sundstrom, and Jenny Nelson. Ultrafast transient optical studies of charge pair generation and recombination in poly-3-hexylthiophene(P3ht):[6,6]phenyl C61 butyric

methyl acid ester (PCBM) blend films. *The Journal of Physical Chemistry B*, **115**:15174–80, (2011).

[3] Fabian Etzold, Ian A Howard, Nina Forler, Don M Cho, Michael Meister, Hannah Mangold, Jie Shu, Michael Ryan Hansen, Klaus Müllen, and Frédéric Laquai. The effect of solvent additives on morphology and excited-state dynamics in PCPDTBT:PCBM photovoltaic blends. *Journal of the American Chemical Society*, **134**:10569–83, (2012).

[4] Sanjeev Singh and Zeev Vardeny. Ultrafast Transient Spectroscopy of Polymer/Fullerene Blends for Organic Photovoltaic Applications. *Materials*, **6**:897–910, (2013).

[5] Ajay Ram Srimath Kandada, Giulia Grancini, Annamaria Petrozza, Stefano Perissinotto, Daniele Fazzi, Sai Santosh Kumar Raavi, and Guglielmo Lanzani. Ultrafast energy transfer in ultrathin organic donor/acceptor blend. *Scientific Reports*, **3**:2073, (2013).

[6] B Bernardo, D Cheyns, B Verreet, R D Schaller, B P Rand, and N C Giebink. Delocalization and dielectric screening of charge transfer states in organic photovoltaic cells. *Nature Communications*, **5**:3245, (2014).

[7] R J Magyar and S Tretiak. Dependence of Spurious Charge-Transfer Excited States on Orbital Exchange in TDDFT: Large Molecules and Clusters. *Journal of Chemical Theory and Computation*, **3**:976–987, (2007).

[8] L. G. Kaake, A. Jailaubekov, K. J. Williams, and X.-Y. Zhu. Probing ultrafast charge separation at organic donor/acceptor interfaces by a femtosecond electric field meter. *Applied Physics Letters*, **99**:083307, (2011).

[9] D. Amarasinghe Vithanage, A. Devižis, V. Abramavičius, Y. Infahsaeng, D. Abramavičius, R. C. I. MacKenzie, P. E. Keivanidis, A. Yartsev, D. Hertel, J. Nelson, V. Sundström, and V. Gulbinas. Visualizing charge separation in bulk heterojunction organic solar cells. *Nature Communications*, **4**:2334, (2013).

[10] Askat E. Jailaubekov, Adam P. Willard, John R. Tritsch, Wai-Lun Chan, Na Sai, Raluca Gearba, Loren G. Kaake, Kenrick J. Williams, Kevin Leung, Peter J. Rossky, and X.-Y. Zhu. Hot charge-transfer excitons set the time limit for charge separation at donor/acceptor interfaces in organic photovoltaics. *Nature Materials*, **12**:66–73, (2013).

[11] Robert W. Boyd. *Nonlinear Optics*. Academic Press, third edition, (2008).

[12] B. Baumeier, D. Andrienko, and M. Rohlfing. Frenkel and charge-transfer excitations in donor-acceptor complexes from many-body greens' functions theory. *J. Chem. Theory Comput.*, **8**:2790–2795, (2012).

[13] I. Duchemin, T. Deutsch, and X. Blase. Short-range to long-range charge-transfer excitations in the zincbacteriochlorin-bacteriochlorin complex: A bethe-salpeter study. *Phys. Rev. Lett.*, **109**:167801, (2012).

[14] J.M. Garcia-Lastra and K.S. Thygesen. Renormalization of optical excitations in molecules near a metal surface. *Phys. Rev. Lett.*, **106**, (2011).

[15] X. Blase and C. Attaccalite. Charge-transfer excitations in molecular donor-acceptor complexes within the many-body bethe-salpeter approach. *Appl. Phys. Lett.*, **99**:171909, (2011).

[16] A. Dreuw, J. L. Weisman, and M. Head-Gordon. Long-range charge-transfer excited states in time-dependent density functional theory require non-local exchange. *J. Chem. Phys.*, **119**:

2943–2946, (2003).

[17] R. Baer and D. Neuhauser. Density functional theory with correct long-range asymptotic behavior. *Phys. Rev. Lett.*, **94**:043002, (2005).

[18] E. Livshits and R. Baer. A well-tempered density functional theory of electrons in molecules. *Phys. Chem. Chem. Phys.*, **9**:2932–2941, (2007).

[19] T. Stein, L. Kronik, and R. Baer. Reliable prediction of charge transfer excitations in molecular complexes using time-dependent density functional theory. *J. Am. Chem. Soc.*, **131**: 2818–2820, (2009).

[20] T. Stein, H. Eisenberg, L. Kronik, and R. Baer. Fundamental gaps in finite systems from eigenvalues of a generalized Kohn-sham method. *Phys. Rev. Lett.*, **105**:266802, (2010).

[21] T. Stein, L. Kronik, and R. Baer. Prediction of charge-transfer excitations in coumarin-based dyes using a range-separated functional tuned from first principles. *J. Chem. Phys.*, **131**: 244119, (2009).

[22] A. K. Manna and B. D. Dunietz. Charge-transfer rate constants in zinc-porphyrin-porphyrin-derived dyads: A fermi golden rule first-principles-based study. *J. Chem. Phys.*, **141**:121102, (2014).

[23] S. Zheng, H. Philips, E. Geva, and B. D. Dunietz. *Ab initio* study of the emissive charge-transfer states of solvated chromophore-functionalized silsesquioxanes. *J. Am. Chem. Soc.*, **134**:6944–6947, (2012).

[24] S. Zheng, E. Geva, and B. D. Dunietz. Solvated charge transfer states of functionalized anthracene and tetracyanoethylene dimers: A computational study based on a range-separated hybrid functional and charge constrained self-consistent field with switching gaussian polarized continuum models. *J. Chem. Theory Comput.*, **9**:1125–1131, (2013).

[25] H. Phillips, Z. Zheng, E. Geva, and B. D. Dunietz. Orbital gap predictions for rational design of organic photovoltaic materials. *Org. Electron.*, **15**:1509–1520, (2014).

[26] Y. Yi, V. Coropceanu, and J.-L. Brédas. Exciton-dissociation and charge-recombination processes in pentacene/c_{60} solar cells: Theoretical insight into the impact of interface geometry. *J. Am. Chem. Soc.*, **131**:15777–15783, (2009).

[27] Y. Yi, V. Coropceanu, and J.-L. Brédas. A comparative theoretical study of exciton-dissociation and charge-recombination processes in oligothiophene/fullerene and oligothiophene/perylenediimide complexes for organic solar cells. *J. Mater. Chem.*, **21**:1479–1486, (2011).

[28] A. Zhugayevych, O. Postupna, R. C. Bakus II, G. C. Welch, G. C. Bazan, and S. Tretiak. *J. Phys. Chem. C*, **117**:4920–4930, (2013).

[29] C. Leng, H. Quin, Y. Si, and Y. Zhao. Theoretical prediction of the rate constants for exciton dissociation and charge recombination to a triplet state in pcpdtbt with different fullerene derivatives. *J. Phys. Chem. C*, **118**:1843–1855, (2014).

[30] R. A. Marcus. On the theory of oxidation-reduction reactions involving electron transfer. I. *J. Chem. Phys.*, **24**:966, (1956).

[31] R. A. Marcus. Electrostatic free energy and other properties of states having nonequilibrium

polarization. I. *J. Chem. Phys.*, **24**:979, (1956).

[32] R. A. Marcus. Electron transfer reactions in chemistry. Theory and experiment. *Rev. Mod. Phys.*, **65**:599–610, (1993).

[33] M. H. Lee, B. D. Dunietz, and E. Geva. Calculation from first principles of intramolecular golden-rule rate constants for photo-induced electron transfer in molecular donor-acceptor systems. *J. Phys. Chem. C*, **117**:23391–23401, (2013).

[34] M. H. Lee, B. D. Dunietz, and E. Geva. Calculation from first principles of golden-rule rate constants for photo-induced subphthalocyanine/fullerene interfacial charge transfer and recombination in organic photovoltaic cells. *J. Phys. Chem. C*, **118**:9780–9789, (2014).

[35] M. H. Lee, B. D. Dunietz, and E. Geva. Donor-to-donor vs. donor-to-acceptor interfacial charge transfer states in the phthalocyanine-fullerene organic photovoltaic system. *J. Phys. Chem. Lett.*, **5**:3810–3816, (2014).

[36] A. Nitzan. *Chemical Dynamics in Condensed Phases*. Oxford University Press, New York, (2006).

[37] N. R. Kestner, J. Logan, and J. Jortner. Thermal electron transfer reactions in polar solvents. *J. Phys. Chem.*, **78**:2148–2166, (1974).

[38] J. Jortner and M. Bixon. Intramolecular vibrational excitations accompanying solvent-controlled electron transfer reactions. *J. Chem. Phys.*, **88**:167, (1988).

[39] R. D. Coalson, D. G. Evans, and A. Nitzan. A nonequilibrium golden rule formula for electronic state populations in nonadiabatically coupled systems. *J. Chem. Phys.*, **101**:436, (1994).

[40] A. J. Leggett, S. Chakravarty, A. T. Dorsey, Matthew P. A. Fisher, Anupam Garg, and W. Zwerger. Dynamics of the dissipative two-state system. *Rev. Mod. Phys.*, **59**:1–85, (1987).

[41] Don De Vault and Britton Chance. Studies of photosynthesis using a pulsed laser. *Biophys. J.*, **6**:825–847, (1996).

[42] Paul F. Barbara, Thomas J. Meyer, and Mark A. Ratner. Contemporary issues in electron transfer research. *J. Phys. Chem.*, **100**:13148–13168, (1996).

[43] Daniel E. Wilcox, Matthew E. Sykes, Andrew Niedringhaus, Max Shtein, and Jennifer P. Ogilvie. Heterodyne-detected and ultrafast time-resolved second-harmonic generation for sensitive measurements of charge transfer. *Optics Letters*, **39**:4274, (2014).

[44] The Scipy community. Optimization and root finding (scipy.optimize). URL `http://docs.scipy.org/doc/scipy/reference/optimize.html`.

[45] Myeong H. Lee, Eitan Geva, and Barry D. Dunietz. Calculation from First-Principles of Golden Rule Rate Constants for Photoinduced Subphthalocyanine/Fullerene Interfacial Charge Transfer and Recombination in Organic Photovoltaic Cells. *The Journal of Physical Chemistry C*, **118**:9780–9789, (2014).

[46] K. Huang and A. Rhys. Theory of light absorption and non-radiative transitions in f-centres. *Proc. R. Soc. Lond. A*, **204**:406–423, (1950).

[47] Q. Wu and T. Van Voorhis. Direct optimization method to study constrained systems within density-functional theory. *Phys. Rev. A*, **72**:024502, (2005).

[48] J.-D. Chai and H.-G. Martin. Systematic optimization of long-range corrected hybrid density functionals. *J. Chem. Phys.*, **128**:084106, (2008).

[49] J.-D. Chai and H.-G. Martin. Long-range corrected hybrid density functionals with damped atom-atom dispersion corrections. *Phys. Chem. Chem. Phys.*, **10**:6615–6620, (2008).

[50] N. Kuritz, T. Stein, R. Baer, and L. Kronik. Charge-transfer-like $\pi \rightarrow \pi^*$ excitations in time-dependent density functional theory: A conundrum and its solution. *J. Chem. Theory Comput.*, **7**:2408–2415, (2011).

[51] A. A. Voityuk and N. Rösch. Fragment charge difference method for estimating donor-acceptor electronic coupling: Application to DNA π-stacks. *J. Chem. Phys.*, **117**:5607, (2002).

[52] H. Gommans, D. Cheyns, T. Aernouts, C. Girotto, J. Poortmans, and P. Heremans. Electro-optical study of subphthalocyanine in an bilayer organic solar cell. *Adv. Funct. Mater.*, **17**: 2653–2658, (2007).

[53] A. F. Hebard, R. C. Haddon, R. M. Fleming, , and A. R. Kortan. Deposition and characterization of fullerene films. *Appl. Phys. Lett.*, **59**:2109–2111, (1991).

[54] B. Pevzner, A. F. Hebard, and M. S. Dresselhaus. Role of molecular oxygen and other impurities in the electrical transport and dielectric properties of c_{60} films. *Phys. Rev. B*, **55**:16439, (1997).

[55] G. J. Dutton and S. W. Robey. Exciton dynamics at cupc/c_{60} interfaces: Energy dependence of exciton dissociation. *J. Phys. Chem. C*, **116**:19173–19181, (2012).

[56] R. Pandey, A. A. Gunawan, K. A. Mkhoyan, and R. J. Holmes. Efficient organic photovoltaic cells based on nanocrystalline mixtures of boron subphthalocyanine chloride and c_{60}. *Adv. Funct. Mater.*, **22**:617–624, (2012).

[57] M. Cossi, N. Rega, G. Scalmani, and V. Barone. Energies, structures, and electronic properties of molecules in solution with the C-PCM solvation model. *J. Comput. Chem*, **24**: 669–681, (2003).

[58] A. W. Lange and J. M. Herbert. Polarizable continuum reaction-field solvation models affording smooth potential energy surfaces. *J. Phys. Chem. Lett.*, **1**:556–561, (2010).

[59] A. W. Lange and J. M. Herbert. A smooth, nonsingular, and faithful discretization scheme for polarizable continuum models: The switching/gaussian approach. *J. Chem. Phys.*, **133**: 244111, (2010).

[60] D. M. York and M. Karplus. A smooth solvation potential based on the conductor-like screening model. *J. Phys. Chem. A*, **103**:11060–11079, (1999).

[61] E. Riedle, M. Beutter, S. Lochbrunner, J. Piel, S. Schenkl, S. Spörlein, and W. Zinth. Generation of 10 to 50 fs pulses tunable through all of the visible and the NIR. *Applied Physics B*, **71**:457–465, (2000).

Chapter 4

Concentration dependence of ultrafast carrier dynamics in tetraphenyldibenzoperiflanthene / C_{70} bulk heterojunctions

4.1 Introduction

The Forrest group at the University of Michigan investigates a wide variety of organic photovoltaics. They recently reported a device with high power conversion efficiency, above 8%, using a bulk heterojunction pictured in Figure 4.1, based on tetraphenyldibenzoperiflanthene (DBP) as the electron donor and C_{70} as the electron acceptor [1, 2]. The concentration dependence is surprising; the best devices used a DBP:C_{70} ratio of 1:8 [1] which offered the best balance of open-circuit voltage V_{oc} and short-circuit current J_{sc}.

We investigated the influence of DBP:C_{70} concentration on the charge separation process in these devices, aiming to improve understanding of the device physics. We used several different pump wavelengths in conjunction with the heterodyne-detected TRSHG described in Chapter 2. This pump-frequency-resolved version of TRSHG is the first effective demonstration of a two-dimensional TRSHG method; we demonstrated a two-dimensional TRSHG method earlier this year using Fourier transforms [3], but the measured bandwidth was too small to observe differences across pump wavelengths.

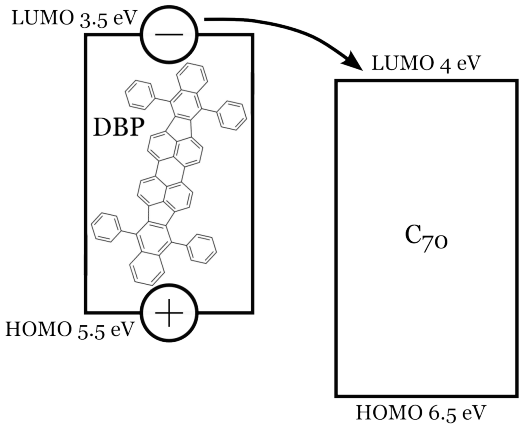

Figure 4.1: Illustration of the DBP / C_{70} charge transfer process. The pump laser primarily excites DBP molecules, creating a Frenkel exciton. The electron is transferred to a nearby C_{70} molecule, creating a Coulombically-bound polaron pair state. Charge separation frees the charge carriers.

Table 4.1: Pump fluence as measured from normal incidence as a function of pump wavelength for the DBP / C_{70} experiment.

PUMP WAVELENGTH (NM)	EXCITATION FLUENCE (μJ/CM^2)
585	0.4
600	0.4
615	0.4
630	0.4
645	0.4
660	0.6
675	0.8
690	1.0
705	1.0
720	1.0

4.2 Methods

A detailed description of the experimental setup was given in Chapters 2 and 3. For these experiments, we used a $\sim$16 mm^2 laser spot area with a $\sim$300 μJ/cm^2 probe fluence, both as measured from normal incidence. The pump light source was a home-built double-pass noncollinear optical parametric amplifier (NOPA) [4]. For this experiment it was tuned to be broadband, covering 575–730 nm. The pump beam next passed through a FASTLITE Dazzler™ acousto-optic programmable dispersive filter, providing dispersion compensation and selecting a 15 nm bandwidth around an arbitrary central wavelength. This provided a tunable-frequency pump pulse. The pump fluence

varied as a function of pump wavelength, maximizing pump power while ensuring the signal still scaled linearly with the pump power. The resulting pump fluences and pump wavelengths are given in Table 4.1. While the pump fluences were much lower than that used in Chapter 3, they were comparable to that used in [5] which was a similar experimental study investigating charge movements in a bulk heterojunction device. The time resolution of this experiment was $<$100 fs, close to the Fourier limit, as measured by a second-order cross-correlation frequency resolved optical gating (XFROG) between the pump and probe in a 10 μm thick β-barium borate (BBO) crystal placed at the sample position. Each data point was averaged for three seconds, before changing the pump wavelength and/or time-delay. The time-points were spaced hyperbolically (following a hyperbolic sine function) so more points were close to time-zero than far from time-zero. Samples were manufactured by Xiao Liu of the Forrest group, with DBP:C_{70} ratios of 1:1, 1:2, 1:3, 1:4, and 1:8. These had ITO and aluminum electrodes, MoO_3 and bathophenanthroline (BPhen) buffer layers, and 54 nm of active layer. There were also control samples, including a neat DBP sample, a neat C_{70} sample, and a sample with no active layer; these control samples had electrodes and buffer layers.

4.2.1 Background signals

Since these films have several interfaces between dissimilar materials, each interface may contribute a background second-order nonlinear susceptibility $\chi^{(2)}$ due to the lack of inversion symmetry at the interface [6]. This would make the SHG not strictly proportional to the EFISH. A model for this background signal is

$$E_{\text{SHG}} \propto \left[\chi^{(2)}_{\text{background}} + \chi^{(3)}_{\text{EFISH}} E_{\text{DC}}\right] E^2_{\text{probe}}. \tag{4.1}$$

It is possible to use heterodyne detection to separate the background from the signal, since both the real and imaginary parts of E_{SHG} are measured. This is therefore an additional advantage of heterodyne detection over traditional detection. It is simple to measure $\chi^{(2)}_{\text{background}}$ by measuring

E_{SHG} as a function of applied external bias V, with the pump beam blocked; it should be a (complex) straight line as a function of $E_{\text{DC}} = V/\mathcal{T} + E_{\text{intrinsic}}$ where $\mathcal{T}$ is the active-layer film thickness and $E_{\text{intrinsic}}$ is the intrinsic electric field. Future measurements will adopt this approach; here we measure and subtract the background contribution using a method described below.

Chapter 2 details computing a TRSHG signal S that is proportional to the effective nonlinear susceptibility $\chi^{(2)}_{\text{eff}} = \chi^{(2)}_{\text{background}} + \chi^{(3)}_{\text{EFISH}} E_{\text{DC}}$. However, the constant of proportionality may vary sample to sample, making comparisons between $\chi^{(2)}_{\text{eff}}$ across samples more difficult. The solution is to define a slightly different signal $\mathcal{S}$ that preserves the constant of proportionality. It was observed in Chapter 2 that the effective nonlinear susceptibility may be written in terms of the spectral interferometry functions $I_0(\omega)$ and $I_1(\omega)$, together with a (complex) constant of proportionality A and a phase function $\phi(\omega)$:

$$\chi^{(2)}_{\text{eff}} = A \frac{I_1(\omega) \exp(i\phi(\omega))}{I_0(\omega)}. \tag{4.2}$$

A problem is that the measured signal S of Chapter 2 may have a different A and ϕ for different samples. However, since $I_0(\omega) = |E_{\text{LO}}|^2 = |A|^2 |E_{\text{probe}}|^4$ and since $I_1(\omega) = E^*_{\text{LO}} E_{\text{SHG}} \exp(-i\phi(\omega)) = A^* \chi^{(2)}_{\text{eff}} |E_{\text{probe}}|^4 \exp(-i\phi(\omega))$ we can define a new measured signal $\mathcal{S}$ proportional to $\chi^{(2)}$ that does not depend on $|A|$:

$$\begin{aligned} \mathcal{S} &\equiv \frac{I_1(\omega)}{\sqrt{I_0(\omega)}} \\ &= S\sqrt{I_0(\omega)} \\ &= \frac{A^*}{|A|} \chi^{(2)}_{\text{eff}} |E_{\text{probe}}|^2 \exp(-i\phi(\omega)). \end{aligned} \tag{4.3}$$

Here, the same $\phi(\omega)$ must be used across samples to make $\mathcal{S}$ proportional to $\chi^{(2)}_{\text{eff}}$ across samples. In order to help compensate for laser noise, I compute $\mathcal{S} = S \cdot \overline{\sqrt{I_0(\omega)}}$ where the over-line indicates taking the mean. Since A should be time-invariant, this is a better way to compute $\mathcal{S}$ as long as the long-term laser noise in the probe pulse is small.

We observed that $\mathcal{S}$ does not depend on $|A|$ but it still depends on the phase of A (the data are not *phased*). Therefore phase differences in $\mathcal{S}$ between samples are not meaningful, al-

though amplitude differences between samples are meaningful. Using a data-trace $\mathcal{S}(t)$ as a function of the pump-probe time delay t, all of the data should lie on a line in the complex plane. This will define the complex direction $\hat{n}_{\text{EFISH}}$ of $\chi^{(3)}_{\text{EFISH}}$ for the current data-trace. Then $\mathcal{S} = \mathcal{S}_{\text{background}} + C\hat{n}_{\text{EFISH}}E_{\text{DC}}$ defines $\mathcal{S}_{\text{background}}$ up to the real constant of proportionality C. Using multiple data-traces, taken with different internal fields E_{DC} on the same sample, the constant C and the background $\mathcal{S}_{\text{background}}$ can be determined using a least-squares framework. The least-squares model is this:

$$\mathcal{S}_j(t<0)\exp(i\varphi_j) = \mathcal{S}_{\text{background}} + CE_{j,\,\text{DC}}(t<0). \tag{4.4}$$

Here, $\mathcal{S}_j(t<0)$ is the measured complex SHG signal of data-trace j in the absence of the pump. φ_j is a measured phase for trace j that makes the EFISH signal real—it comes from $\hat{n}_{j,\,\text{EFISH}}$ which comes from the dynamics of $\mathcal{S}_j(t>0)$. Meanwhile, $E_{j,\,\text{DC}}(t<0)$ is the known internal electric field in the absence of the pump, controlled by the external voltage V_j. As before, this is $E_{j,\,\text{DC}} = V_j/\mathcal{T} + E_{\text{intrinsic}}$ where $\mathcal{T}$ is the film thickness and $E_{\text{intrinsic}}$ is the built-in electric field. The unknowns are the complex background $\mathcal{S}_{\text{background}}$ and the real coefficient C. So long as two or more traces j with different external voltages V_j are used, the background can be fit. Then the measured internal field can be directly computed:

$$E_{j,\,\text{DC}}(t) = \frac{1}{C}\text{Re}\left\{\mathcal{S}_j(t)\exp(i\varphi_j) - \mathcal{S}_{\text{background}}\right\}. \tag{4.5}$$

4.3 Results

We measured TRSHG time traces on the neat films (the control samples), but they showed no appreciable dynamics over the timescales we measured, as shown in Figure 4.2. This is expected, because very little charge transfer and separation should occur in these films. The small amount of signal we saw in the neat DBP sample is probably due to charge transfer from the DBP to the BPhen buffer layer. The 1:1 mixed sample also showed very little dynamics, as shown in Figure

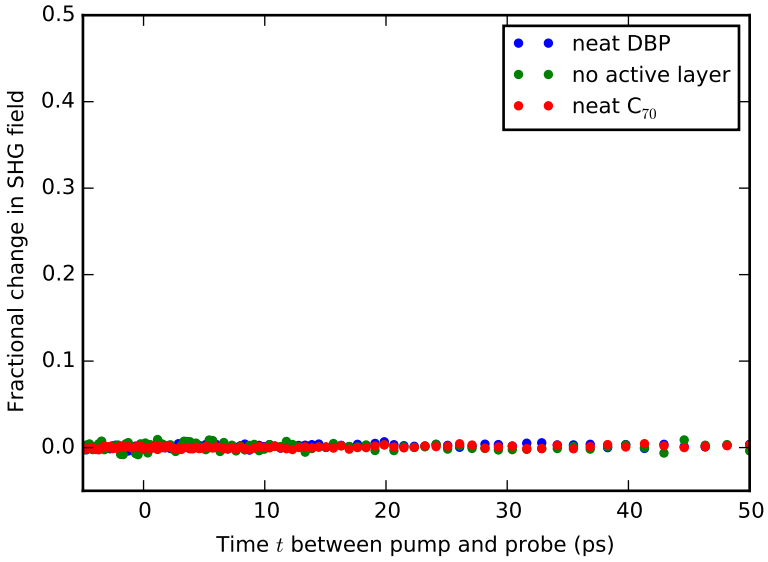

Figure 4.2: TRSHG results on neat DBP and C_{70} samples, and a no-active-layer sample. No appreciable dynamics are observed. The plotted data used a pump wavelength of 600 nm and an applied voltage of 0 V (short-circuit conditions); other pump wavelengths similarly did not show any dynamics.

4.3. Some dynamics are visible, but they are surprisingly slow for the applied voltage of -2 V (see Figure 4.4). The four remaining samples, the 1:2, 1:3, 1:4, and 1:8 mixtures, all showed qualitatively similar dynamics, in that a strong signal with a relatively simple temporal shape is immediately evident after time zero. Several representative examples are given in Figure 4.4.

The TRSHG data on the mixed films were converted to measurements of electric field $E_{\text{DC}}(t)$ in the active layer, using Equation 4.5. We used an active-layer film thickness of $\mathcal{T}$=54 nm and a built-in electric field $E_{\text{intrinsic}} = (0.9\,\text{V})/\mathcal{T}$ coming from the open-circuit voltage of these devices [1, 2]. We considered exponential and stretched exponential kinetic models, together with a simplified power law with a fixed exponent of -1; the mean error of these models is shown in Figure 4.5. A double exponential model (not shown) did fit well, but needed more free parameters and the data did not effectively constrain those parameters. For the most part, the best model was a simple power law with a fixed exponent of -1, achieving a good representation of the dynamics with only three free parameters A, B, and k (the same number of free parameters as a single exponential

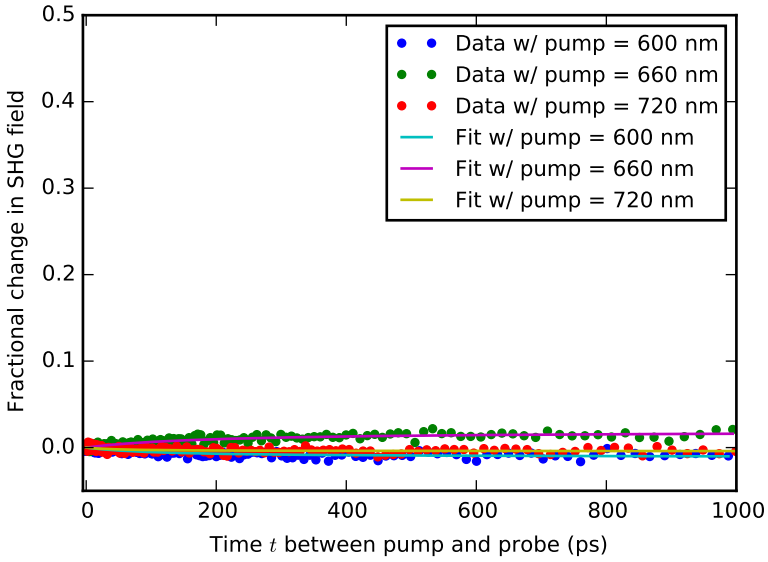

Figure 4.3: TRSHG results on a DBP:C_{70} ratio of 1:1. Only small and relatively slow dynamics are observed, despite the large applied voltage of -2 V. Compare with the much larger and faster dynamics recorded in Figure 4.4.

model):

$$E_{\text{DC}}(t) = A - H(t)B\left(1 - \frac{1}{1+kt}\right). \tag{4.6}$$

Here, $E_{\text{DC}}(t)$ is the electric field in the active layer as a function of time (given by Equation 4.5), $H(t)$ is the Heaviside step function, A is the electric field before photoexcitation, B is the late-time change in E_{DC} induced by the pump, and k is a rate constant with units of inverse time. This power law may be interpreted as an exponential distribution of exponential rates with mean k; under this interpretation the probability density function $\rho(\kappa)$ for a particular molecule to have a rate κ would be $\rho(\kappa) = \exp(-\kappa/k)/k$.

For the data with the -2 V external bias, we additionally included a slow (linear) component in the model:

$$E_{\text{DC}}(t) = A + H(t)\left[-B\left(1 - \frac{1}{1+kt}\right) + Dt\right], \tag{4.7}$$

where D is the amplitude of the slow component. There are several processes that could explain its presence; for example, hole transport in DBP is expected to be much slower than electron transport in C_{70}. Alternatively, the linear component may reflect the steady-state charge carrier mobility. We

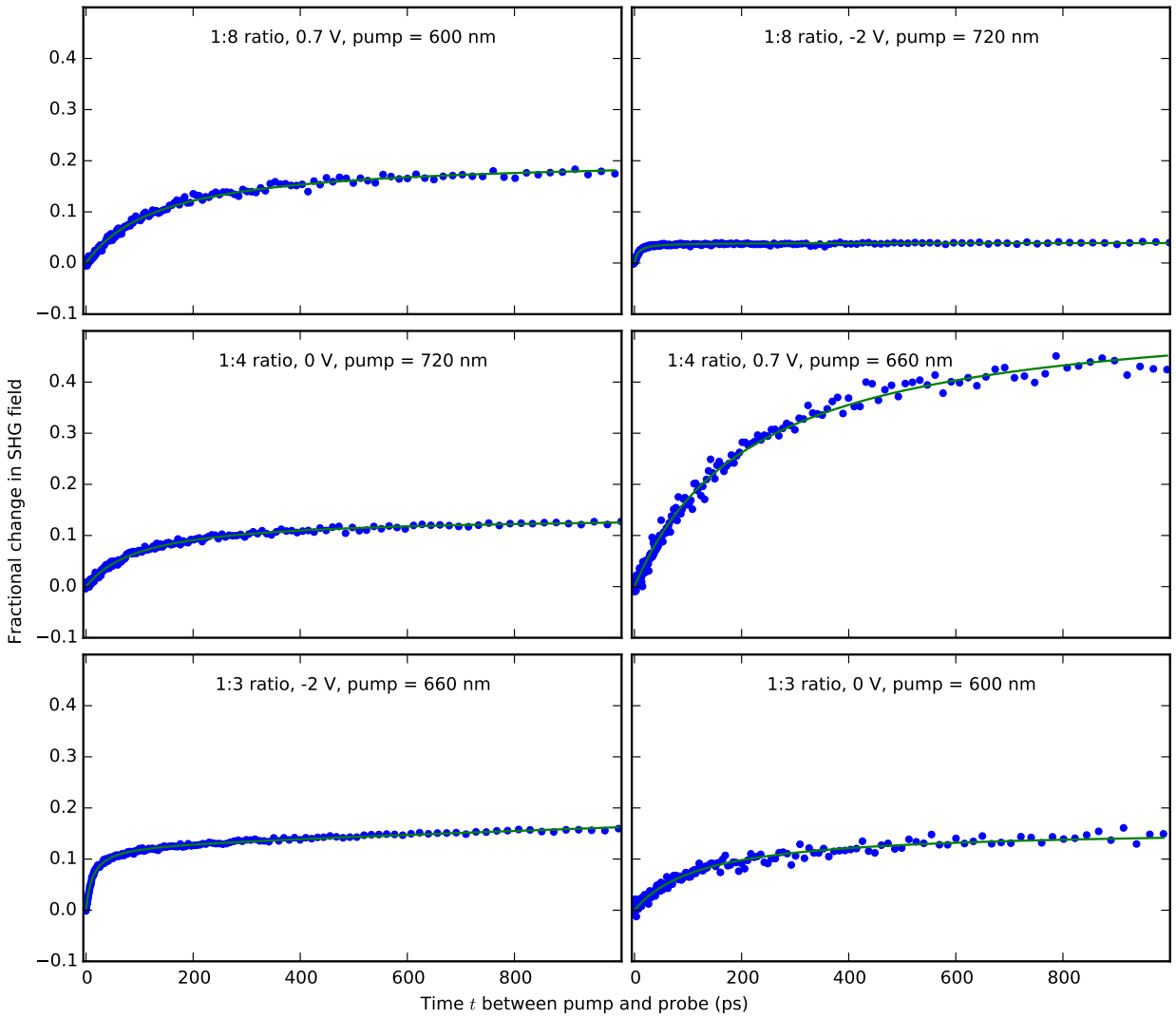

Figure 4.4: Representative TRSHG results on DBP:C_{70} ratios of 1:3, 1:4, and 1:8. Dots, measured data. Solid lines, fits. Some general trends are observable here: the rate(s) associated with -2 V are faster than those of 0 V, which are faster than those of 0.7 V. Fractional changes for -2 V are small because the electric field is high, and vice versa for 0.7 V.

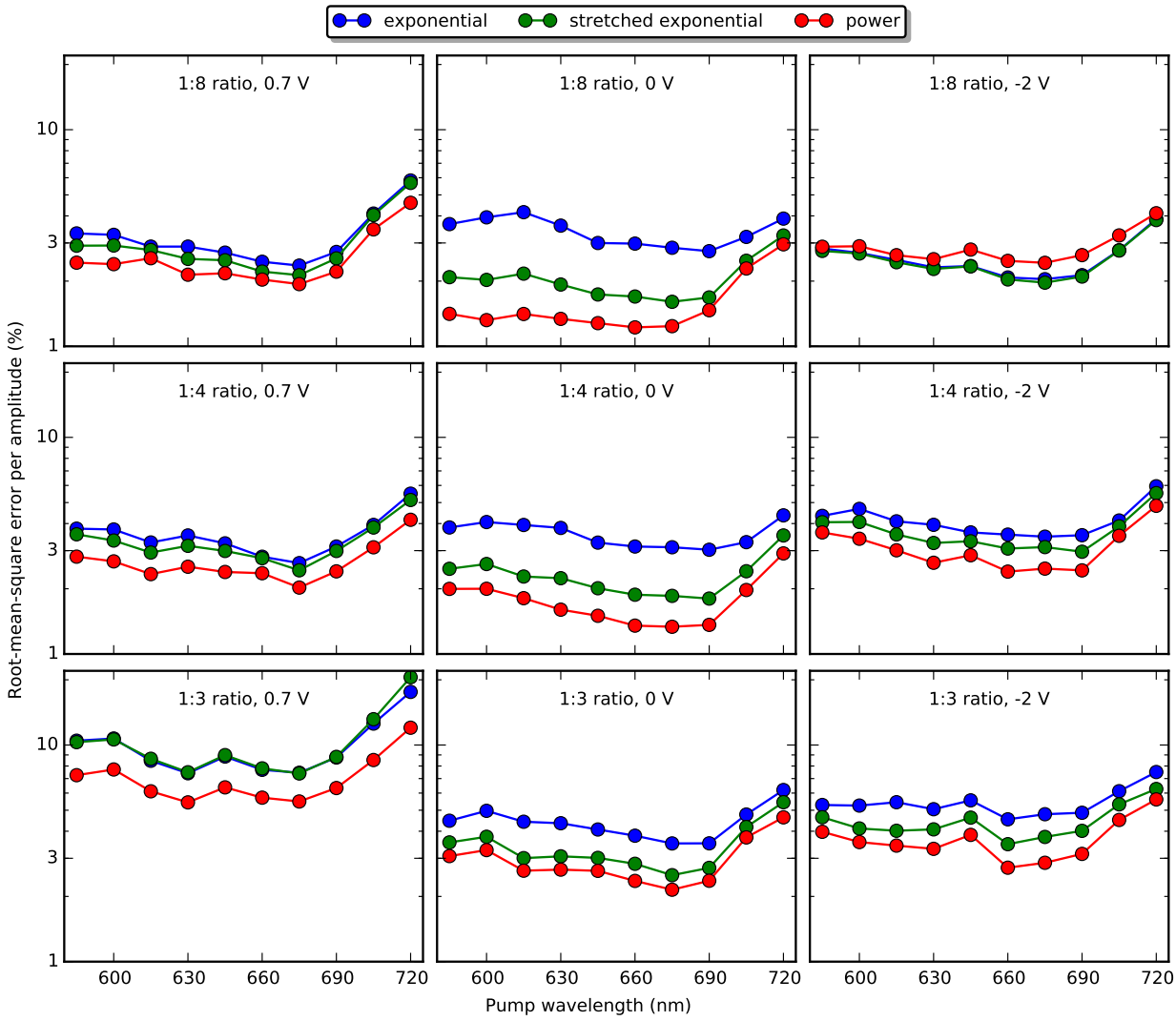

Figure 4.5: Root mean square error for different fitting models, expressed as a percentage of the amplitude of the signal. Each column of subfigures contains a single voltage, while each row contains a single mixture. Three types of models are pictured: the blue curves contain a single exponential model with three parameters. The green curves are a stretched exponential model with four parameters. The red curves are the power-law model defined in 4.6 with three parameters. All -2 V data included an additional linear term akin to Equation 4.7, requiring one extra fitting parameter. All models perform fairly well, with fitted errors typically on a several-percent level, but in most cases the power-law model is the best. However, the exponential model does perform slightly better for the 1:8 mixture at -2 V. The error increases for red pumping wavelengths due decreased pump absorption decreasing the amplitude of the signal.

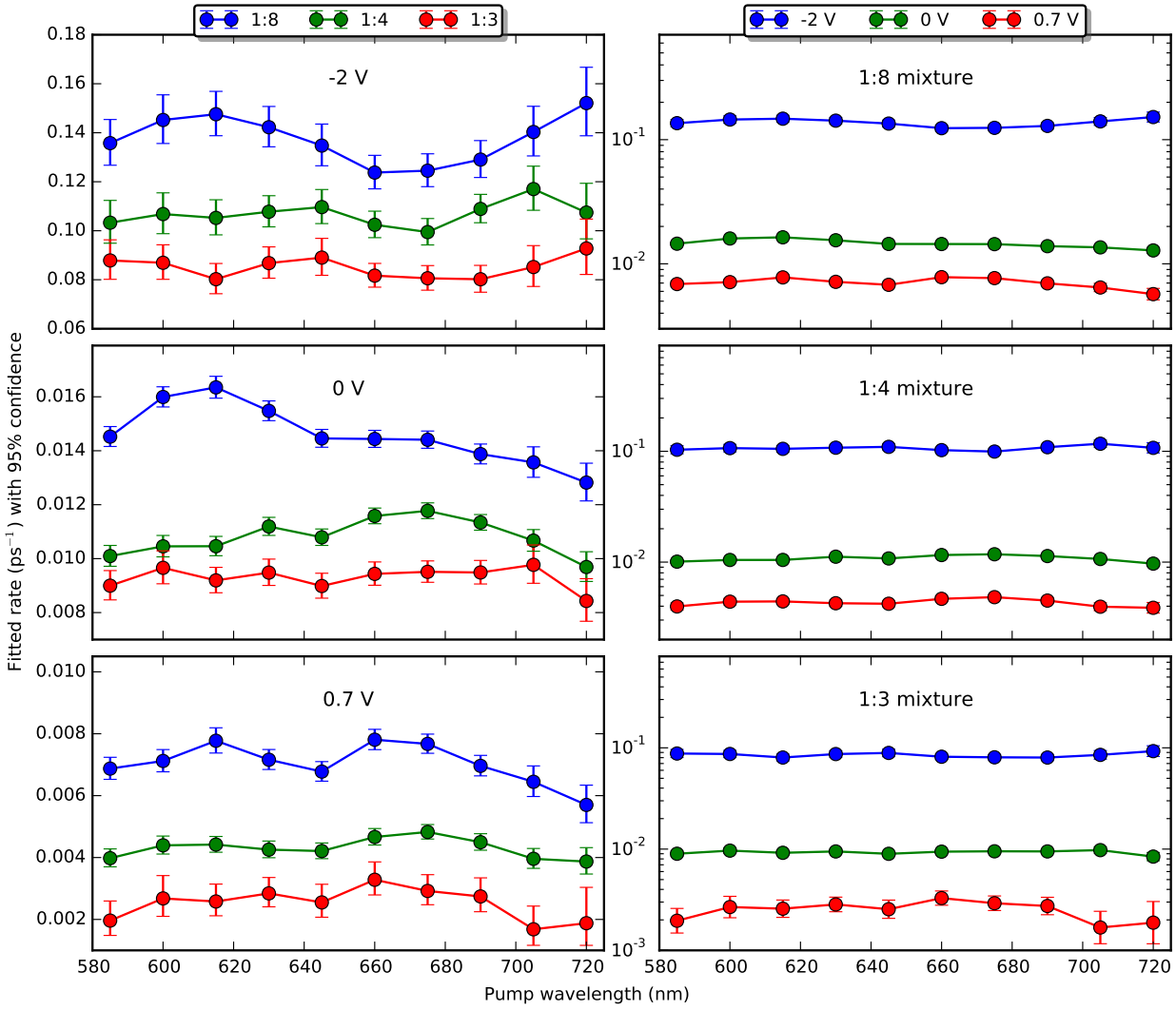

Figure 4.6: Fitted rates as a function of sample concentration and applied voltage. Rates k are defined in Equation 4.6. Error bars are 95% confidence intervals. Left subfigures compare across samples at fixed external voltage (legend at the top). Right subfigures provide comparisons between voltages for each sample (legend at the top).

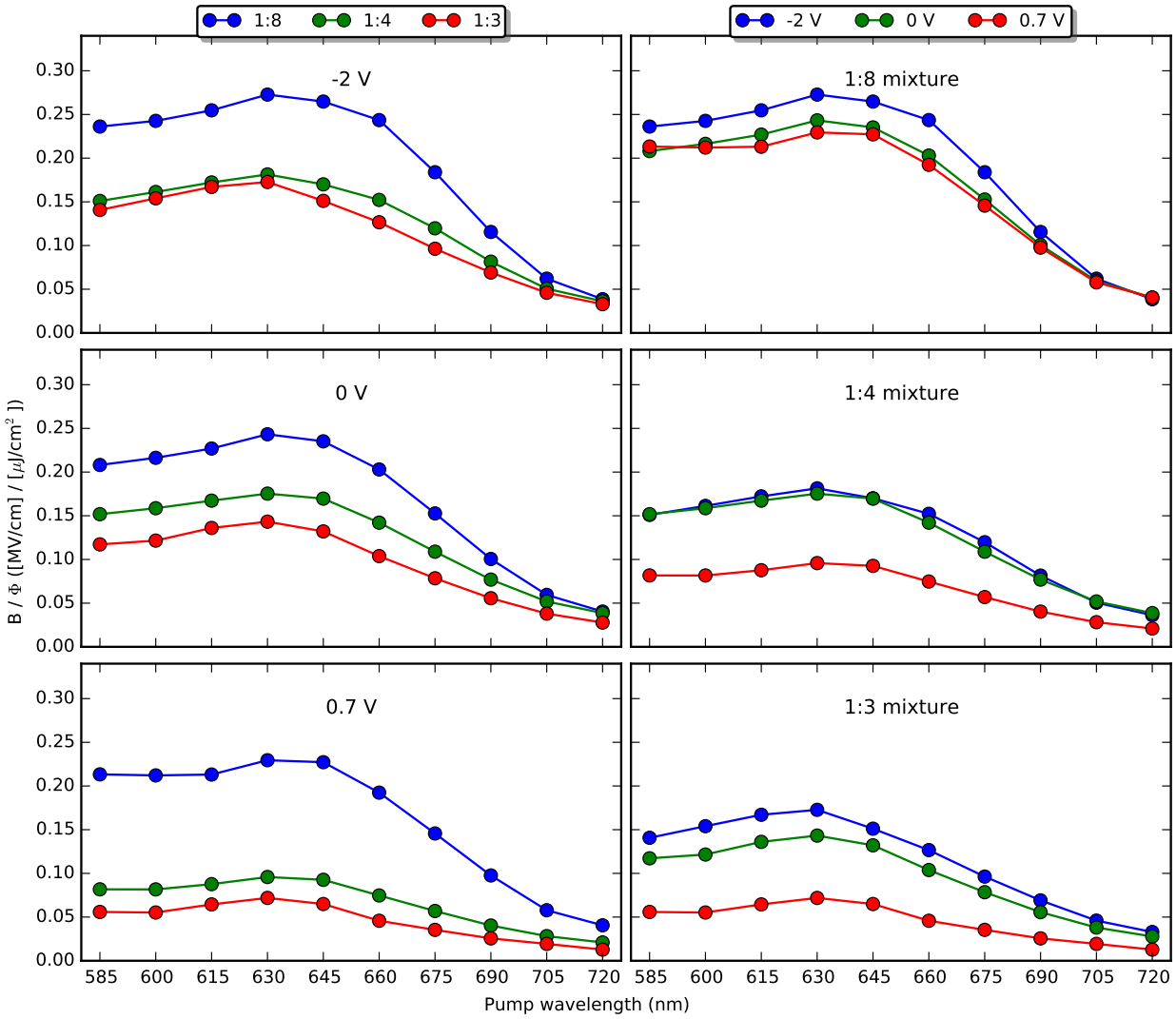

Figure 4.7: Fitted amplitudes as a function of sample concentration and applied voltage. The change in internal electric field B is plotted (defined in Equation 4.6), per unit pump fluence Φ (given in Table 4.1). This B/Φ is expected to be proportional to the separation ℓ between electron and hole after the initial charge separation event, times the absorption spectrum. Left subfigures compare across samples at fixed external voltage (legend at the top). Right subfigures provide comparisons between voltages for each sample (legend at the top).

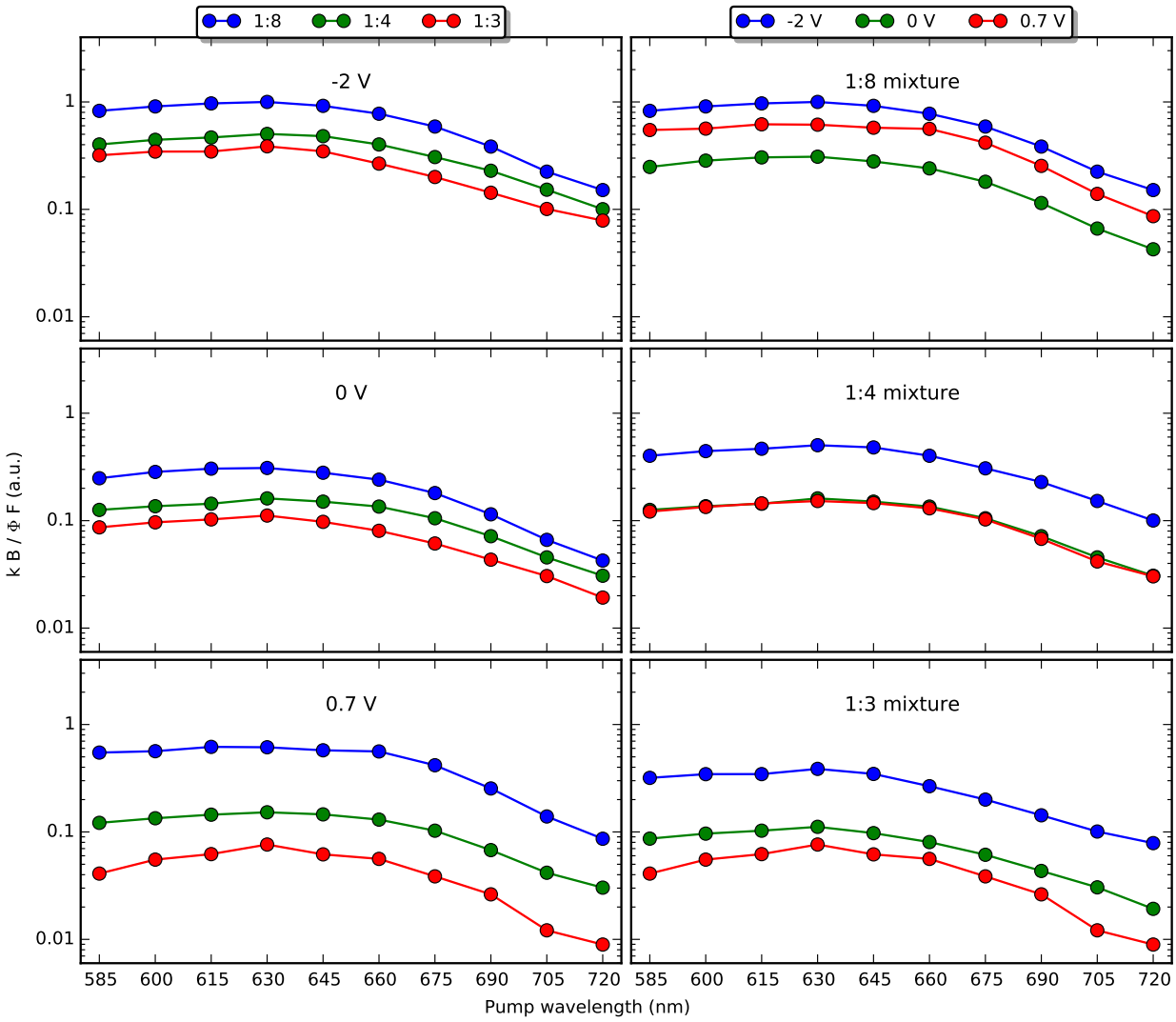

Figure 4.8: Trends for mobility as a function of sample concentration and applied voltage, for the initial charge separation event. $kB/\Phi F$ is expected to be proportional to the effective mobility for the initial charge separation event, times the absorption spectrum. k and B are defined in Equation 4.6. Pump fluence Φ is given in Table 4.1. I used $F = (0.9\,\mathrm{V} - \mathcal{V})/\mathcal{T}$ as the internal field, where $0.9\,\mathrm{V}$ is the open-circuit voltage [1, 2], $\mathcal{V}$ is the applied bias voltage, and $\mathcal{T}$=54 nm is the active-layer film thickness. Left subfigures compare across samples at fixed external voltage (legend at the top). Right subfigures provide comparisons between voltages for each sample (legend at the top).

only observe the slow component in the -2 V external bias case; this is likely because charge transport becomes much faster with such a strong internal field. We expect that if we scanned to sufficiently long pump-probe delays t that the 0 V and 0.7 V data would also show the slow component.

These power-law models were fitted to the data for the 1:3, 1:4, and 1:8 mixtures, using the `leastsq` Levenberg-Marquart least-squares fitting algorithm in the open-source `scipy.optimize` package [7]. The fitted rate constants k as a function of pump wavelength, applied voltage, and sample are plotted in Figure 4.6. Using the estimated covariance matrix, 95% confidence intervals for the rates were obtained. Meanwhile, the fitted amplitudes per unit pump fluence B/Φ are plotted in Figure 4.7, where Φ is the pump fluence. While not plotted, the data for the 1:2 mixture look qualitatively similar and show similar trends.

A power-law model is not expected to work for very long times, on the scales of nanoseconds to milliseconds. The instantaneous mobility—proportional to the derivative of the model—should eventually converge to the steady-state mobility. As mentioned above, we saw the first hints of longer-term components to the kinetics with the -2 V data, where some slow process was visible, which may even represent the steady-state mobility.

4.4 Discussion

Our prefactual expectation was that the SHG would always decrease after photoexcitation, following the EFISH explicitly [5]. This was observed to be true, except in the case where we applied a positive external bias of 0.7 V to the 1:3 ratio sample. This was strong evidence for the background SHG signal as described in Section 4.2.1 that does not come from EFISH. If the phase of $\chi^{(2)}_{\text{background}}$ is more than $\pi/2$ away from the phase of $\chi^{(3)}_{\text{EFISH}}$ then the total amount of $|E_{\text{SHG}}|^2$ may increase as E_{DC} decreases, for cases where $\chi^{(3)}E_{\text{DC}}$ is small, as in cases of small internal fields enabled by positive external bias voltages. Amarasinghe Vithanage et al. did not observe this phenomenon [5], but that may be because they did not use positive external bias voltages.

The data suggest that there is a discrete phenomenon of initial charge separation, where the electron and hole separate by several nanometers, after which the separation process slows dramatically. The initial charge separation occurs over a time period of $1/k$ = 7–500 ps, depending on applied voltage and mixture. After subtracting the background to yield measured fields, the change in field $B = \Delta E_{\text{DC}}(t)$ is proportional to the average distance $\ell(t)$ the carriers have traveled along that field:

$$\Delta E_{\text{DC}} = \frac{ne\ell(t)}{\epsilon\epsilon_0}, \tag{4.8}$$

where n is the number density of carriers, e is the fundamental charge, ϵ is the relative permittivity of the active layer, and ϵ_0 is the permittivity of free space [5]. The number density n is proportional to the number of absorbed photons. Therefore the amplitudes per pump fluence B/Φ are proportional to the final displacement ℓ times the absorption spectrum. These displacements may be estimated to be on the order of several nanometers, based on reasonable assumptions. For example, in Figure 4.7 we see $B/\Phi \sim 0.25\,\text{MV cm}^{-1}\,\mu\text{J}^{-1}\,\text{cm}^2$ for a pump wavelength of 630 nm in the 1:8 sample, nearly independent of applied bias. Meanwhile, $n/\Phi \approx (630\,\text{nm})/hc\mathcal{T}$ for near-total pump absorption, where h is Planck's constant and c is the speed of light in vacuum. Taking $\epsilon \sim 3$ for these films, and taking into account the 45-degree angle of incidence for the pump, the approximate final ℓ will be ∼10 nm. The other samples will have a smaller final ℓ, in the range of ∼2–7 nm.

We may interpret this ultrafast charge separation event in terms of an effective mobility. Since B/Φ is proportional to displacement ℓ, multiplying it by the rate k is proportional to the carrier velocity: $v \propto kB/\Phi$. Dividing this velocity by the field strength F gives an effective mobility for the initial charge separation process $\mu \propto kB/\Phi F$, where F is the field inside the sample. These are plotted in Figure 4.8; it should be remembered that $kB/\Phi F$ is also proportional to the light absorption.

4.4.1 Trends in the 1:3, 1:4, and 1:8 mixtures

There are several trends that can be observed in the data shown in Figures 4.6, 4.7, and 4.8. First, larger internal electric fields $E_{\mathrm{DC}}(t < 0)$ (more-negative voltages) make for larger changes in field B. Since carrier densities n are likely independent of internal field, this means that larger fields cause the carriers to travel farther during the initial charge separation (larger ℓ). For some samples and voltages, this effect is small. For example, the 1:4 sample shows nearly-identical amplitudes for -2 V and 0 V, although it does decrease for 0.7 V. Also, all three voltages on the 1:8 sample show similar amplitudes even though the same trend is apparent. On the other hand, larger fields $E_{\mathrm{DC}}(t < 0)$ correspond to much larger rates k, by more than an order of magnitude. So larger fields make the carriers travel a little farther, but they get there much faster. This makes the effective mobility of the initial charge separation event generally increase for more-negative voltages, as seen in Figure 4.8.

Second, larger amounts of C_{70} in the ratio between DBP and C_{70} also make for a significantly larger amplitude B, and a significantly faster rate k. Therefore larger amounts of C_{70} cause carriers to travel further before stopping, and they do so in less time. The effective carrier mobility is much larger with increasing C_{70}—especially for the 0.7 V bias which is close to the maximum power point [1]. It is probable that this further, faster separation decreases polaron pair recombination in the 1:8 sample.

Third, the fitted rates k depend on pump wavelength, although the effect is not large. The effect is most interesting on the red edge of the spectrum, where the rates trend downwards for 0 V and 0.7 V but they trend upwards for -2 V. This may be due to the nature of the absorptions on that edge. Neither C_{70} nor DBP absorb appreciably around 700 nm by themselves, but the mixture absorbs quite a bit more, as seen in Figure 4.9 and Ref. [1]. Clearly, mixing the two materials creates new optical transitions to newly-accessible states. It seems logical that those states would have direct charge-transfer character, due to the donor-acceptor nature of C_{70} and DBP. For example, linking donor and acceptor subunits together in the same conjugated polymer enables new, lower-energy transitions with charge-transfer properties [8]. Also, our collaborators

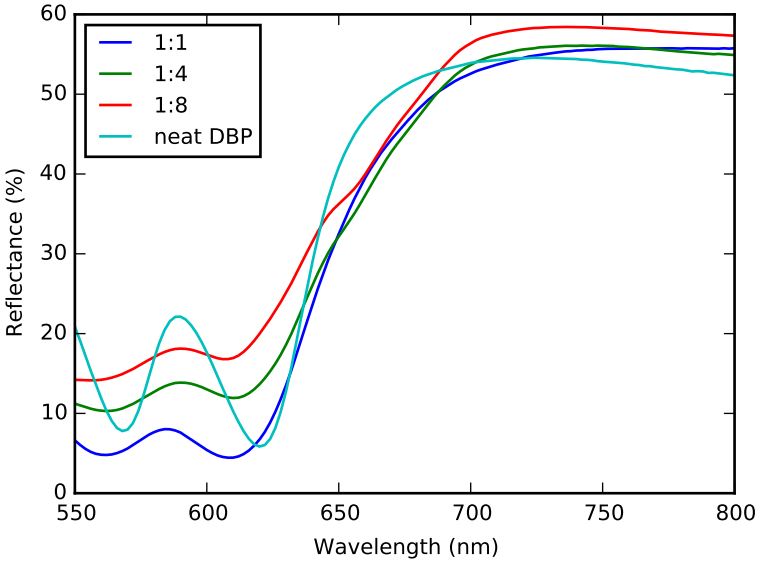

Figure 4.9: Measured reflectance of several devices, measured by Xiao Liu. Shown are reflectance for the 1:1, 1:4, and 1:8 mixtures; the neat-DBP control sample is also shown for comparison.

predict at least some configurations of boron subphthalocynanine chloride (SubPc) next to C_{60} can produce optically bright charge transfer states [9] with lower energy than molecules' original absorptions. If the 700 nm absorptions in DBP / C_{70} are indeed charge-transfer states, then they are in essence directly-excited polaron pair states. The separation rate k may trend downwards for small internal fields, since the polaron pair is a *cold* polaron pair having no extra vibrational energy. By contrast, bluer pumping wavelengths would yield a *hot* polaron pair; the energy in the Frenkel exciton is significantly more than the energy in the polaron pair state, and the extra energy would likely go into local vibrational modes. The increased effective localized temperature may promote charge separation when the internal fields are not very large. On the other hand, at large internal fields such as the -2 V external bias, the separation rate k may trend upwards due to a combination of the large field overcoming the effect of hot versus cold polaron pairs, together with the fact that direct optical excitation of polaron pairs means it is not necessary to convert the Frenkel exciton to a polaron pair.

Fourth, much of the pump wavelength dependence in the $kB/\Phi F$ plot (Figure 4.8) is likely due to the frequency dependence of the absorption, as illustrated by the films' reflectance shown in Figure 4.9. However, the 0.7 V data on the 1:8 film shows nearly the same $kB/\Phi F$ for 645 nm

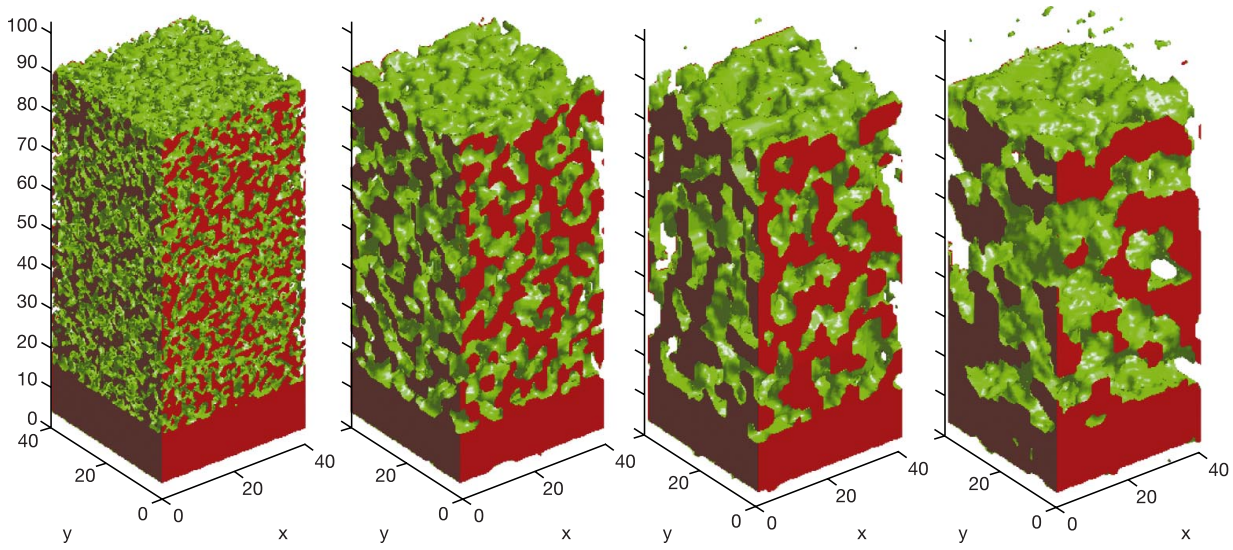

Figure 4.10: Depiction of phase separation in organic photovoltaic films, reproduced from [10]. Simulation of progressive phase-separation upon annealing using a 1:1 mixture of copper phthalocyanine (CuPc) and 3,4,9,10-perylene tetracarboxylic bis-benzimidazole (PTCBI). CuPc is shown in red while PTCBI is transparent; the interface between CuPc and PTCBI is shown in green. The simulation shows clear interpenetrating percolating networks of CuPC and PTCBI. Left, no annealing; left-center, annealed for 15 min at 450 K; right-center, annealed for 15 min at 500 K; right, annealed for 15 min at 550 K. Progressively larger domain sizes are visible with higher annealing temperatures.

and 660 nm pump wavelengths, despite having significantly different absorption. This indicates that the 660 nm pump wavelength gives a significantly higher effective mobility than the 645 nm wavelength.

4.4.2 The initial charge separation event

It is very interesting that the initial charge separation mobility is so much faster than the steady-state mobility. This observation may be related to the morphology: efficient bulk heterojunctions typically phase separate into two interpenetrating *percolating* networks of electron donor and electron acceptor phases [11]. This structure ensures a small physical distance between donor and acceptor materials throughout the device, enhancing Frenkel excition to polaron pair conversion. The structure also allows holes to travel efficiently through the donor and electrons to travel efficiently through the acceptor, suppressing geminate recombination at the same time. This phase

separation is qualitatively depicted in Figure 4.10. While the figure shows phase separation as a function of annealing temperature, it is expected that some phase separation would be visible even without any annealing, due to the kinetic energy imparted by the vacuum thermal deposition process, and even due to molecular motions at room temperature.

In the particular case of a bulk DBP:C_{70} heterojunction, Xiao Liu in the Forrest group reports that C_{70} forms small crystallites, based on electron diffraction data. Larger fractions of C_{70} in the mixture result in larger crystallites. Due to the very small amounts of DBP in these devices, the DBP must fill up small gaps between C_{70} crystallites. With these constraints in mind, I would expect the C_{70} crystallites to form a variety of mostly-convex shapes that adjoin each other into a percolating network, and I would expect the amorphous DBP domains to be threadlike percolating networks reminiscent of a *reticulated foam*. For large amounts of DBP, I would expect the amorphous DBP domains to wrap around the C_{70} crystallites such that the C_{70} network doesn't percolate, harming electron mobility and increasing geminate recombination. For very small amounts of DBP, the threads of DBP might cease to percolate, harming the hole mobility and increasing geminate recombination.

There are a large number of possible explanations for the initial charge separation phenomenon, some of which deal with morphology and some more general. Some of them have been eliminated outright, while others need further investigation. In general, the picture is this: the electron and hole separate by several nanometers measured along the electric field line during the first 10–500 ps, depending on applied voltage and DBP:C_{70} ratio, after which they stop, at least on the time-scale of around a nanosecond. The rate is much faster for larger fields, and somewhat faster for larger C_{70} concentrations. The distance traveled and even the effective mobilities are also somewhat increased for larger fields and larger C_{70} concentrations.

- The observed carrier stopping is not attributable to charges piling up edges of the active layer, canceling the electric field. We only observe small changes in electric field, not a complete cancellation of the field.

- The stopping is not attributable to a charge transfer picture where polaron pairs are created

but no further changes happen on the timescale of a nanosecond. Charge-transfer states keep the electron and hole close together; to cause the kinds of field dynamics we observe, either the electron and hole need to be several nanometers apart—unrealistic for a polaron pair—or the polaron pair number density needs to be much higher than our pump photon fluence would allow.

- The dynamics cannot be solely due to charge transfer states tunneling directly to long-range charge separated states, escaping the Coulombic binding energy. Movements of free carriers are necessarily faster than movements of bound carriers; the process of tunneling out of the Coulombic binding energy would then make the carriers move faster afterwards, not come to a stop.

- Excitons in organic photovoltaics have some characteristic delocalization over several molecules; it has been observed that this increased exciton size can enhance dissociation efficiency [10]. However, it seems unlikely that this delocalization could lead to the charges stopping after a nanosecond.

- It is conceivable that the percolating-network structure of these films could lead to large initial mobility followed by greatly-reduced mobility. In this picture, electrons move until they hit a 'dead end', after which they must thermally move around until they can escape. The extreme case here is the 1:1 film, where perhaps the C_{70} network does not percolate and so almost no dynamics occur. In support of this idea, the 1:3, 1:4, and 1:8 films exhibit faster rates for larger fields, and larger amounts of C_{70} do allow for more charge movement. However, larger amounts of C_{70} also allow for a faster rate, which is inconsistent with this picture unless the electron mobility is much higher in these films. Also, larger amounts of C_{70} only have a little more charge movement before stopping; larger amounts of C_{70} in a percolating-network picture should drastically reduce the number of dead ends, enabling much more charge movement.

- Charge traps may explain the dynamics. These traps would likely come from defects in the

crystalline structure of C_{70}; crystallite boundaries and interfaces with DBP are obvious sites for defects. Larger amounts of C_{70} might therefore be expected to decrease the carrier trap density, promoting increased travel distance. This would enhance the electron mobility and therefore could also explain the increased rate k with larger amounts of C_{70}.

- The sizes of the C_{70} crystallites may also be a key explanatory factor. Larger amounts of C_{70} should increase the crystallite size somewhat. This would explain the increased separation ℓ. Perhaps the crystallinity would also be improved, which could enhance the electron mobility and therefore the rate k. Larger crystallites have a decreased surface area-to-volume ratio, decreasing the density of surface states which may be traps. This is a second mechanism by which larger crystallites may lead to improved electron mobility.

- It is common for mobilities to increase with larger internal fields in disordered organic semiconductors [12–16]. The mobility dependence on the electric field appears somewhat lessened in the 1:4 and 1:8 samples compared to the 1:3 sample, suggesting the C_{70} disorder may indeed decrease with larger C_{70} concentrations (enhanced crystallinity and/or decreased amount of crystallite surface).

4.4.3 The 1:1 mixture

By contrast, the 1:1 sample shows almost no kinetics as a function of time, as shown in Figure 4.3. This implies the effective charge mobility in the 1:1 mixture is much lower than the other mixtures. The total mobility is likely dominated by electrons since the C_{70} crystallites should have a high electron mobility. It is tempting to attribute this to my prediction earlier—that too much DBP allows it to wrap around the C_{70} crystallites, preventing percolation in the network of C_{70}. However, the most promising explanation above for the rest of our data is that dynamics are only observed within a single crystallite, and so this theory would still predict rapid initial kinetics for the 1:1 sample. On the other hand, we also suggested that decrease C_{70} in the mixture may inhibit C_{70} electron mobility, by decreasing the crystallinity and/or decreasing the density

of surface states. The electron mobility is therefore expected to be particularly poor for the 1:1 sample, which is consistent with our data.

4.4.4 The meaning of the power-law model

It is also interesting that our best fitting model was a simplified power law of the form $1/(1+kt)$. A good question is, what is the origin of such behavior? As mentioned above, it could come from an exponential distribution of individual rates, but what phenomena would lead to such a distribution? As mentioned above, the sizes of the C_{70} crystallites could be key. A broad distribution of sizes of the C_{70} crystallites could lead to the $1/(1 + kt)$ form of the kinetics.

We did see differences in form for the 1:8 sample at high field (-2 V)—that data trace looked slightly more exponential in character as seen in Figure 4.5. However, the fitted rate for that case was very high, around 0.14 ps^{-1}, and so relatively few of our data-points contributed to the observed kinetics, making determination of the best model more difficult. In addition, including a linear component to the model may have biased our fitting towards preferring the exponential model.

4.5 Conclusions

To summarize, using TRSHG spectroscopy we measured ultrafast charge separation in DBP:C_{70} bulk heterojunction devices as a function of the ratio between DBP and C_{70}. We used several different pump wavelengths, spanning 585 to 720 nm, resolving both the excitation frequency and the time dependence of the charge separation. We came to several interesting conclusions. In particular, it appears that photoexcitation is followed by a relatively fast initial charge separation event where the electron and hole separate by several nanometers, measured along the direction of the external electric field. After the initial charge separation, they separate much more slowly. Our best explanation for this effect is that the electrons are quite mobile within the C_{70} crystallites but take some time to hop from crystallite to crystallite. Surprisingly, the kinetics of this initial

separation followed a $1/(1+kt)$ simplified power law, suggesting a broad size distribution of the crystallites. This crystallite-based explanation of our data is consistent with perhaps our most important observation. Specifically, larger concentrations of C_{70} enable longer separations between electron and hole during the initial charge separation—and the separation happens faster. Certainly the C_{70} crystallite size should increase with larger C_{70} concentration, promoting longer separations; perhaps the crystallinity also increases and/or the surface trap density decreases with the decreasing surface area density, elevating within-crystallite mobility and thus the rate. This farther, faster effect may promote charge separation and suppress polaron pair recombination, enhancing device performance.

In addition, a 1:1 mixture of DBP:C_{70} showed very small, very slow dynamics. This drastic reduction in carrier mobility compared to samples with more C_{70} suggests the C_{70} crystallinity is quite poor for the 1:1 mixture and/or the surface trap density is very high, harming the electron mobility. Also, trends in our data suggested that 'hot' polaron pairs may enhance the charge separation rate, so bluer absorption wavelengths produce charge separation more quickly.

Several important avenues for future work remain. The data raise several interesting questions such as the effect of crystallite size and crystallite size distribution, which are not fully answered. An X-ray or electron diffraction experiment could establish the size distribution more quantitatively.

References

[1] Xin Xiao, Jeramy D. Zimmerman, Brian E. Lassiter, Kevin J. Bergemann, and Stephen R. Forrest. A hybrid planar-mixed tetraphenyldibenzoperiflanthene/C_{70} photovoltaic cell. *Applied Physics Letters*, **102**:073302, (2013).

[2] Xin Xiao, Kevin J. Bergemann, Jeramy D. Zimmerman, Kyusang Lee, and Stephen R. Forrest. Small-molecule planar-mixed heterojunction photovoltaic cells with fullerene-based electron filtering buffers. *Advanced Energy Materials*, **4**:1301557, (2014).

[3] Daniel E. Wilcox and Jennifer P. Ogilvie. Fourier-transform time-resolved surface second harmonic generation for direct charge-transfer measurements. In *The 7th International Conference on Coherent Multidimensional Spectroscopy*, page 136, (2014).

[4] E. Riedle, M. Beutter, S. Lochbrunner, J. Piel, S. Schenkl, S. Spörlein, and W. Zinth. Generation of 10 to 50 fs pulses tunable through all of the visible and the NIR. *Applied Physics B*, **71**:457–465, (2000).

[5] D. Amarasinghe Vithanage, A. Devižis, V. Abramavičius, Y. Infahsaeng, D. Abramavičius, R. C. I. MacKenzie, P. E. Keivanidis, A. Yartsev, D. Hertel, J. Nelson, V. Sundström, and V. Gulbinas. Visualizing charge separation in bulk heterojunction organic solar cells. *Nature Communications*, **4**:2334, (2013).

[6] Robert W. Boyd. *Nonlinear Optics*. Academic Press, third edition, (2008).

[7] The Scipy community. Optimization and root finding (scipy.optimize). URL `http://docs.scipy.org/doc/scipy/reference/optimize.html`.

[8] Bong-Gi Kim, Kyeongwoon Chung, and Jinsang Kim. Molecular design principle of all-organic dyes for dye-sensitized solar cells. *Chemistry: A European Journal*, **19**:5220–30, (2013).

[9] Myeong H. Lee, Eitan Geva, and Barry D. Dunietz. Calculation from first-principles of golden rule rate constants for photoinduced subphthalocyanine/fullerene interfacial charge transfer and recombination in organic photovoltaic cells. *The Journal of Physical Chemistry C*, **118**:9780–9789, (2014).

[10] Peter Peumans, Soichi Uchida, and Stephen R. Forrest. Efficient bulk heterojunction photovoltaic cells using small-molecular-weight organic thin films. *Nature*, **425**:158–162, (2003).

[11] Harald Hoppe and Niyazi Serdar Sariciftci. Organic solar cells: An overview. *Journal of Materials Research*, **19**:1924–1945, (2004).

[12] Sam-Shajing Sun and Niyazi Serdar Sariciftci. *Organic Photovoltaics: Mechanisms, Materials, and Devices*. Taylor & Francis, (2005).

[13] Mark Van der Auweraer, Frans C. De Schryver, Paul M. Borsenberger, and Heinz Bassler. Disorder in charge transport in doped polymers. *Advanced Materials*, **6**:199–213, (1994).

[14] Paul M. Borsenberger and John J. Fitzgerald. Effects of the dipole moment on charge transport in disordered molecular solids. *The Journal of Physical Chemistry*, **97**:4815–4819, (1993).

[15] S. V. Novikov, D. H. Dunlap, V. M. Kenkre, P. E. Parris, and A. V. Vannikov. Essential role of correlations in governing charge transport in disordered organic materials. *Physical Review Letters*, **81**:4472–4475, (1998).

[16] S. V. Rakhmanova and E. M. Conwell. Electric-field dependence of mobility in conjugated polymer films. *Applied Physics Letters*, **76**:3822, (2000).

Chapter 5

Fast second-harmonic generation frequency-resolved optical gating using only a pulse shaper

Several important ultrafast experiments employ a pulse-shaper in a collinear geometry. Coherent control experiments [1, 2], pulse-shaper-assisted nonlinear microscopy [3, 4], and two-dimensional electronic spectroscopy in the all-collinear [5] and pump-probe geometries [6] all employ a pulse-shaper producing a single beam of ultrafast pulses. In all of these contexts, it is critical to minimize and measure pulse durations to optimize time resolution and the information content available from ultrafast measurements [7]. For example, in two-dimensional electronic spectroscopy transform-limited pulses are required in order to avoid peakshape distortions [8]. Many nonlinear microscopies require short pulse durations to optimize signal-to-noise [9]. In coherent control experiments, transform-limited pulse durations are not always necessary, but well-defined spectral phase functions are required [1].

A large number of pulse-measurement techniques exist for measuring pulse durations and spectral phase [7]; common techniques include frequency-resolved optical gating (FROG) [10], spectral interferometry for direct electric field reconstruction (SPIDER) [11], and multiphoton intrapulse interference phase scan (MIIPS) [12].

In the context of collinear pulse-shaping experiments, it is convenient to employ a collinear pulse-measurement technique where the pulse-shaper is the only active element and where no additional beams are required to characterize the pulses at the sample position. This avoids a large number of extra optics, motorized delay stages, and alignment time. The MIIPS method

satisfies these requirements, and is very useful for compressing pulses with a pulse-shaper [12]. However, it is a frequency-domain technique, and thus does not provide a direct measurement of pulse duration. Time-domain methods of measuring pulse duration are often useful since certain effects like spatial chirp [13] or phase noise [14] can cause frequency-domain methods to falsely report a well-compressed pulse, whereas a time-domain method would reveal the true longer pulse duration. Combining these expanded requirements suggests a pulse-shaped collinear FROG as the method of choice, as both SPIDER and MIIPS are frequency-domain techniques. In addition, a second-order FROG is preferred such a second-harmonic-generation FROG (SHG-FROG) because second-order FROGs are more sensitive than higher-order FROGs [7]. Many experiments require very weak pulses, such as nonlinear spectroscopy or microscopy on biological systems, making high sensitivity crucial.

There are several existing methods meeting the above criteria which can be performed with a pulse-shaper by directing the shaper to produce pairs of identical pulses with a controllable relative time-delay. One method uses two pulses of different polarizations in a type-II SHG crystal [15]. However, most pulse-shapers produce only one polarization of light. A second method is essentially a frequency-resolved interferometric autocorrelation [16]; the traditional SHG-FROG signal (as defined by Trebino [10]) is isolated from the interferometric trace using Fourier filtering. Alternatively, a different signal can be isolated from the frequency-resolved interferometric autocorrelation with Fourier filtering, yielding a new kind of FROG with a specialized phase-retrieval algorithm [17] although in my opinion this trace is not as intuitive as the standard SHG-FROG. It is even possible to analytically extract the spectral phase from the frequency-resolved interferometric autocorrelation trace [18], although this is fundamentally a frequency-domain technique. All of the above interferometric techniques require many time-delays between the two pulses in order to fully sample the interferometric trace; the Nyquist period is almost always much less than the pulse duration. This lengthens the data-acquisition time. Meanwhile, for very short pulses where the pulse duration begins to approach the Nyquist period, it becomes impossible to do Fourier filtering without distorting the FROG trace. This would happen when the width of the Fourier peaks

is comparable to the spacing between the Fourier peaks. I estimate that as the pulse duration becomes shorter than about two optical cycles (longer for non-Gaussian pulses), the Fourier filtering starts to introduce distortions.

Forget et al. [19] introduced a pulse-shaper-based 'baseband interferometric SHG-FROG' technique where the shaper produces a pair of identical pulses with a controllable relative time-delay and a controllable relative carrier-envelope phase. By choosing the relative carrier-envelope phase to correspond to the rotating frame, the required number of time-points is greatly reduced. However, the resulting trace is qualitatively different from the traditional SHG-FROG and requires a modified phase-retrieval algorithm; I again feel the resulting trace is not as intuitive as the standard SHG-FROG. Here I propose and demonstrate a new collinear SHG-FROG method combining four carrier-envelope phases with the same time-delay, making it possible to retrieve the traditional SHG-FROG signal so standard FROG software can be used and so that the trace is as intuitive as possible. This phase-cycled technique does not require many time-delays, nor does it require Fourier filtering. The technique is well-suited to almost any experiment using a pulse-shaper; all that is needed is a second-order nonlinear crystal such as beta barium borate (BBO) and a spectrometer.

I describe the phase-cycled FROG technique following the derivation of Stibenz and Steinmeyer [17], altering their derivation to allow for controllable carrier-envelope phase as permitted by a pulse shaper. The complex electric field of a pulse can be written $\mathscr{E}(t) = E(t)\exp(i\omega_0 t)$ where $E(t)$ is the complex amplitude and ω_0 is the carrier frequency. Only the relative phase between the two pulses matters for a FROG measurement, so it is only necessary to apply a phase ϕ to one of the pulses. The pair of pulses can then be written as $\mathscr{E}(t) + \mathscr{E}(t-\tau)\exp(i\phi)$ where τ is the relative time-delay between the two pulses. What is sent to the pulse-shaper to create the pulse-pair is the frequency-domain version of this, or $\tilde{\mathscr{E}}(\omega)\left[1 + \exp(-i\omega\tau + i\phi)\right]$. Therefore the measured spectral intensity of the collinear SHG-FROG is given by

$$I(\omega,\tau,\phi) = \left| \int_{-\infty}^{\infty} \left[\mathscr{E}(t) + \mathscr{E}(t-\tau)\exp(i\phi)\right]^2 \exp(-i\omega t)\, dt \right|^2 . \tag{5.1}$$

Continuing to follow Stibenz and Steinmeyer, substituting $\Delta\omega = \omega - 2\omega_0$ I define the second-harmonic of a single pulse as

$$E_{\text{SH}}(\Delta\omega) = \int_{-\infty}^{\infty} E^2(t) \exp(-i\Delta\omega t)\, dt. \tag{5.2}$$

The SHG-FROG field is then given by

$$E_{\text{FROG}}(\Delta\omega, \tau) = \int_{-\infty}^{\infty} E(t)E(t-\tau) \exp(-i\Delta\omega t)\, dt. \tag{5.3}$$

These definitions permit expansion of Equation 5.1:

$$\begin{aligned} I(\Delta\omega, \tau, \phi) = \\ \left| \left[1 + \exp(2i\phi - i(2\omega_0 + \Delta\omega)\tau)\right] E_{\text{SH}}(\Delta\omega) + 2\exp(i\phi - i\omega_0\tau) E_{\text{FROG}}(\Delta\omega, \tau) \right|^2. \end{aligned} \tag{5.4}$$

Expanding this further yields

$$\begin{aligned} I(\Delta\omega, \tau, \phi) =& 2\left|E_{\text{SH}}(\Delta\omega)\right|^2 + 4\left|E_{\text{FROG}}(\Delta\omega, \tau)\right|^2 \\ &+ 8\cos\left[\phi - (\omega_0 + \Delta\omega/2)\,\tau\right] \text{Re}\left[E_{\text{FROG}}(\Delta\omega, \tau) E^*_{\text{SH}}(\Delta\omega) \exp\left(i\Delta\omega\tau/2\right)\right] \\ &+ 2\cos\left[2\phi - (2\omega_0 + \Delta\omega)\,\tau\right] \left|E_{\text{SH}}(\Delta\omega)\right|^2. \end{aligned} \tag{5.5}$$

If four different carrier-envelope phases are combined, the cosine terms can be completely eliminated:

$$\begin{aligned} I(\Delta\omega, \tau, 0) + I(\Delta\omega, \tau, \pi/2) + I(\Delta\omega, \tau, \pi) + I(\Delta\omega, \tau, 3\pi/2) \\ = 8\left|E_{\text{SH}}(\Delta\omega)\right|^2 + 16\left|E_{\text{FROG}}(\Delta\omega, \tau)\right|^2. \end{aligned} \tag{5.6}$$

This is identical to the Fourier-filtered result given by Amat-Roldán et al. [16] and Stibenz and Steinmeyer [17]. It is simple to eliminate the τ-independent term by evaluating the above expression at a sufficiently large τ that the FROG term is zero and $8\left|E_{\text{SH}}(\Delta\omega)\right|^2$ is all that remains [16].

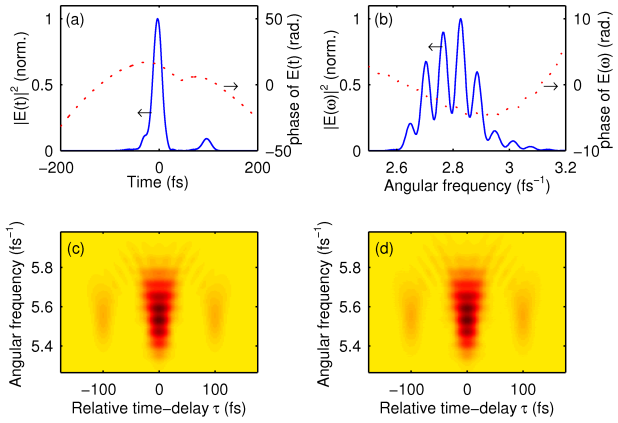

Figure 5.1: Phase-cycled SHG-FROG simulation results. (a) Temporal intensity and phase of the simulated test pulse, which is temporally a double-pulse with significant quadratic and cubic spectral phase. (b) Spectral intensity and phase of the simulated test pulse. (c) Simulated standard SHG-FROG trace of the test pulse. (d) Simulated phase-cycled collinear SHG-FROG trace of the test pulse, showing excellent agreement with (c).

This term can then be subtracted.

To explore the effectiveness of my technique, I performed both a computer simulation and an experimental demonstration. For the simulation, I calculated the scheme using a known test pulse. I chose a complicated test pulse to provide a more rigorous test. The simulated test pulse included a small double-pulse and exhibited both quadratic and cubic spectral phase. In Figure 5.1(a,b) the spectral intensity, spectral phase, temporal intensity, and temporal phase of the simulated test pulse are plotted. Figure 5.1(c) shows the simulated standard non-collinear SHG-FROG trace. Figure 5.1(d) shows the simulated phase-cycled collinear SHG-FROG trace. The simulation included shot noise and camera readout noise, modeled after the characteristics of the actual camera, with realistic intensity levels and averaging times. Roughly speaking, this corresponded to approximately a fifty-to-one signal-to-noise ratio for a single laser shot, with one hundred laser shots averaged per time-delay. The agreement between the standard and the phase-cycled-collinear SHG-FROG traces is excellent.

More simulated data are plotted in Figure 5.2, illustrating how the four phase shifts combine to remove the interferometric modulation. The four individual shifts (a-d), and the sum of the first two (e), and the sum of all four (f) are plotted, restricting τ to clearly show the modulation. Each of

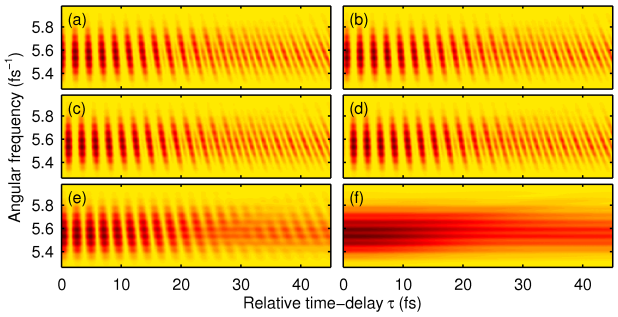

Figure 5.2: Phase-cycled SHG-FROG phase shift simulations. (a-d) Interferometric FROG traces of the simulated test pulse with 0, $\pi/2$, π, and $3\pi/2$ relative carrier-envelope phase shifts respectively, zoomed in along τ to show the interferometric modulation. (e) The sum of the first two phase shifts showing removal of the second-harmonic frequency. (f) The sum of all four phase shifts, showing removal of all modulation along τ; the modulation along the detection axis is part of the traditional SHG-FROG trace (see Figure 5.1).

the individual shifts shows modulation at both the fundamental and second-harmonic frequencies, but the sum of the first two shifts or last two shifts removes the second-harmonic modulation (this is especially visible at later times such as 30 fs). With all four, all interferometric modulation is removed.

As an experimental demonstration, I measured the phase-cycled collinear SHG-FROG trace of a compressed laser pulse. To perform this experiment, a titanium-doped sapphire oscillator (Femto Lasers Femtosource™ Synergy™) seeded a regenerative amplifier (Spectra-Physics Spitfire® Pro™) yielding 4 mJ, 30 fs pulses centered at 800 nm at a 1 KHz repetition rate. This powered a home-built two-stage non-collinear optical parametric amplifier generating broad-bandwidth light tunable over much of the visible spectrum [20, 21]. The beam passed through a FASTLITE Dazzler™ pulse-shaper, which provided the dispersion compensation, and it split the input beam into pairs of identical pulses with a controllable time-delay and relative carrier-envelope phase. The pulses were compressed by scanning the second-order spectral phase to maximize the second-harmonic intensity produced by focusing into a 10-micron-thick BBO (Eksma Optics). At the BBO, there were $\sim$20 nJ of energy in each of the two pulse copies with a spot size of $\sim$150 μm. The beam was filtered to remove most of the fundamental light (Hoya U-330) and focused into a spectrometer (Horiba Jobin-Yvon iHR320). The light was detected with a CCD camera (Princeton Instruments

PIXIS 100B with a UV coating). Figure 5.3(a) depicts a simplified schematic of the setup.

I used 40 time-delays between the two pulses spaced evenly between 0 and 150 fs; SHG-FROG traces are time-symmetric so only positive delays are necessary. This required 160 waveforms in the pulse shaper. I took data for 30 seconds. To extract the temporal amplitude and phase of the pulses, I used the MATLAB® code published by Rick Trebino's group [22]. Figure 5.3(b–e) shows the measured and extracted SHG-FROG traces, with the extracted temporal and spectral intensities and phases. The interferometric components are clearly absent from the data, demonstrating the phase-cycling is working as designed. The reconstruction matches the measured data well ($G' = 0.057$ [23]), showing measurement errors are minimal. The extracted temporal and spectral phase are near zero as expected for a compressed pulse, yielding a pulse-duration of 32 fs FWHM as shown in Figure 5.3(d).

For comparison with other methods, for a Fourier-filtered FROG variant I estimate needing $\sim$1200 waveforms, requiring roughly 7.5x more data-acquisition time. This estimate is based on a Nyquist period of the highest-frequency term being $\sim$0.5 fs, so 0.33 fs sampling out to 400 fs would take $\sim$1200 waveforms (careful choice of window could reduce the number of needed waveforms). Many ultrafast lasers have longer pulse durations than the present demonstration, causing the phase-cycled FROG method to be even faster relative to the Fourier-filtered FROGs. The amount of data required for a Fourier-filtered FROG scales with the pulse duration divided by the Nyquist period, while the amount of data required for the phase-cycled technique scales only with pulse complexity.

I conclude by observing that a wide variety of research groups use an ultrafast laser in a collinear geometry with a pulse-shaper; many of these groups do collinear nonlinear microscopy with a pulse-shaper. There are also groups doing pulse-shaper-assisted Fourier-transform spectroscopy [5, 6, 24] and groups doing pulse-shaper-assisted coherent control [1]. In all of these cases, a readily-accessible FROG is helpful. While MIIPS [12] and SPIDER [11] are certainly useful, they do not provide as direct a measure of pulse duration as a FROG. Fundamentally, they are all frequency-domain methods while FROG is fundamentally a time-domain method. Using

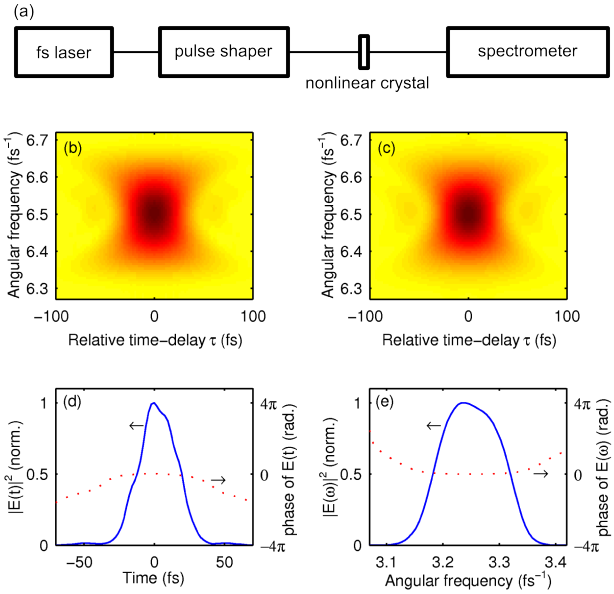

Figure 5.3: Phase-cycled SHG-FROG experimental results. (a) Diagram of experimental setup for the new phase-cycled technique. (b) Measured SHG-FROG trace using the technique. (c) Reconstructed SHG-FROG trace using the standard FROG algorithm; the reconstruction error is low at $G' = 0.057$. (d) Measured temporal intensity and phase showing a 31.6 fs pulse duration FWHM; linear component of temporal phase subtracted. (e) Measured spectral intensity and phase; linear component of spectral phase subtracted.

FROG as a cross-check against one of these other methods boosts confidence that the compressed laser pulse really is transform-limited.

While collinear FROGs suitable for use with a pulse-shaper have existed for approximately a decade, this phase-cycled SHG-FROG method saves time compared with Fourier-filtered variants and yields a standard SHG-FROG trace which is more intuitive than non-standard FROGs and which does not require specialized analysis software. These attributes make it a valuable tool for pulse measurement in pulse-shaping contexts.

Acknowledgments

The original version of this chapter may be found at the following reference: Daniel E. Wilcox, Franklin D. Fuller, and Jennifer P. Ogilvie. Fast second-harmonic generation frequency-resolved optical gating using only a pulse shaper. *Optics Letters*, **38**:2980–2983, (2013). `http://dx.doi.org/10.1364/OL.38.002980`

References

[1] Debabrata Goswami. Optical pulse shaping approaches to coherent control. *Physics Reports*, **374**:385–481, (2003).

[2] Warren S. Warren, Herschel Rabitz, and Mohammed Dahleh. Coherent control of quantum dynamics: the dream is alive. *Science*, **259**:1581–9, (1993).

[3] Jennifer P. Ogilvie, Delphine Débarre, Xavier Solinas, Jean-Louis Martin, Emmanuel Beaurepaire, and Manuel Joffre. Use of coherent control for selective two-photon fluorescence microscopy in live organisms. *Optics Express*, **14**:759, (2006).

[4] Igor Pastirk, Johanna Dela Cruz, Katherine Walowicz, Vadim Lozovoy, and Marcos Dantus. Selective two-photon microscopy with shaped femtosecond pulses. *Optics Express*, **11**:1695, (2003).

[5] Peifang Tian, Dorine Keusters, Yoshifumi Suzaki, and Warren S. Warren. Femtosecond phase-coherent two-dimensional spectroscopy. *Science*, **300**:1553–5, (2003).

[6] Jeffrey A. Myers, Kristin L. M Lewis, Patrick F. Tekavec, and Jennifer P. Ogilvie. Two-color two-dimensional Fourier transform electronic spectroscopy with a pulse-shaper. *Optics Express*, **16**:17420–8, (2008).

[7] Andrew M. Weiner. *Ultrafast Optics*. John Wiley & Sons, Inc., Hoboken, NJ, USA, (2009).

[8] Patrick F. Tekavec, Jeffrey A. Myers, Kristin L. M. Lewis, Franklin D. Fuller, and Jennifer P. Ogilvie. Effects of chirp on two-dimensional Fourier transform electronic spectra. *Optics Express*, **18**:11015, (2010).

[9] Jeffrey J. Field, Ramón Carriles, Kraig E. Sheetz, Eric V. Chandler, Erich E. Hoover, Shane E. Tillo, Thom E. Hughes, Anne W. Sylvester, David Kleinfeld, and Jeff A. Squier. Optimizing the fluorescent yield in two-photon laser scanning microscopy with dispersion compensation. *Optics Express*, **18**:13661, (2010).

[10] Rick Trebino. *Frequency-Resolved Optical Gating: The Measurement of Ultrashort Laser Pulses*. Springer, (2002).

[11] C. Iaconis and I. A. Walmsley. Spectral phase interferometry for direct electric-field reconstruction of ultrashort optical pulses. *Optics Letters*, **23**:792, (1998).

[12] Vadim V. Lozovoy, Igor Pastirk, and Marcos Dantus. Multiphoton intrapulse interference. IV. Ultrashort laser pulse spectral phase characterization and compensation. *Optics Letters*, **29**: 775, (2004).

[13] Selcuk Akturk, Xun Gu, Pablo Gabolde, and Rick Trebino. The general theory of first-order spatio-temporal distortions of Gaussian pulses and beams. *Optics Express*, **13**:8642, (2005).

[14] Justin Ratner, Günter Steinmeyer, Tsz Chun Wong, Randy Bartels, and Rick Trebino. Coherent artifact in modern pulse measurements. *Optics Letters*, **37**:2874–6, (2012).

[15] L. Gallmann, Günter Steinmeyer, D. H. Sutter, N. Matuschek, and U. Keller. Collinear type II second-harmonic-generation frequency-resolved optical gating for the characterization of sub-10-fs optical pulses. *Optics Letters*, **25**:269–71, (2000).

[16] Ivan Amat-Roldán, Iain G. Cormack, Pablo Loza-Alvarez, Emilio J. Gualda, and David Artigas. Ultrashort pulse characterisation with SHG collinear-FROG. *Optics Express*, **12**:1169, (2004).

[17] Gero Stibenz and Günter Steinmeyer. Interferometric frequency-resolved optical gating. *Optics Express*, **13**:2617, (2005).

[18] Ivan Amat-Roldán, David Artigas, Iain G. Cormack, and Pablo Loza-Alvarez. Simultaneous analytical characterisation of two ultrashort laser pulses using spectrally resolved interferometric correlations. *Optics Express*, **14**:4538, (2006).

[19] Nicolas Forget, Vincent Crozatier, and Thomas Oksenhendler. Pulse-measurement techniques using a single amplitude and phase spectral shaper. *Journal of the Optical Society of America B*, **27**:742, (2010).

[20] E. Riedle, M. Beutter, S. Lochbrunner, J. Piel, S. Schenkl, S. Spörlein, and W. Zinth. Generation of 10 to 50 fs pulses tunable through all of the visible and the NIR. *Applied Physics B*, **71**:457–465, (2000).

[21] T. Wilhelm, J. Piel, and E. Riedle. Sub-20-fs pulses tunable across the visible from a blue-pumped single-pass noncollinear parametric converter. *Optics Letters*, **22**:1494–6, (1997).

[22] Tsz Chun Wong and Rick Trebino. Trebino-group code. URL `http://frog.gatech.edu/code.html`.

[23] R. P. Scott, N. K. Fontaine, Jing Cao, Katsu Okamoto, B. H. Kolner, J. P. Heritage, and S. J. Ben Yoo. High-fidelity line-by-line optical waveform generation and complete characterization using FROG. *Optics Express*, **15**:9977, (2007).

[24] Sang-Hee Shim and Martin T. Zanni. How to turn your pump-probe instrument into a multidimensional spectrometer: 2D IR and Vis spectroscopies via pulse shaping. *Physical Chemistry Chemical Physics : PCCP*, **11**:748–61, (2009).

Chapter 6

Comparison of pulse compression methods using only a pulse shaper

6.1 Introduction

Pulse-shapers are commonly used in a variety of important ultrafast spectroscopy experiments: coherent control experiments [1, 2], pulse-shaper-assisted nonlinear microscopy experiments [3–5], and pulse-shaper-based two-dimensional electronic spectroscopy [6–9] are several examples. Minimizing pulse durations is critical for optimizing time resolution and the information content available from ultrafast measurements [10]. For example, many nonlinear microscopies require short pulse durations to optimize signal-to-noise [11]. Two-dimensional electronic spectroscopy requires transform-limited pulses to avoid peakshape distortions [12]. Coherent control experiments do not always require transform-limited pulse durations, but well-defined spectral phase functions are important [1].

When working with very short pulses, dispersion management becomes a critical aspect of the experiment. Third-, fourth-, and higher-order spectral phase distortions can have a significant effect on pulse duration and on pulse symmetry. Using a pulse-shaper is a flexible way to manage these high-order phase distortions. It is convenient for this pulse-shaper to be the only active element used in pulse measurement and compression, reducing alignment time and optics. Many techniques exist for measuring these high-order spectral phase distortions in general; some good sources include Walmsley and Dorrer [13] and Trebino [14]. Several more techniques are exclu-

sive to the present pulse-shaper-only context as given by Lozovoy et al. [15] and Forget et al. [16]. To my knowledge there has been no systematic study of how much time these pulse-shaper-only methods require to achieve a given amount of error. Some studies focus on very fast 'single shot' methods [17, 18] but these methods require dedicated optics and alignment time, and generally require intense pulses which are not always available. Other studies discuss how individual methods respond to noise [19–21], but do not predict how noise varies by method. I am aware of two direct experimental comparisons between a small number of methods [22, 23], but they reported experimental noise likely dominated by spatial and temporal pulse-overlap noise and laser noise. These are not issues for pulse-shaper-only methods because there is only one beam so pulse-overlap is not a noise source and rapid pulse-shape-cycling can eliminate laser noise. I investigate the speed of several pulse-shaper-only methods using a computer simulation, as measured by the amount of time required to achieve a similar accuracy of characterization. I perform the simulations on several different test cases of varying spectral phase and amplitude complexity.

One of the most common pulse-shaper-only pulse-compression techniques is multiphoton intrapulse interference phase-scan (MIIPS) [15]. To be clear, many pulse-shaper-only phase measurement techniques can be considered a formal multiphoton intrapulse interference phase-scan, including all of the phase-only methods discussed here. However, the algorithms used to convert measured data to measured phase vary widely between the original MIIPS algorithm and those other methods. For ease of terminology, here I use the term 'MIIPS' to refer to the original MIIPS algorithm. MIIPS is a simple and highly accurate integrated method for pulse compression that only requires a pulse-shaper that can perform phase shaping. Its accuracy makes it an excellent way to measure the group delay dispersion of a material [24]. A relatively large number of pulse-shapes—on the order of one hundred—are needed to measure a MIIPS trace. Further, a single round of the MIIPS algorithm only provides an approximate measure of the spectral phase; several rounds are required for an accurate measure.

Alternatively, a pulse-shaper-only frequency-resolved optical gating (FROG) [16, 25] or a pulse-shaper-only spectral interferometry for direct electric field reconstruction (SPIDER) [16]

could be used to measure the spectral phase. The pulse-shaper could then be set to compensate the measured distortions [26]. Ultimately, these techniques are less convenient than MIIPS because they require a shaper capable of both amplitude and phase shaping, which not all shapers can provide. Pulse-shaper-based FROG is additionally inconvenient because it is a form of SHG-FROG and therefore has a direction-of-time ambiguity.

A sonogram-like MIIPS variant named MIIPS-S demonstrated a remarkable ability to compensate very high order phase distortions [27]. However, this method requires both phase and amplitude shaping, and requires even more pulse-shapes than traditional MIIPS—on the order of one thousand. Further, the method's amplitude shaping discards most of the laser power and so signals are likely to be relatively weak, harming S/N.

Meanwhile, the dispersion scan method by Miranda et al. [28] (recently extended to pulse-shapers by Loriot et al. [29] as 'chirp scan') makes extremely few approximations, and due to its holistic data-fitting approach could be a particularly efficient way to measure spectral phase. It is additionally convenient because the pulse-shaper only needs to perform phase shaping. Another option is the Chirp Reversal Technique (CRT) [29] as a 'far-field' limit of the chirp scan technique. This method uses an impressively small amount of data, using only two pulse-shapes to measure the phase, thus having the potential to be particularly fast. I present a technique having a similar theory, but differing in the transformation from measured data to measured spectral phase, named Spectral Phase of Electric field by Analytic Reconstruction (SPEAR). Like CRT, SPEAR is computationally simple, but allows for more of the chirp scan data to be used than the CRT technique. After discussing the SPEAR theory, I experimentally demonstrate it. I then proceed to the computer simulation of the various methods, and discuss their strengths and weaknesses.

6.2 Theory of SPEAR

The methods here investigated all have well-known theory with the exception of SPEAR. Its theoretical background is similar to CRT's as described by Loriot et al. [29] but with a different

transformation from measured data to measured spectral phase. Fundamentally CRT and SPEAR work by adding enough quadratic spectral phase to the laser pulse so that only second-harmonic-generation (SHG) occurs at each laser frequency; there is little to no sum-frequency-generation (SFG) between different laser frequencies. Essentially these methods prevent SFG by adding linear chirp to introduce a temporal separation of the different laser frequencies. By looking at how the amplitude of the SHG changes as a function of chirp for each laser frequency, it is possible to extrapolate at what chirp each of those frequencies would be optimally compressed—the negative second derivative of the phase.

Here the SPEAR theory is briefly discussed in terms of the physical processes. Suppose a laser pulse $E(\omega)$ has unknown spectral amplitude $|E(\omega)|$ and unknown spectral phase $\varphi(\omega)$:

$$E(\omega) = |E(\omega)| \exp\left(-i\varphi(\omega)\right). \tag{6.1}$$

A quadratic known phase function is applied to the unknown pulse by the pulse-shaper:

$$E_i(\omega) = |E(\omega)| \exp\left(-i\varphi(\omega) - \frac{i}{2}\phi_2^{(i)}\left(\omega - \omega_0\right)^2\right), \tag{6.2}$$

where ω_0 is some central angular frequency, and $\phi_2^{(i)}$ is the chirp coefficient. There are multiple applied phase functions and each one has a $\phi_2^{(i)}$. As derived by Loriot et al. [29] in equation 5, in the far-field limit—meaning the applied chirps $\phi_2^{(i)}$ are sufficiently strong—a relatively simple expression exists for the spectral intensity of the SHG:

$$I_{SHG}^{(i)}(2\omega) = \beta \left| \frac{1}{\varphi''(\omega) + \phi_2^{(i)}} \right| |E(\omega)|^4, \tag{6.3}$$

where β is a constant of proportionality that describes the efficiency of the SHG process. This formula is the basis of the CRT and SPEAR methods, and it becomes exact in the limit of strong $\phi_2^{(i)}$. Essentially, the measured intensity at a second-harmonic frequency 2ω is related only to the characteristics of the pulse at laser frequency ω. The CRT authors used this relationship to derive

a formula for the second-derivative of the phase $\varphi''(\omega)$ using second-harmonic spectral intensity measurements $I^{(1)}_{SHG}(2\omega)$ and $I^{(2)}_{SHG}(2\omega)$ from two applied chirp-values $\phi_2^{(1)}$ and $\phi_2^{(2)}$; the formula is given in equation 6 of [29]:

$$\varphi''(\omega) \approx \frac{\phi_2^{(1)} I^{(1)}_{SHG}(2\omega) + \phi_2^{(2)} I^{(2)}_{SHG}(2\omega)}{I^{(1)}_{SHG}(2\omega) + I^{(2)}_{SHG}(2\omega)}. \tag{6.4}$$

On the other hand, SPEAR works by calculating a least-squares fit for $\varphi''(\omega)$ and $|E(\omega)|$ given several applied chirp-values and associated second-harmonic spectral intensity measurements. The fitting procedure minimizes the following weighted least-squares objective function $\mathcal{L}$ which consists of the sum of the squared residuals as compared to Equation 6.3:

$$\mathcal{L}(c,b) = \sum_{i,\omega} W_i(\omega) \left(I^{(i)}_{SHG}(2\omega) - \left| \frac{c(\omega)}{b(\omega) + \phi_2^{(i)}} \right| \right)^2. \tag{6.5}$$

In this objective function, $c(\omega)$ represents the best-fit estimate for $\beta |E(\omega)|^4$. $b(\omega)$ represents the best-fit estimate for $\varphi''(\omega)$. $W_i(\omega)$ represents the weighting factors, which should be chosen such that they approximate the inverse variance of the measurements $I^{(i)}_{SHG}(2\omega)$. I use

$$W_i(\omega) = \frac{1}{r + I^{(i)}_{SHG}(2\omega)}, \tag{6.6}$$

where r represents the known variance of the detector read noise ($\sqrt{r} \approx 11$ photoelectrons for our detector) and $I^{(i)}_{SHG}(2\omega)$—the measured spectral intensity—doubles as an estimate of the variance due to shot noise because the variance of a Poisson process is the same as its mean (this requires intensities measured in photoelectrons). Since independent variances add, $r + I^{(i)}_{SHG}(2\omega)$ is an estimate of the noise variance, leading to my chosen weight. Unfortunately, the absolute value in the objective function introduces a discontinuity in the objective function's gradient, making minimization unwieldy. However, in practice the sign of $b(\omega)+\phi_2^{(i)}$ is already known since $|\phi_2^{(i)}| \gg b(\omega)$. This permits an equivalent objective function lacking the absolute value that is consequently

easier to handle analytically:

$$\mathcal{L}(c,b) = \sum_{i,\omega} W_i(\omega) \left(I_{SHG}^{(i)}(2\omega) - \frac{s_i \cdot c\,(\omega)}{b\,(\omega) + \phi_2^{(i)}} \right)^2 . \tag{6.7}$$

Here, the values $s_i = \text{sgn}\left[b\,(\omega) + \phi_2^{(i)}\right]$ are known and constant. Solving for zero gradient with respect to the two unknowns gives an analytic equation for the best-fit $b(\omega)$ that can be quickly and deterministically solved to within machine precision using numerical methods such as Brent's [30] or Ridders' method [31] (I use Brent's method as implemented in the open-source `scipy.optimize` module [32]):

$$\left[\sum_i \frac{s_i \cdot W_i(\omega) I_{SHG}^{(i)}(2\omega)}{b\,(\omega) + \phi_2^{(i)}} \right] \left[\sum_i \frac{W_i(\omega)}{\left(b\,(\omega) + \phi_2^{(i)} \right)^3} \right] = \left[\sum_i \frac{W_i(\omega)}{\left(b\,(\omega) + \phi_2^{(i)} \right)^2} \right] \left[\sum_i \frac{s_i \cdot W_i(\omega) I_{SHG}^{(i)}(2\omega)}{\left(b\,(\omega) + \phi_2^{(i)} \right)^2} \right] . \tag{6.8}$$

The solution $b(\omega)$ of this equation constitutes the best-fit estimate for $\varphi''\,(\omega)$. This is the central difference between SPEAR and CRT: the data-to-phase transformation is derived in a least-squares sense and allows the data from more than two applied pulse-shapes to be used. More than two applied pulse-shapes can be desirable because it adds redundancy to the measurement. It is also convenient that the SPEAR formula is only marginally more complicated to program than the CRT formula. Once $b\,(\omega)$ is found, the following formula can be used to find $c(\omega)$, which is the best-fit estimate for $\beta\,|E(\omega)|^4$:

$$c(\omega) = \frac{\displaystyle\sum_i \frac{s_i \cdot W_i(\omega) I_{SHG}^{(i)}(2\omega)}{b\,(\omega) + \phi_2^{(i)}}}{\displaystyle\sum_i \frac{W_i(\omega)}{\left(b\,(\omega) + \phi_2^{(i)} \right)^2}} . \tag{6.9}$$

Once the two parameters $b(\omega)$ and $c(\omega)$ have been fit, the spectral and temporal amplitude and phase can be directly calculated. In practice $c(\omega)$ can be distorted relative to the squared spectral

intensity $\beta |E(\omega)|^4$. This depends on SHG crystal thickness and therefore phase-matching bandwidth and the spectral transmittance of any filters in between the crystal and the spectrometer. Other factors affecting $c(\omega)$ include any spectral distortions from the spectrometer itself including the grating, and any clipping on the entrance slit combined with spatial chirp in the beam. However, as noted by Miranda et al. [28] the measured data should only be distorted by a constant spectral filter—assuming the fundamental beam is not depleted by the SHG process—and so while $c(\omega)$ can be distorted, $b(\omega)$ remains correct.

In principle CRT and SPEAR do not require multiple iterations to produce a compressed pulse. However, any slight miscalibration or imperfection in the pulse-shaper or the spectrometer could mean that some MIIPS-like iteration may be required to converge to the solution. Specifically, a single iteration yields a measure of $\varphi''(\omega)$ which is sent to the pulse-shaper to compensate; the next iteration runs CRT or SPEAR starting from a mostly-compensated phase. In addition, some trials may be necessary to find a good value of applied chirp large enough to prevent SFG but small enough to have good signal-to-noise; Appendix B discusses how to do this. In my experience, using well-chosen applied chirp values, one or two iterations works well; the first provides a good measure of $\varphi''(\omega)$ and the second provides validation and corrects for any miscalibration or imperfection errors.

6.3 Experimental demonstration of SPEAR

For an experimental demonstration of SPEAR, a Spectra-Physics Mai Tai SP™ oscillator seeded a Spectra-Physics Spitfire Pro™ regenerative amplifier yielding 4 mJ, ∼40 fs pulses at 1 kHz centered at 800 nm. This powered a home-built double-pass noncollinear optical parametric amplifier [33, 34] yielding broadband pulses tunable over much of the visible. A FASTLITE Dazzler™ pulse-shaped the result. The resulting beam, which was a few tens of nanojoules of pulse-energy, was focused into a 10 micron thick beta barium borate (BBO) crystal (Eksma Optics). The output was collimated, filtered to remove most of the fundamental light, focused into a spectrometer

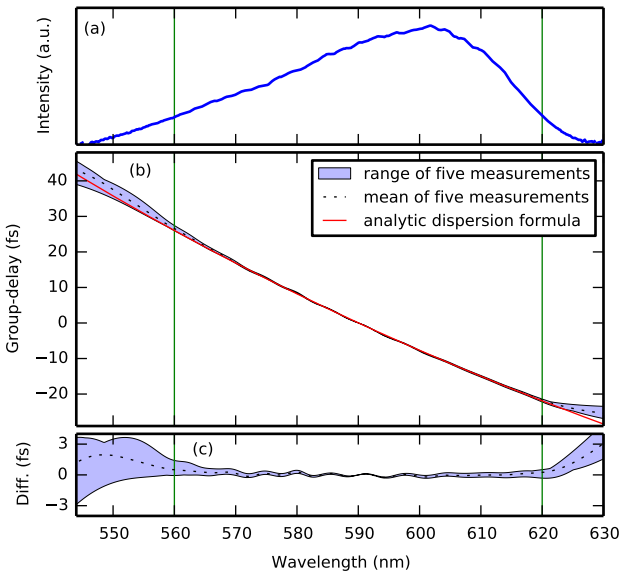

Figure 6.1: Demonstration of the SPEAR method. (a) Measured $\sqrt{c(\omega)}$ which is a measure of spectral intensity. (b) Measured and true group-delay as a function of wavelength relative to the group-delay of 590 nm. (c) Difference between measured and true group-delay. Red solid line, the true group-delay based on the published dispersion formula. Black dotted line, the average of five independent measurements of the group-delay using the SPEAR method. Blue shaded area, the range of those five measurements showing excellent repeatability and accuracy everywhere there is significant spectral intensity. Vertical green lines, boundaries of the region of interest over which there is significant spectral intensity.

(Horiba Jobin-Yvon iHR-320) and detected by a CCD (Princeton Instruments PIXIS-100B with UV coating).

The dispersion of a glass window in between the pulse-shaper and the nonlinear crystal was measured. I used SPEAR on an uncompressed pulse, with and without the window in the optical path. Four values of ϕ_2 were used, ± 1500 fs^2 and ± 1167 fs^2. Only two seconds of laser time (two thousand laser shots) were used per measurement. The difference between the measured $b(\omega)$ for the with-glass and without-glass measurements is proportional to the intrinsic group delay dispersion of the glass. Integrating that difference with respect to ω yields the group delay as a function of laser frequency. The window's thickness was measured with a Mitutoyo ABSOLUTE digital caliper ($\sim$10 micron precision) to be T=2.09 mm thick. The material was CDGM H-K9L, which has a published dispersion formula $n(\lambda)$ [35]. The spectral phase $\phi(\omega) = n(\omega)T\omega/c$ was differentiated to compute the group delay $d\phi/d\omega$ as a function of wavelength. Figure 6.1 shows the com-

puted group delay and the measured group delay. The measurements were performed five times, and the full range of those measurements are plotted, together with the mean. This demonstrates exceptional repeatability and accuracy; the group-delay dispersion at 590 nm, using data from 560nm to 620nm (the spectral region exhibiting significant laser intensity) is measured at 147.4 fs^2 but calculated at 146.7 fs^2, a 0.5% difference. This slight error can be attributed to window thickness measurement error, pulse-shaper calibration error, and/or spectrometer calibration error. For comparison with previous measurements in the literature, Figure 4 of [24] shows measured fs^2 of deionized water using several different path-lengths; much like the present measurement they best-fit a polynomial to the detection bandwidth. After fitting along detection bandwidth, they best-fit a line through different path-lengths as shown in Figure 4(b); their R^2 value indicates the residual noise is 3–4 fs^2 for any one path-length. My 0.7 fs^2 error compares favorably with this.

6.4 Speed comparison of pulse-shaper-only spectral phase measurements

Having established the SPEAR method, I compare the speed of several pulse-shaper-only methods using a computer simulation. The speed metric was the minimum number of laser shots needed to achieve about a femtosecond of RMS error of spectral group-delay over a spectral region-of-interest. I use spectral group-delay as the metric because it corresponds to actual pulse broadening, unlike spectral phase or spectral group-delay dispersion. I also evaluated the amount of computation time each method required. The simulation included shot noise, camera readout noise, finite BBO thickness, and finite spectrometer resolution. It neglected laser noise because in my experience that can typically be overcome by rapid pulse-shape-cycling. The source code for the simulation is available under an open-source license to facilitate scrutiny of the results [36].

Four different test cases centered at 650 nm were used, with varying complexity of spectral intensity and phase, as shown in Figure 6.2. These test cases characterized how the different methods perform with different types of pulse complexity. Case 1 was a relatively simple somewhat-

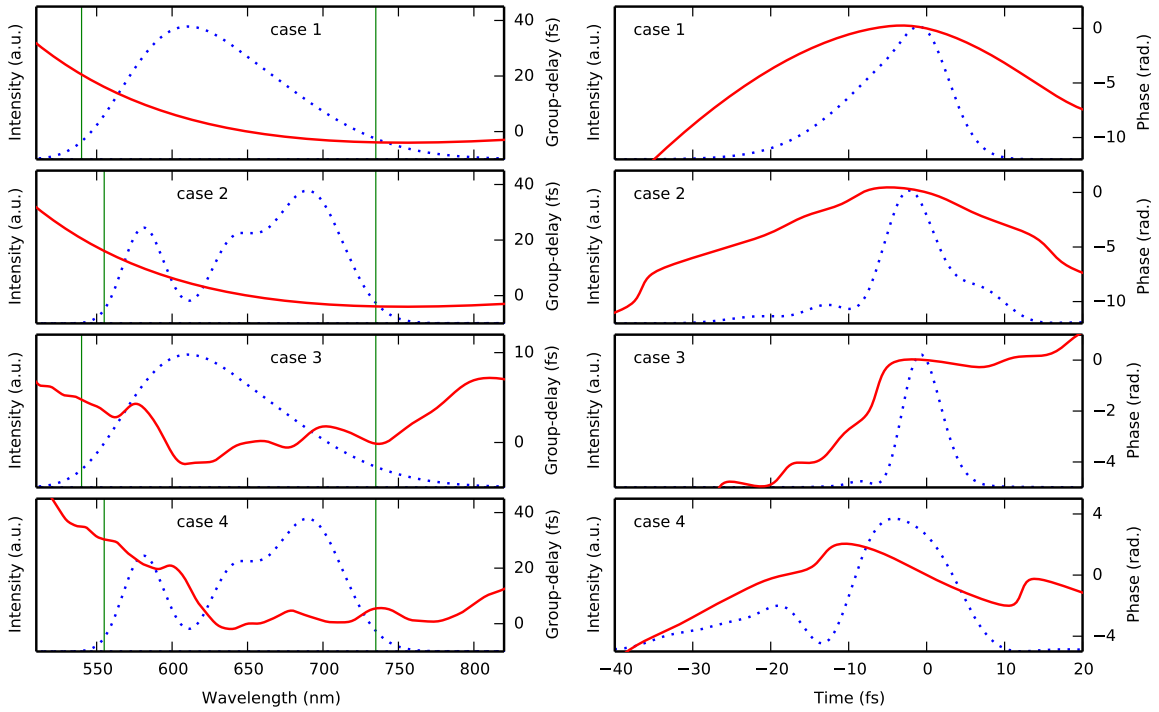

Figure 6.2: Depiction of the four test cases being used to evaluate pulse-shaper-only spectral phase measurements. Left column, spectral intensity and group-delay; right column, temporal intensity and phase. Blue dotted line, spectral or temporal intensity; red solid line, spectral group-delay or temporal phase; vertical thin green lines: edges of region of interest with appreciable spectral intensity.

asymmetric Gaussian spectral intensity profile and a relatively simple spectral phase consisting of second-order and third-order components. Case 2 was a more complex spectral intensity with multiple peaks, but the same simple spectral phase. Case 3 had the simpler intensity profile with a spectral phase close to zero, but with significant ripple in the group delay dispersion, as might occur with several bounces off of chirped mirrors or by transmission through certain antireflection coatings or interference filters. While the pulse was not significantly broadened in the time domain, its symmetry was significantly reduced. Case 4 had the more-complex spectral intensity and a strong ripple to the spectral phase, in addition to second-order and third-order components.

Second harmonic generation was simulated by squaring the time-domain field and multiplying by a spectral filter mimicking a 200 micron spot-size (D4σ) on a ten micron thick BBO crystal cut for optimal phase-matching. Because the simulation included shot noise and read noise, signal-to-noise increased dramatically with increasing pulse energy; I used 20 nJ of energy per laser shot,

Table 6.1: Comparison of different methods' speed, both laser time and computation time.

METHOD	LASER TIME (SHOTS)	COMPUTE TIME (MINUTES)
SPIDER	10K–2M	negligible
MIIPS	260–2M	negligible
MIIPS-S	210K–180M	negligible
FROG	2100	3–4
CRT	250–15K	negligible
SPEAR	250–15K	negligible
Chirp-scan	30	< 1

which is a typical energy for our two-dimensional electronic spectroscopy experiments. Spectral and temporal discretization of the simulated pulses and spectral filters were chosen to be significantly higher than the Nyquist limit over the entire field profile. The added noise and spectrometer-induced blurring were based on the physical characteristics of our spectrometer and camera. See Appendix C for more details. None of the retrieval methods were provided with knowledge of the BBO's SHG efficiency curve, nor were any special parameters given for different test cases.

For each method, 120 independent simulations were performed, in order to characterize the distribution of retrieved results. In Figures 6.3, 6.4, 6.5, and 6.6, the percentiles of the retrieved distributions are plotted for cases 1, 2, 3, and 4 respectively. Table 6.1 summarizes the results; a detailed discussion is given below.

6.4.1 SPIDER

For the SPIDER simulations, the pulse-shaper created a sum of two time-delayed pulse replicas and a bandwidth-limited chirped pulse, as described by Forget et al. [16] in equation 26. There were four applied pulse-shapes representing different sums and differences of the relevant pulse components. A $\tau = 200$ fs separation was used between pulse replicas to minimize pulse overlap and therefore reduce error. Different test cases needed different levels of spectral resolution; case 1 used spectral resolution $\delta\omega = 0.34$ fs^{-1} (55 THz), case 2 had $\delta\omega = 0.25$ fs^{-1} (39 THz), case 3 had $\delta\omega = 0.098$ fs^{-1} (16 THz), and case 4 had $\delta\omega = 0.058$ fs^{-1} (9.4 THz). The chirped pulse had $\tau/\delta\omega$ of quadratic spectral phase and a $10\delta\omega$-bandwidth bandpass filter. The biases in the retrieved

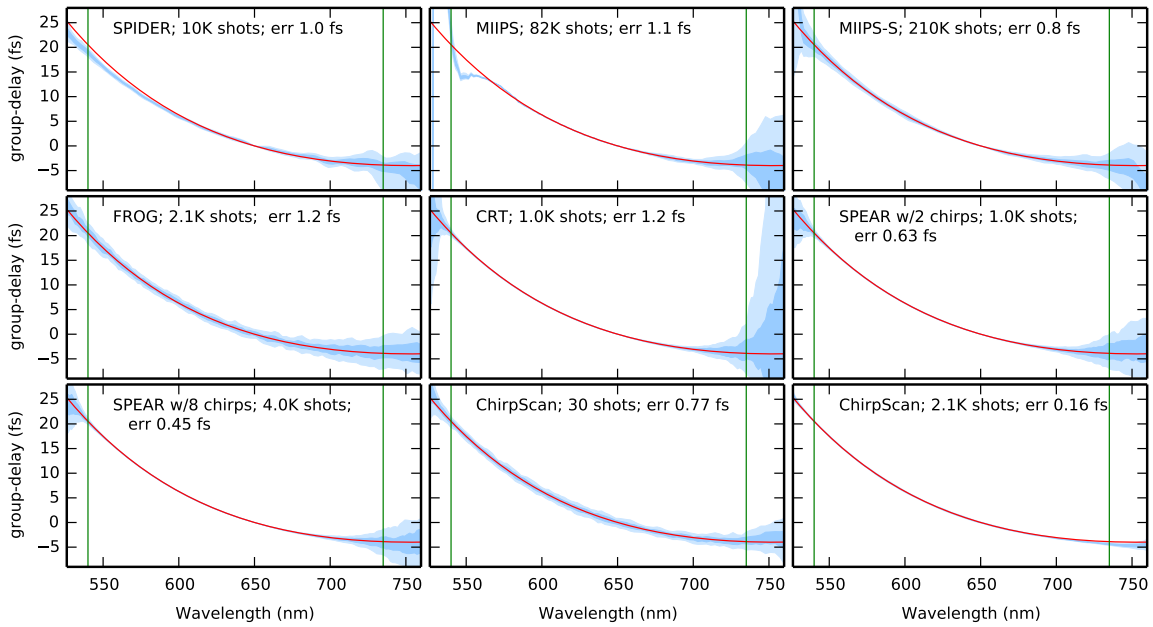

Figure 6.3: Simulated spectral group-delay and retrieved distribution of spectral group delay for the case 1 pulse under the methods being simulated. Retrieved group-delays from FROG were artificially rectified to have the correct direction of time. Red line, the simulated true spectral group-delay. Dark shaded area, the 30th to 70th percentiles of the retrieved group-delay; light shaded area, the 10th to 90th percentiles. Vertical green lines, boundaries of the spectral region of interest. Retrieved group-delay errors are root-mean-square deviations between retrieved and true group-delay over the region of interest.

group-delays are due the limited spectral resolution. Smaller bias can be achieved with smaller $\delta\omega$, but that reduces the signal strength, requiring more laser shots to mitigate the noise, which decreases as the square root of the number of laser shots. Because the signals were weak, SPIDER was slow, requiring 10,000 laser shots for case 1, 40,000 shots for case 2, 500,000 shots for case 3, and 2,000,000 shots for case 4. Computation time for converting measured data to measured phase was negligible.

6.4.2 MIIPS

For MIIPS to achieve the necessary spectral resolution to see the ripples in the spectral group delay, α as defined by Xu et al. [23] was increased from the default 1.5π to 30π for case 1, 2.0π for case 2, 70π for case 3, and 120π for case 4. $\gamma = 4$ fs was used with 64 pulse shapes per MIIPS iteration. Four MIIPS iterations achieved convergence. The step-like behavior of the measured

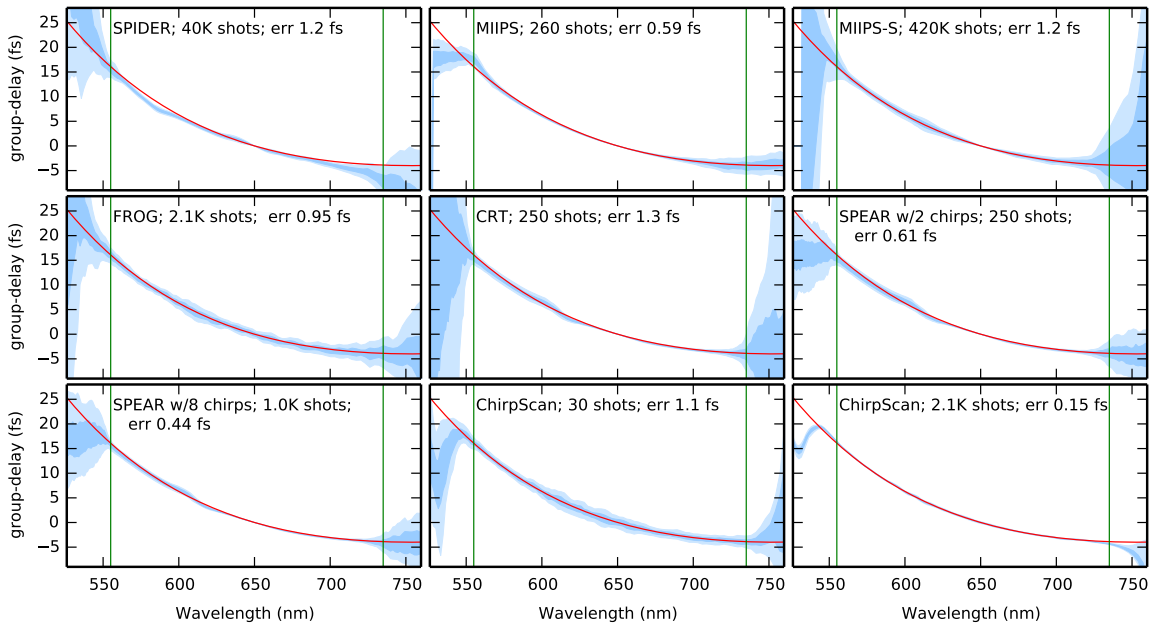

Figure 6.4: Simulated spectral group-delay and retrieved distribution of spectral group delay for the case 2 pulse under the methods being simulated. Retrieved group-delays from FROG were artificially rectified to have the correct direction of time. Red line, the simulated true spectral group-delay. Dark shaded area, the 30th to 70th percentiles of the retrieved group-delay; light shaded area, the 10th to 90th percentiles. Vertical green lines, boundaries of the spectral region of interest. Retrieved group-delay errors are root-mean-square deviations between retrieved and true group-delay over the region of interest.

group-delay comes from the number of pulse-shapes used per iteration. If more pulse-shapes are used per iteration, the retrieved group-delay becomes smoother, but more laser pulses are needed. I used 81,920 shots for case 1, 256 shots for case 2, 327,680 for case 3, and 1,966,080 for case 4. I found that the MIIPS algorithm tended to be biased in spectral regions where the spectral intensity and spectral group-delay and SHG efficiency are strongly sloped (see Figure C.1 for the SHG efficiency); the problem is especially visible in cases 1 and 3 on the blue edge of the spectrum, although case 2 shows it as well. The bias dominated the retrieved error of case 1 until I increased the spectral resolution by increasing α. Unfortunately, this made the signal weaker and so the number of laser shots needed to be increased to compensate. Case 2 didn't show the bias problem nearly as much, and so I could use low spectral resolution and a quite low number of laser shots were needed. Cases 3 and 4 both required much higher spectral resolution to see the ripples, which made the signals weak and required many more laser shots to average out the noise. In addition,

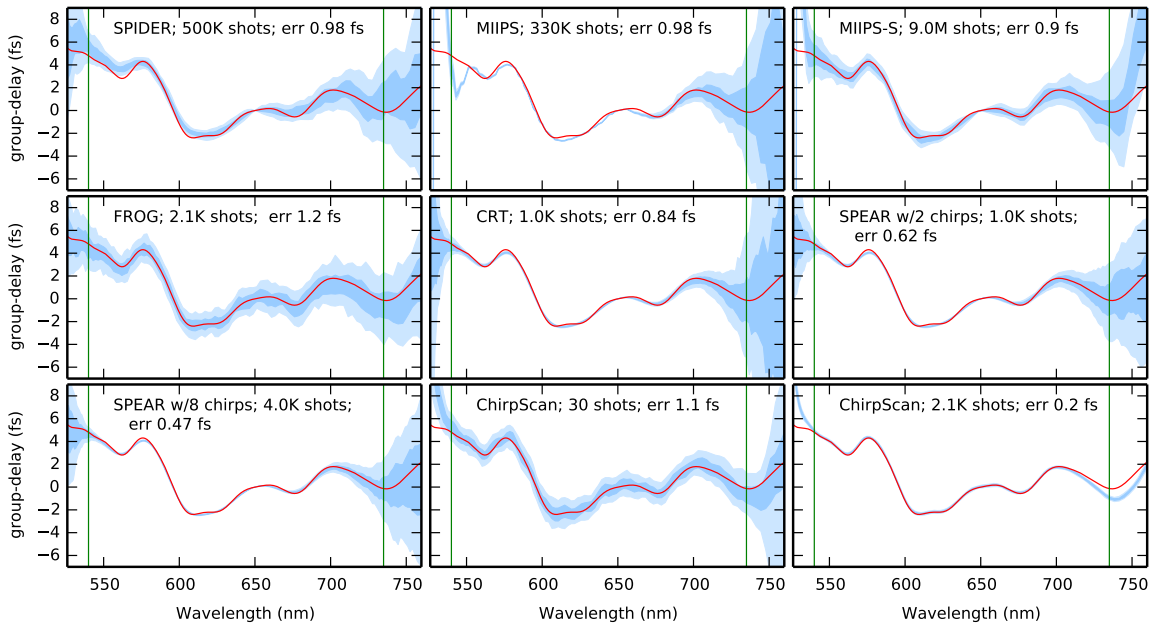

Figure 6.5: Simulated spectral group-delay and retrieved distribution of spectral group delay for the case 3 pulse under the methods being simulated. Retrieved group-delays from FROG were artificially rectified to have the correct direction of time. Red line, the simulated true spectral group-delay. Dark shaded area, the 30th to 70th percentiles of the retrieved group-delay; light shaded area, the 10th to 90th percentiles. Vertical green lines, boundaries of the spectral region of interest. Retrieved group-delay errors are root-mean-square deviations between retrieved and true group-delay over the region of interest.

large spectral regions of low spectral intensity such as the red side of cases 1 and 3 tended to accumulate more errors, since the noisy measured group-delay dispersion (GDD) integrated to produce variable smooth errors over that spectral region; this required more laser shots on those cases. Another reason why many laser shots were needed to average out the observed noise is because of the way the MIIPS noise scales with spectral intensity; the ratio R of the noise on the edges of the spectrum to the noise in the middle of the spectrum is much larger than SPIDER. This is because SPIDER measures sum-frequency signals between a narrowband reference sub-pulse and the rest of the pulse, so the signal scales linearly with the spectral field. On the other hand, traditional MIIPS only creates second-harmonic-generation of a single part of the pulse at a time, so the signal scales with the spectral field squared. Computation time for converting measured data to measured phase was negligible.

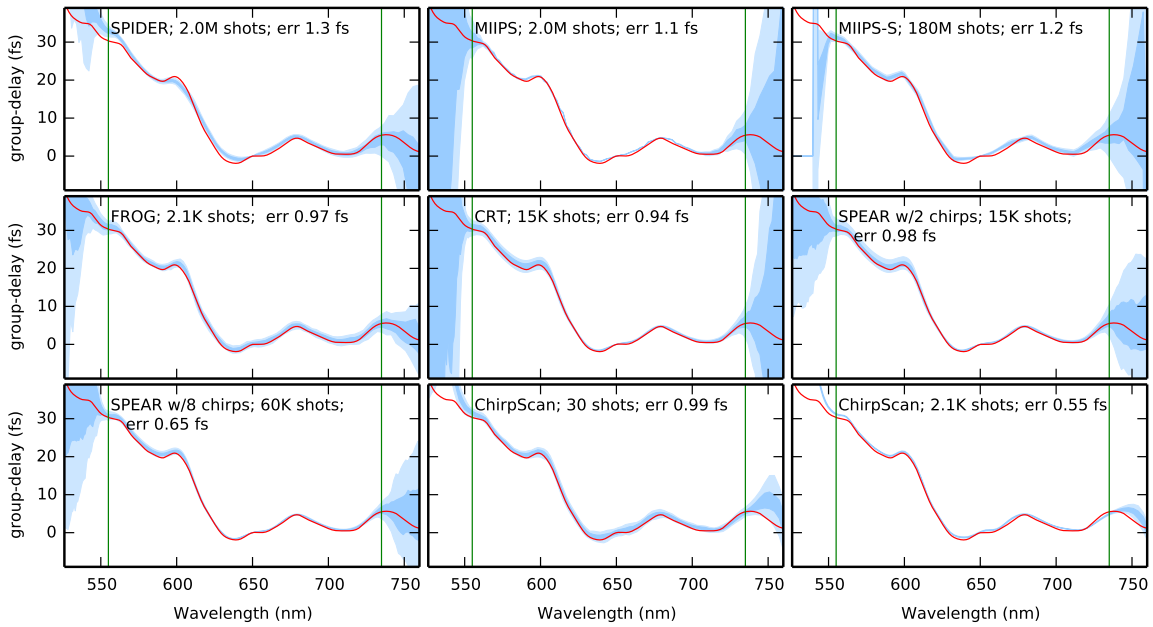

Figure 6.6: Simulated spectral group-delay and retrieved distribution of spectral group delay for the case 4 pulse under the methods being simulated. Retrieved group-delays from FROG were artificially rectified to have the correct direction of time. Red line, the simulated true spectral group-delay. Dark shaded area, the 30th to 70th percentiles of the retrieved group-delay; light shaded area, the 10th to 90th percentiles. Vertical green lines, boundaries of the spectral region of interest. Retrieved group-delay errors are root-mean-square deviations between retrieved and true group-delay over the region of interest.

6.4.3 MIIPS-S

The sonogram-like MIIPS-S method is nice because it is unbiased in its estimates of group-delay. However, because the signal is generated by two narrowband pulses with a tiny fraction of the total laser power, the signal is very weak and so many laser shots are required to average out the noise. Further, many pulse-shapes are scanned which further increases the number of laser shots required. I controlled the spectral resolution by dividing the region of interest into k equal-sized T-slits as defined in [27]. For cases 1 and 2 I used $k = 9$, and for cases 3 and 4 I used $k = 15$. The time-delay between the two T-slits was scanned in 15 steps from $-10k$ fs to $10k$ fs. I used two iterations of the method as suggested in [27]. I needed very large numbers of laser shots, ranging from 210,000 shots for case 1 to 180,000,000 shots for case 4. That said, the noise ratio R was more similar to SPIDER than that of traditional MIIPS. This is because like SPIDER, MIIPS-S

measures sum-frequency signals between a narrowband reference sub-pulse and the rest of the pulse, so the signal scales linearly with the spectral field.

6.4.4 FROG

I was unable to get sufficiently good results with the standard generalized-projections-based FROG inversion algorithm, for two reasons. First, many time-delays are required to sample sufficiently large delays such that the FROG trace decays to zero, while satisfying the Fourier relationship between the time and frequency grids that the FROG algorithm requires. Second, the algorithm requires non-negative data and so all negative values are replaced with zero. This made the tails of the trace have an average positive value, when they really average to zero. Therefore the retrieval algorithm adds noise to the retrieved pulse to increase the amplitude of the tails of the retrieved trace. Smoothing the data before replacing non-negative values with zero helps, but not enough. My solution was to use a chirp-scan-like direct fitting algorithm described in Appendix C; this allowed for fewer pulse-shapes and better accuracy of fitting. There was no need to force the data to be non-negative. Perhaps surprisingly, the significant modulation imposed by the finite thickness of the BBO (see Figure C.1) caused negligible aberrations in the results. For the FROG simulation parameters, there were thirty-five time-delays T_i according to the formula $T_i = a \sinh(i/b)$, for i an integer in the range $[0,\, 34]$. The constants a and b were chosen such that $a/b = 1\,\text{fs}$ and such that the last T_i was 60 fs. This nonlinear spacing of the time-delays provided good performance both for the nearly-compressed pulse in case 3, which needed more time-delays near time zero, and the more-chirped pulses in the other cases, which needed more time-delays far from time zero. Four phase cycles were used per time-delay as described in Chapter 5. Instead of adding the phase cycles together, the data for all of the measured pulse-shapes were simultaneously directly fitted. Due to FROG's direction-of-time ambiguity, in this simulation the retrieved traces were artificially rectified to have the correct time-direction, for the purpose of meaningful comparison. The noise ratio R was especially good; I believe that is because the time-delay-scanning nature of FROG allows for good sum-frequency-generation to occur between the weak portions of the pulse and the

many of the strong portions of the pulse. 2,100 laser shots per FROG trace were needed; there were no significant changes in performance for the different cases. Three or four minutes of computation time were needed for the fitting algorithm on a workstation computer.

6.4.5 CRT and SPEAR

There are actually two scenarios for using CRT or SPEAR. In the first one, a chirp-scan is taken and CRT or SPEAR is used to provide an initial guess to the nonlinear optimization of the chirp-scan algorithm. Here, SPEAR is likely to be the better option because more than two of the data-points can be used at once: as many data-points as can be considered 'far-field' can be used. The extra data provides redundancy and improves signal-to-noise. The second scenario utilizes CRT or SPEAR exclusively for pulse-compression; the chirp-scan least-squares fitting algorithm is not used. Only two far-field applied chirps are involved. To capture these different scenarios, I performed three simulations: one of CRT with two chirps, one of SPEAR with the same chirps and the same number of laser shots, and one of SPEAR with eight chirps and the same number of laser shots per pulse-shape as the other two. For the CRT simulation and the two-chirp SPEAR simulation, the applied chirps were -300 fs^2 and 300 fs^2, except for case 4 which needed more spectral resolution and therefore used -1000 fs^2 and 1000 fs^2. For the eight-chirp SPEAR simulation, I used four positive and four negative chirps, starting at the CRT chirps and moving outward in increments of 50 fs^2. CRT showed excellent performance in the middle of the spectrum, although much poorer performance on the edges. The two-chirp SPEAR simulation has nearly identical performance to CRT in the middle of the spectrum, but more reasonable results on the edges, allowing for a slight improvement in accuracy most of the time. I believe this is because the SPEAR equation (Equation 6.8) has a solution between the positive-s_i and negative-s_i values of $\phi_2^{(i)}$ whenever the S/N is reasonable; when the equation has no solution the S/N is known to be poor, and a regularized result can be returned ensuring $|\phi_2^{(i)}| \gg b(\omega)$. As expected, the eight-chirp SPEAR simulation does better than the CRT and two-chirp SPEAR simulations. Both CRT and SPEAR had relatively strong signals and so required relatively small numbers of laser shots, with 1,000 shots in cases 1

and 3, 300 shots in case 2, and 15,000 shots in case 4. Both of the methods have a noise ratio R comparable to MIIPS, because they rely on pure second-harmonic-generation of each portion of the pulse. For the same reason, the measured GDD was relatively noisy in the dip region of cases 2 and 4 near 610 nm and so the slope of the retrieved group-delay was noisy at 610 nm. This is visible in Figures 6.4 and 6.6 where the retrieved group-delay appears noisy for frequencies bluer than 610 nm. The retrieved group-delay of any one simulation actually tracks the true-group delay quite nicely over that whole spectral region bluer than 610 nm, but the offset is different for each one due to that noisy slope at 610 nm. In addition, large spectral regions of low spectral intensity such as the red side of cases 1 and 3 tended to accumulate more errors, much like MIIPS. Computation time for converting measured data to measured phase was negligible for both methods.

6.4.6 Chirp-scan

For the chirp-scan method, there were ten applied quadratic phases, linearly spaced in increments of about 44 fs^2 over a range of -200 fs^2 to 200 fs^2. I found that large numbers of applied chirps were unnecessary and that large scan ranges were unnecessary. The algorithm producing the measured phase from the measured data is described in Appendix C. The measured bias and noise are both low. Perhaps surprisingly, the significant modulation imposed by the finite thickness of the BBO (see Figure C.1) caused negligible aberrations in the results, much like FROG. The noise ratio R was comparable to FROG, since again the weak portions of the pulse interacted with many of the strong portions of the pulse. Only 30 laser shots were needed because the signals were very strong because the applied chirps were weak; there were no significant changes in performance for different test cases. Approximately one minute of computation time was needed for the fitting algorithm on a workstation computer. I also simulated the method with the same amount of laser time as FROG (2,100 laser shots) yielding significantly better accuracy than FROG; the computation time increased with more laser shots but remained smaller than FROG's.

6.5 Discussion

On the surface these simulations could seem to indicate that the chirp-scan method should be used exclusively over the other methods, due to the dramatically smaller amount of laser time required for good signal-to-noise. However, there are several considerations that might affect which pulse-compression method is best for a particular application. For example, the computational time for the chirp-scan algorithm can be the limiting factor instead of laser time. In this case, CRT or SPEAR seem the best choices, keeping the laser time down while minimizing the computational time. On the other hand, for low-repetition-rate systems chirp-scan is likely optimal. For pulses with spectral 'holes,' MIIPS, CRT, and SPEAR may be problematic because the relative group delay between the two sides of the hole is unmeasurable. High-energy pulses do not have a sensitivity concern and so large numbers of laser shots are unnecessary. In this case CRT might be the most convenient method, being the simplest of the methods allowing for only two pulse-shapes (and therefore only two laser shots). There are many other cases not tested here, that may have special requirements: extremely strong phase modulations might make FROG or chirp-scan the best options, since all of the methods except FROG and chirp-scan get dramatically slower with more complex pulses. Octave-spanning pulses may present additional difficulties, since the fundamental and second harmonics spectrally overlap. Also, the present study did not address the issue of pulse-shaper spectral resolution: low-resolution and/or pixelated shapers might not be able to create the pulse-shapes required by some of these methods. For example, Comin et al. [37] report MIIPS exhibiting phase-wrapping problems when used with high spectral resolution like the present study. Therefore in cases with low-resolution pulse-shapers chirp-scan may be the best option because it uses small applied phase functions. Further, the present study did not address several more considerations: laser noise, pixel-to-pixel variations in detector quantum efficiency, detector 1/f noise, detector dark current and associated shot noise, spectrometer-coupling noise, nonlinearities in pulse-shaper response, spatio-temporal coupling from the pulse-shaper, pulse-shaper misalignment, and imperfect calibration of the pulse-shaper.

I observe three trends across methods. First, FROG and chirp-scan perform equally well with

both simple and complex pulses; the other methods get much slower with increasing complexity. Second, methods requiring both phase and amplitude shaping (SPIDER, MIIPS-S, and FROG) on average performed worse than methods requiring only phase shaping (MIIPS, CRT, SPEAR, and chirp-scan). This is reasonable because the amplitude-shaped methods necessarily discard some of the laser power, decreasing the signal strength. Finally, methods with weak applied phases (low-resolution MIIPS, CRT, SPEAR, and chirp-scan) perform better than methods with strong applied phases (SPIDER, high-resolution MIIPS, MIIPS-S, and FROG), probably because strong applied phases decrease the nonlinear signal strength.

6.6 Conclusions

Following investigation of the speed of several pulse-shaper-only techniques, a wide variety of performance was observed in several typical simulated cases. Chirp-scan consistently required the smallest amount of laser time to achieve a femtosecond of RMS error by far, and required less than a minute of computation time. CRT and SPEAR also required small amounts of laser time and negligible amounts of computation time. The other methods were generally slower.

The new method SPEAR has proven to be a reliable pulse-compression technique. It is accurate and fast in terms of measurement and computation time. It can be a drop-in replacement for MIIPS because it has the same experimental requirements, so it could be useful to a wide variety of researchers using pulse-shapers since it automates the pulse-compression. It especially has an advantage when the spectral phase drifts over time, due to the improved speed. Even in the absence of drift, the improved speed of compression can be very convenient.

Acknowledgments

The original version of this chapter may be found at the following reference: Daniel E. Wilcox and Jennifer P. Ogilvie. Comparison of pulse compression methods using only a pulse shaper. *Journal of the Optical Society of America B*, **31**:1544–1554 (2014). http://dx.doi.org/10.1364/JOSAB.31.001544

References

[1] Patrick Nuernberger, Gerhard Vogt, Tobias Brixner, and Gustav Gerber. Femtosecond quantum control of molecular dynamics in the condensed phase. *Physical chemistry chemical physics : PCCP*, **9**:2470–97, (2007).

[2] Warren S. Warren, Herschel Rabitz, and Mohammed Dahleh. Coherent control of quantum dynamics: the dream is alive. *Science*, **259**:1581–9, (1993).

[3] Jennifer P. Ogilvie, Delphine Débarre, Xavier Solinas, Jean-Louis Martin, Emmanuel Beaurepaire, and Manuel Joffre. Use of coherent control for selective two-photon fluorescence microscopy in live organisms. *Optics Express*, **14**:759, (2006).

[4] Igor Pastirk, Johanna Dela Cruz, Katherine Walowicz, Vadim Lozovoy, and Marcos Dantus. Selective two-photon microscopy with shaped femtosecond pulses. *Optics Express*, **11**:1695, (2003).

[5] Meredith H. Brenner, Dawen Cai, Joel A. Swanson, and Jennifer P. Ogilvie. Two-photon imaging of multiple fluorescent proteins by phase-shaping and linear unmixing with a single broadband laser. *Optics Express*, **21**:17256, (2013).

[6] Peifang Tian, Dorine Keusters, Yoshifumi Suzaki, and Warren S. Warren. Femtosecond phase-coherent two-dimensional spectroscopy. *Science*, **300**:1553–5, (2003).

[7] Sang-Hee Shim and Martin T. Zanni. How to turn your pump-probe instrument into a multidimensional spectrometer: 2D IR and Vis spectroscopies via pulse shaping. *Physical Chemistry Chemical Physics : PCCP*, **11**:748–61, (2009).

[8] Jeffrey A. Myers, Kristin L. M. Lewis, Patrick F. Tekavec, and Jennifer P. Ogilvie. Two-color two-dimensional Fourier transform electronic spectroscopy with a pulse-shaper. *Optics Express*, **16**:17420–8, (2008).

[9] Franklin D. Fuller, Daniel E. Wilcox, and Jennifer P. Ogilvie. Pulse shaping based two-dimensional electronic spectroscopy in a background free geometry. *Optics Express*, **22**: 1018, (2014).

[10] Andrew M. Weiner. *Ultrafast Optics*. John Wiley & Sons, Inc., Hoboken, NJ, USA, (2009).

[11] Jeffrey J. Field, Ramón Carriles, Kraig E. Sheetz, Eric V. Chandler, Erich E. Hoover, Shane E. Tillo, Thom E. Hughes, Anne W. Sylvester, David Kleinfeld, and Jeff A. Squier. Optimizing

the fluorescent yield in two-photon laser scanning microscopy with dispersion compensation. *Optics Express*, **18**:13661, (2010).

[12] Patrick F. Tekavec, Jeffrey A. Myers, Kristin L. M. Lewis, Franklin D. Fuller, and Jennifer P. Ogilvie. Effects of chirp on two-dimensional Fourier transform electronic spectra. *Optics Express*, **18**:11015, (2010).

[13] Ian A. Walmsley and Christophe Dorrer. Characterization of ultrashort electromagnetic pulses. *Advances in Optics and Photonics*, **1**:308, (2009).

[14] Rick Trebino. *Frequency-Resolved Optical Gating: The Measurement of Ultrashort Laser Pulses*. Springer, (2002).

[15] Vadim V. Lozovoy, Igor Pastirk, and Marcos Dantus. Multiphoton intrapulse interference. IV. Ultrashort laser pulse spectral phase characterization and compensation. *Optics Letters*, **29**: 775, (2004).

[16] Nicolas Forget, Vincent Crozatier, and Thomas Oksenhendler. Pulse-measurement techniques using a single amplitude and phase spectral shaper. *Journal of the Optical Society of America B*, **27**:742, (2010).

[17] Daniel J. Kane and Rick Trebino. Single-shot measurement of the intensity and phase of an arbitrary ultrashort pulse by using frequency-resolved optical gating. *Optics Letters*, **18**:823, (1993).

[18] C. Dorrer, B. de Beauvoir, C. Le Blanc, S. Ranc, J.-P. Rousseau, P. Rousseau, J.-P. Chambaret, and F. Salin. Single-shot real-time characterization of chirped-pulse amplification systems by spectral phase interferometry for direct electric-field reconstruction. *Optics Letters*, **24**:1644, (1999).

[19] David N. Fittinghoff, Kenneth W. DeLong, Rick Trebino, and Celso L. Ladera. Noise sensitivity in frequency-resolved optical-gating measurements of ultrashort pulses. *Journal of the Optical Society of America B*, **12**:1955, (1995).

[20] M. E. Anderson, L. E. E. de Araujo, E. M. Kosik, and I. A. Walmsley. The effects of noise on ultrashort-optical-pulse measurement using SPIDER. *Applied Physics B*, **70**:S85–S93, (2000).

[21] S. Yeremenko, A. Baltuška, M. S. Pshenichnikov, and D. A. Wiersma. Phase-amplitude retrieval: SHG FROG vs. SPIDER. In *Conference on Lasers and Electro-Optics, 2000. (CLEO 2000).*, pages 476–477, (2000).

[22] L. Gallmann, D. H. Sutter, N. Matuschek, G. Steinmeyer, and U. Keller. Techniques for the characterization of sub-10-fs optical pulses: a comparison. *Applied Physics B*, **70**:S67–S75, (2000).

[23] Bingwei Xu, Jess M. Gunn, Johanna M. Dela Cruz, Vadim V. Lozovoy, and Marcos Dantus. Quantitative investigation of the multiphoton intrapulse interference phase scan method for simultaneous phase measurement and compensation of femtosecond laser pulses. *Journal of the Optical Society of America B*, **23**:750, (2006).

[24] Yves Coello, Bingwei Xu, Tricia L. Miller, Vadim V. Lozovoy, and Marcos Dantus. Group-velocity dispersion measurements of water, seawater, and ocular components using multiphoton intrapulse interference phase scan. *Applied Optics*, **46**:8394, (2007).

[25] Daniel E. Wilcox, Franklin D. Fuller, and Jennifer P. Ogilvie. Fast second-harmonic generation frequency-resolved optical gating using only a pulse shaper. *Optics Letters*, **38**:2980, (2013).

[26] J. Garduño Mejía, A. Greenaway, and D. Reid. Designer femtosecond pulses using adaptive optics. *Optics Express*, **11**:2030, (2003).

[27] Dmitry Pestov, Vadim V. Lozovoy, and Marcos Dantus. Single-beam shaper-based pulse characterization and compression using MIIPS sonogram. *Optics Letters*, **35**:1422–4, (2010).

[28] Miguel Miranda, Cord L. Arnold, Thomas Fordell, Francisco Silva, Benjamín Alonso, Rosa Weigand, Anne L'Huillier, and Helder Crespo. Characterization of broadband few-cycle laser pulses with the d-scan technique. *Optics Express*, **20**:18732–43, (2012).

[29] Vincent Loriot, Gregory Gitzinger, and Nicolas Forget. Self-referenced characterization of femtosecond laser pulses by chirp scan. *Optics Express*, **21**:24879, (2013).

[30] Richard P. Brent. *Algorithms for Minimization Without Derivatives*. Prentice-Hall, Edgewood Cliffs, NJ, (1973).

[31] C. Ridders. A new algorithm for computing a single root of a real continuous function. *IEEE Transactions on Circuits and Systems*, **26**:979–980, (1979).

[32] The Scipy community. Optimization and root finding (scipy.optimize). URL `http://docs.scipy.org/doc/scipy/reference/optimize.html`.

[33] E. Riedle, M. Beutter, S. Lochbrunner, J. Piel, S. Schenkl, S. Spörlein, and W. Zinth. Generation of 10 to 50 fs pulses tunable through all of the visible and the NIR. *Applied Physics B*, **71**:457–465, (2000).

[34] T. Wilhelm, J. Piel, and E. Riedle. Sub-20-fs pulses tunable across the visible from a blue-pumped single-pass noncollinear parametric converter. *Optics Letters*, **22**:1494–6, (1997).

[35] CDGM. CDGM Optical Glass Products Database. URL `http://www.cdgmgd.com/en/asp/`.

[36] Daniel Edward Wilcox. Pulse-shaping pulse-measurement simulations, (2014). URL `http://github.com/dewilcox/PulseshapingPulsemeasurementSimulations`.

[37] Alberto Comin, Richard Ciesielski, Giovanni Piredda, Kevin Donkers, and Achim Hartschuh. Compression of ultrashort laser pulses via gated multiphoton intrapulse interference phase scans. *Journal of the Optical Society of America B*, **31**:1118, (2014).

[38] Ichiro Shoji, Hirotaka Nakamura, Keisuke Ohdaira, Takashi Kondo, Ryoichi Ito, Tsutomu Okamoto, Koichi Tatsuki, and Shigeo Kubota. Absolute measurement of second-order nonlinear-optical coefficients of β-BaB_2O_4 for visible to ultraviolet second-harmonic wavelengths. *Journal of the Optical Society of America B*, **16**:620, (1999).

[39] Richard H. Byrd, Peihuang Lu, Jorge Nocedal, and Ciyou Zhu. A Limited Memory Algorithm for Bound Constrained Optimization. *SIAM Journal on Scientific Computing*, **16**: 1190–1208, (1995).

Chapter 7

Conclusions

This dissertation describes several innovations and scientific advances. In order to improve the signal-to-noise ratio of very weak TRSHG signals from organic photovoltaics, in Chapter 2 we developed a new version of it employing optical heterodyne detection. The new setup is much less sensitive to stray light and read noise than our initial non-interferometric implementation. The fully-linear interferometer is easy to use and align, and is very phase-stable. The heterodyne detection also measures both the amplitude and phase of the SHG; Chapter 4 exploits this to remove a background signal. The collinear geometry aids time resolution: non-collinear nonlinear spectroscopies have a spatial variation in the time delay between pump and probe, leading to a temporal smear that harms time resolution. The lack of temporal smear in the collinear geometry permits the use of very large laser spot sizes, enhancing signal strength in our typical constrained-laser-fluence experimental situation.

Chapter 3 progressed to measuring charge transfer in organic photovoltaic films using the TRSHG method. We measured a $\sim$0.1 ps^{-1} charge transfer rate for a SubPc / C_{60} bilayer film, and compared it to theoretical calculations of the rate. We used a fully quantum mechanical theoretical framework based on Fermi's golden rule. Two different optimized SubPc / C_{60} configurations were used in the calculations, but in real devices it is likely that a wide variety of SubPc / C_{60} configurations are present due to SubPc's irregular shape. Therefore our theoretical calculations were expected to be an upper bound for the experimentally-measured rate, as was observed. Our framework for comparing theory to experiment will continue to be useful for any future work employing

more realistic SubPc / C_{60} geometries.

In Chapter 4 we continued our TRSHG measurements on a DBP / C_{70} bulk heterojunction. This heterojunction boasts impressive conversion efficiency [1, 2] but has a surprising concentration dependence. Specifically, only one part DBP to eight parts C_{70} yields the best performance. We therefore investigated ultrafast charge dynamics as a function of concentration. We came to several interesting conclusions. In particular, it appears that photoexcitation is followed by a relatively fast initial charge separation event where the electron and hole separate by several nanometers, measured along the direction of the external electric field. After the initial charge separation, they separate much more slowly. Our best explanation for this effect is that the electrons are quite mobile within the C_{70} crystallites but take some time to hop from crystallite to crystallite. Surprisingly, the kinetics of this initial separation followed a $1/(1+kt)$ simplified power law, suggesting an exponential size distribution of the crystallites. This crystallite-based explanation of our data dovetails nicely with perhaps our most important observation. Specifically, larger concentrations of C_{70} enable longer separations between electron and hole during the initial charge separation—and the separation happens faster. Certainly the C_{70} crystallite size should increase with larger C_{70} concentration, promoting longer separations; perhaps the crystallinity also increases, elevating within-crystallite mobility and thus the rate. This farther, faster effect may promote charge separation and suppress polaron pair recombination, enhancing device performance.

Moving on to ultrafast pulse measurements, in Chapter 5 I describe a new FROG technique employing only a pulse shaper, using fewer pulse shapes than previous pulse-shaper-only techniques that yield a straightforward SHG-FROG trace. This enables more rapid acquisition of such traces, reducing the influence of laser noise and increasing productivity. A FROG measurement—because it is a very direct measure of pulse duration—helps ensure effects like pulse front tilt, spatial chirp, and phase noise are negligible. In Chapter 6 I describe a new pulse measurement technique named SPEAR that enables a particularly fast and direct measure of the spectral phase of an ultrafast pulse. In our experience, this method is much more precise and repeatable than FROG measurements for real-world use. It is also much faster than the MIIPS method we'd contemplated. Once

SPEAR was introduced, pulse compression to $<$15 fs became routine in the Ogilvie group. I then became very interested in which methods perform the best in general, so Chapter 6 also presents an extensive computer simulation comparing the signal-to-noise of several pulse-shaper-only pulse measurement techniques. The simulation included shot noise and read noise, but not laser noise. The performance disparity between methods was surprisingly large: methods differ by several orders of magnitude. The best-performing methods—chirp reversal technique (CRT), SPEAR, and chirp scan—are all quite new. I hope that many researchers will change their pulse measurement methods from commonly-used older methods such as MIIPS or SPIDER to these newer methods. This will enable them to reduce the amount of time they spend on pulse measurement and compression.

There are many possibilities for future research extending this work. The TRSHG experiment itself can be extended in several useful ways. *Phasing* the data is one possibility; at present only relative changes in SHG phase are measured but absolute knowledge of the SHG phase could enhance comparisons to microscopic models of SHG generation. I am particularly excited about another possibility, using broadband probe pulses for TRSHG, since different spectral regions could have different resonances with different kinds of charge transfer states. This TRSHG variant would have two measurement axes: a time axis T and a detection frequency ω. I hope it will perform much like transient absorption spectroscopy, where tracking multiple kinds of states at once is a key ability. My coworker Andrew Niedringhaus is already planning out such an experiment. It would be very straightforward to combine the pump wavelength tuning approach of Chapter 4 with the broadband probe, yielding a measurement with a pump frequency axis ω_1, a probe detection frequency axis ω_3, and a time axis T. This would be very analogous to two-dimensional electronic spectroscopy (2DES) [3–6], but would have the distinct advantage of probing charge transfer. For better time resolution, it would be straightforward to instead use two broadband pump pulses with a time-delay t_1 between them; the pump frequency axis would be obtained by Fourier transforming over the t_1 axis as in Fourier-transform 2DES. Phase cycling translates perfectly from Fourier-transform 2DES to this Fourier-transform TRSHG. I've already done a preliminary demonstration

of this [7]; Andrew is planning to continue that work.

Having developed heterodyne-detected TRSHG, there are many further possibilities for research on organic photovoltaics. It is interesting that copper pthalocyanine / C_{60}, a seemingly-similar system to our SubPc / C_{60} one, yields charge transfer times two orders of magnitude faster, >10 ps^{-1} [8, 9]. A survey of what kinds of (sub)phthalocyanine / fullerene heterojunctions produce what kinds of charge transfer rates might yield a predictive semi-empirical or even fully ab-initio law relating molecules to charge transfer rates. This could greatly improve understanding of devices. As mentioned above, a careful structural characterization of interfaces could be key here. Meanwhile, a survey of high-performance organic photovoltaics would also be interesting; for example the Forrest group has mentioned 'push-pull' molecules that yield especially good performance—even better than DBP—and TRSHG could give insights into why they perform so well. Measuring polaron-pair recombination rates could also be useful for device researchers, since it is a major loss mechanism. Measuring the recombination rates would require a much larger experimental temporal range—nanoseconds to microseconds—but it would be feasible at the recently-funded Laboratory for Ultrafast Multidimensional Optical Spectroscopy (LUMOS) at the University of Michigan.

Some recent high-profile work [10, 11] has suggested that charge transfer in organic photovoltaics may be enhanced vibronically. While suggestive, these experiments were not conclusive and further work must be done to establish this claim. Since they used visible probe pulses, I am concerned there may be other signals in addition to the charge transfer ones, contaminating their results. I can see a few different experiments that could settle the question more fully. A 2DES experiment with a NIR probe would be more believable, since there are fewer signals in the NIR besides the charge-transfer ones. A suitably short ($<$7 fs) 700–900 nm probe pulse can be generated using a degenerate optical parametric amplifier (DOPA) [12]; Andrew Niedringhaus has already made us one so this experiment would be straightforward. TRSHG would be even more believable, being an even more direct measure of charge transfer than a NIR absorptive probe. To achieve the needed time resolution, the Fourier-transform version of TRSHG with broadband,

very short, pump and probe pulses is probably necessary. Finally, a coherent control experiment, where the pump pulse is phase-shaped to drive a vibrational mode [13], could provide very direct evidence of vibronic enhancement of charge transfer. This could work well with either a NIR absorptive or a SHG probe.

Many other systems would be interesting to study via TRSHG. Dye-sensitized solar cells are an obvious candidate, as are hybrid organic / inorganic solar cells based on organometal halide perovskites [14]. Biological photosynthetic complexes such as Photosystem II—the water-splitting complex in plants and cyanobacteria [15]—could be particularly interesting, since the charge transport pathway is complex. Some difficulties would first need to be overcome; these complexes are large proteins with a single reaction center that separates the charges, and the proteins usually reside in solution. This presents two difficulties: first, to achieve appreciable optical density the sample will need to be many microns thick—making the sample much thicker than an optical wavelength, in contrast to organic photovoltaic films which are only tens of nanometers thick. This means that *phase matching* may be an issue, since the phase velocities of the probe and signal frequencies differ. I estimate the sample thickness would need to be kept to $\lesssim$10 microns, which would require very high concentration. However, such high concentrations have been reported [16]. Second, as the charges move, the average electric field will change very little, since the carrier number density is necessarily low. However, the fields next to the carriers will be much higher. Chlorophylls and pheophytins are important components of the charge transport pathway, and so their electric fields are likely to be high as the charges separate. They have a large absorption component at $\sim$650 nm, and so a $\sim$1400 nm probe wavelength would yield a signal at $\sim$700 nm, which is quasi-resonant with those absorptions. The nonlinear susceptibility $\chi^{(3)}$ of the chlorophylls and pheophytins would likely be increased by orders of magnitude, due to the resonant enhancement, and so the signal from their electric fields would be enhanced relative to the bulk signal from the average electric field in the sample.

It is difficult to predict how pulse measurement methods will evolve; FROG methods especially are very mature and so any future improvements are likely to be incremental. It is possible

that a totally new time-domain method could arise; I observe in Chapter 6 that phase-only methods generally work better than amplitude-and-phase methods. Therefore while traditional FROG pulse shapes are of the form $S(\omega,\tau) = [1 + \exp(-i\omega\tau)]/2$, a phase-only pulse shape of the form $S(\omega,\tau) = \exp[-i\sin((\omega-\omega_0)\tau)]$ might provide time-domain information with better signal-to-noise. It wouldn't need to be phase-cycled and may therefore have multiple practical advantages over the FROG method described. More generally, the field of optimal pulse measurement methods is quite young, so there are innumerable possibilities for optimizing pulse measurement. Many people use pulse measurement techniques that are not based on a pulse shaper, so we could investigate which no-pulse-shaper methods perform best. Alternatively, while Chapter 6 compares several existing methods, we could investigate which method performs best in a global sense, out of the set of all possible pulse-measurement methods. Such an investigation would likely be based on information theory; I've already done some preliminary work in this area. Laser noise and other non-idealities are other important considerations for future research: how do different methods perform in the presence of these non-idealities? Are certain methods particularly sensitive or insensitive to them? Extremely large bandwidths such as octave-spanning pulses cause problems for the methods analyzed in Chapter 6 because the fundamental and second harmonic pulses overlap spectrally; how can we accurately measure such large bandwidths using a pulse shaper? One possibility would be a collinear geometry based on cross-polarized wave generation, which has no bandwidth restrictions and which phase-matches very well.

References

[1] Xin Xiao, Jeramy D. Zimmerman, Brian E. Lassiter, Kevin J. Bergemann, and Stephen R. Forrest. A hybrid planar-mixed tetraphenyldibenzoperiflanthene/C_{70} photovoltaic cell. *Applied Physics Letters*, **102**:073302, (2013).

[2] Xin Xiao, Kevin J. Bergemann, Jeramy D. Zimmerman, Kyusang Lee, and Stephen R. Forrest. Small-molecule planar-mixed heterojunction photovoltaic cells with fullerene-based electron filtering buffers. *Advanced Energy Materials*, **4**:1301557, (2014).

[3] David M. Jonas. Two-dimensional femtosecond spectroscopy. *Annual Review of Physical Chemistry*, **54**:425–63, (2003).

[4] Jeffrey A. Myers, Kristin L. M. Lewis, Patrick F. Tekavec, and Jennifer P. Ogilvie. Two-color two-dimensional Fourier transform electronic spectroscopy with a pulse-shaper. *Optics Express*, **16**:17420–8, (2008).

[5] Patrick F. Tekavec, Jeffrey A. Myers, Kristin L. M. Lewis, and Jennifer P. Ogilvie. Two-dimensional electronic spectroscopy with a continuum probe. *Optics Letters*, **34**:1390–2, (2009).

[6] Franklin D. Fuller, Daniel E. Wilcox, and Jennifer P. Ogilvie. Pulse shaping based two-dimensional electronic spectroscopy in a background free geometry. *Optics Express*, **22**: 1018, (2014).

[7] Daniel E. Wilcox and Jennifer P. Ogilvie. Fourier-transform time-resolved surface second harmonic generation for direct charge-transfer measurements. In *The 7th International Conference on Coherent Multidimensional Spectroscopy*, page 136, (2014).

[8] L. G. Kaake, A. Jailaubekov, K. J. Williams, and X.-Y. Zhu. Probing ultrafast charge separation at organic donor/acceptor interfaces by a femtosecond electric field meter. *Applied Physics Letters*, **99**:083307, (2011).

[9] Askat E. Jailaubekov, Adam P. Willard, John R. Tritsch, Wai-Lun Chan, Na Sai, Raluca Gearba, Loren G. Kaake, Kenrick J. Williams, Kevin Leung, Peter J. Rossky, and X.-Y. Zhu. Hot charge-transfer excitons set the time limit for charge separation at donor/acceptor interfaces in organic photovoltaics. *Nature Materials*, **12**:66–73, (2013).

[10] Sarah Maria Falke, Carlo Andrea Rozzi, Daniele Brida, Margherita Maiuri, Michele Amato, Ephraim Sommer, Antonietta De Sio, Angel Rubio, Giulio Cerullo, Elisa Molinari, and Christoph Lienau. Coherent ultrafast charge transfer in an organic photovoltaic blend. *Science*, **344**:1001–5, (2014).

[11] Yin Song, Scott N. Clafton, Ryan D. Pensack, Tak W. Kee, and Gregory D. Scholes. Vibrational coherence probes the mechanism of ultrafast electron transfer in polymer-fullerene blends. *Nature Communications*, **5**:4933, (2014).

[12] A. M. Siddiqui, G. Cirmi, D. Brida, F. X. Kärtner, and G. Cerullo. Generation of $<$7 fs pulses at 800 nm from a blue-pumped optical parametric amplifier at degeneracy. *Optics Letters*, **34**:3592–4, (2009).

[13] Erik M. Grumstrup, Justin C. Johnson, and Niels H. Damrauer. Enhanced triplet formation in polycrystalline tetracene films by femtosecond optical-pulse shaping. *Physical Review Letters*, **105**:257403, (2010).

[14] Mingzhen Liu, Michael B. Johnston, and Henry J. Snaith. Efficient planar heterojunction perovskite solar cells by vapour deposition. *Nature*, **501**:395–8, (2013).

[15] Robert E. Blankenship. *Molecular Mechanisms of Photosynthesis*. Wiley-Blackwell, (2002).

[16] N. P. Pawlowicz, M.-L. Groot, I. H. M. van Stokkum, J. Breton, and R. van Grondelle. Charge separation and energy transfer in the photosystem II core complex studied by femtosecond midinfrared spectroscopy. *Biophysical Journal*, **93**:2732–42, (2007).

APPENDIX A

Supporting Information: Ultrafast charge-transfer dynamics at the boron subphthalocyanine chloride / C_{60} heterojunction: Comparison between experiment and theory

This appendix contains supporting information with respect to Chapter 3, which studied the SubPc / C_{60} charge transfer process. I include additional experimental details, a discussion of laser fluence, and a description of the principal projection used in Chapter 3.

A.1 Additional experimental details

For the TRSHG experiments, a titanium-doped sapphire oscillator (Spectra-Physics® Mai Tai® SP) seeded a regenerative amplifier (Spectra-Physics® Spitfire® Pro) yielding 4 mJ, ∼40 fs pulses centered at 800 nm at 500 Hz. A portion of this beam formed the probe pulse. Another portion powered a home-built double-pass noncollinear optical parametric amplifier (NOPA) [1] forming the pump pulse, which for this experiment was tuned to 580 nm. A motorized delay stage controlled the relative time-delay between the pump and the probe pulses. The pulses interacted collinearly at the sample, with the sample oriented at 45 degrees. The beams were approximately 1 cm in diameter, which allowed for appreciable signal generation while maintaining the very low laser fluences re-

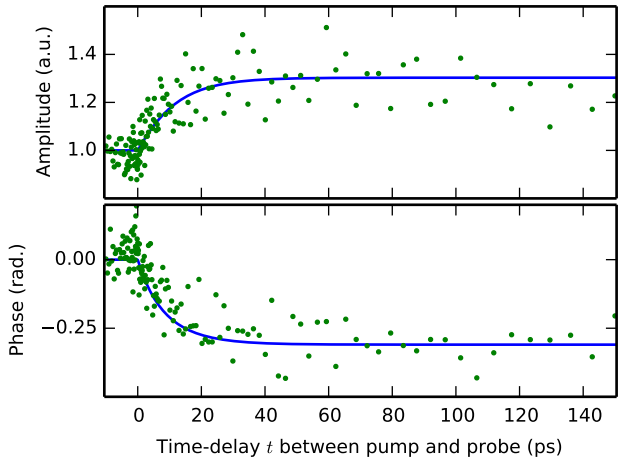

Figure A.1: Measured and fitted p-polarized hTRSHG data, showing the SHG amplitude and phase as a function of the time-delay t between pump and probe pulses. Amplitudes and phases are measured relative to the SHG before time zero. Green dots, measured data. Blue line, fitted single-exponential curve.

quired by these samples, as discussed later on. After the sample, the second-harmonic signal was linearly mixed with a reference field or local oscillator (LO) in order to perform heterodyne detection. The signal and LO were dispersed with a spectrometer (Horiba Jobin-Yvon iHR-320) and detected with a CCD (Princeton Instruments PIXIS-100B). The time resolution of this experiment was $\sim$200 fs as measured by a second-order cross-correlation between the pump and probe in a 10 μm thick beta barium borate (BBO) crystal placed at the sample position. This time resolution could easily be improved by compressing the pump pulse, but that was not done here to avoid compressor losses. The observed dynamics were much slower than the time resolution. Each TRSHG trace with a single probe polarization took about half an hour, with ten seconds of data averaging for each of 150 time-points. The time-points were spaced hyperbolically (following a hyperbolic sine function) so more points were close to time-zero than far from time-zero.

Three types of samples were prepared on an ultra-smooth c-cut sapphire wafer (Precision Micro-Optics LLC): a 3 nm film of SubPc capped by 20 nm of C_{60}, a neat 20 nm film of C_{60}, and a neat 3 nm film of SubPc. Films were deposited onto room-temperature substrates using vacuum thermal evaporation at a pressure below 5×10^{-7} Torr and at deposition rates of 1 Å/s and 0.5 Å/s for C_{60} and SubPc, respectively. Samples were encapsulated under a pure nitrogen atmosphere

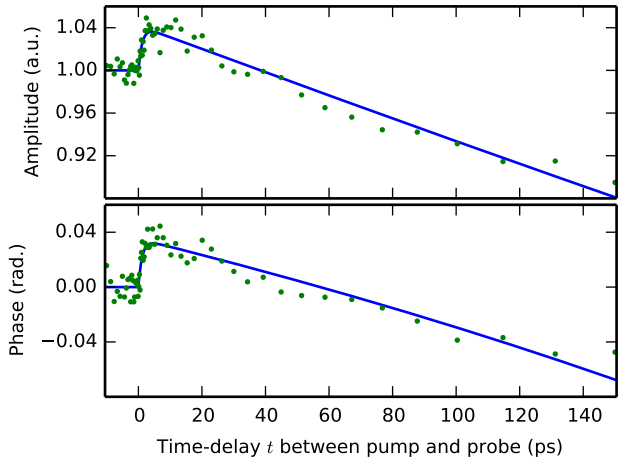

Figure A.2: Measured and fitted high-fluence *p*-polarized hTRSHG data, showing the SHG amplitude and phase as a function of the time-delay t between pump and probe pulses. Amplitudes and phases are measured relative to the SHG before time zero. Green dots, measured data. Blue line, fitted curve containing an exponential component ($k \sim 1\,\mathrm{ps}^{-1}$) and a linear component.

using a BK7 window and solvent-free UV-cured epoxy to prevent oxygen- and moisture-induced degradation. The layer of SubPc was extremely thin (∼3 nm) to prevent exciton diffusion from being a significant driver of the observed dynamics. I verified this by observing the same charge-transfer rate in both a 1.5 nm SubPc film and a 3 nm SubPc film, each capped with C_{60}.

For each trace, I measured a real and imaginary component to the signal at each time-point, corresponding to its amplitude and phase. For the present experiment, I did not "phase" the data, meaning there is an unknown phase between the measured signal and the second-order nonlinear susceptibility $\chi^{(2)}$, so only relative measured phases are meaningful rather than absolute phases. While absolute phases should provide for more meaningful comparisons against microscopic models of the interface, relative phases still provide a second data-point at every measured time-point, which aids in resolving the dynamics. Figure A.1 shows representative data, where I plot the measured amplitude and phase of the SHG signal as a function of the time-delay t between the pump and probe pulses, using a *p*-polarized probe pulse on a SubPC/C_{60} bilayer sample.

A.2 Laser fluence

I found that very low laser fluences were necessary to avoid higher-order processes such as exciton-exciton annihilation and laser-induced aging. For example, Figure A.2 shows a hTRSHG trace taken with higher laser fluence (10 μJ/cm^2 in the pump and 100 μJ/cm^2 in the probe) showing obviously-different dynamics as compared to the low-fluence data shown in Figure A.1. Figure A.2 shows both faster dynamics near time zero ($k \sim 1\,\text{ps}^{-1}$) and slower dynamics far from time zero, which I was not able to resolve with this experiment. I attribute the large slow component to the formation of long-lived triplet states after exciton-exciton annihilation. That is, two nearby excited SubPc molecules can undergo exciton-exciton annihilation via a variety of spin-allowed processes: $S_1 + S_1 \rightarrow S_2 + S_0 \rightarrow S_1 + S_0$, $S_1 + S_1 \rightarrow T_1 + T_1$, or even $S_1 + S_1 \rightarrow T_2 + T_1 \rightarrow T_1 + T_1$ depending on what the energy levels are. The triplet state T_1 is presumed to be long-lived; my experiments seem to indicate on the order of milliseconds. It is evident from Figure A.2 that the magnitude of the two-photon cross section associated with the triplet state(s) is very large, since the slowly-growing-in signal is so large and shows no signs of stopping within the range of this experiment. The faster dynamics near time zero also has the opposite sign of phase-change when compared to the low-fluence data, as seen in Figure A.1 compared to Figure A.2. The fast kinetics are therefore likely to be due to a fundamentally-different process than the low-fluence processes; I attribute the fast kinetics to absorption events starting from a pre-existing population of triplet states: $T_1 + h\nu \rightarrow T_2$.

As I decreased the laser fluence, the faster and slower kinetic components decreased, and could not be detected at the final pump fluence of 2 μJ/cm^2. I likewise reduced the probe fluence to 50 μJ/cm^2 to eliminate laser-induced aging in the film, as determined by the kinetics staying the same over multiple repetitions of the experiment in the same spot on the sample.

A.3 Description of the principal projection

I best-fit the data using a single-exponential model, with the same rate k for both polarizations:

$$S_i(t) = A_i + B_i\,\theta(t)\,\left[1 - \exp(-kt)\right]. \tag{A.1}$$

Here, $S_i(t)$ represents the measured complex hTRSHG signal as a function of polarization i and pump-probe relative time delay t. A_i represents the ground-state signal ($t < 0$) and B_i represents the change in SHG due to the presence of the pump, in the limit of large t. Both A_i and B_i are complex and depend on the polarization i. $\theta(t)$ is the Heaviside step function. k is the (real) rate constant of the process, and does not depend on polarization. The unknowns in the fit were A_i, B_i, and k. The measured data and their fits are plotted using the principal projection $\mathcal{P}$ of the data onto the $\vec{A}$–$\vec{B}$ line—essentially, the first principal component of the data—where $\vec{A}$ and $\vec{B}$ are the four-component vectors

$$\vec{A} = \begin{bmatrix} \mathrm{Re}\,\{A_1\} \\ \mathrm{Im}\,\{A_1\} \\ \mathrm{Re}\,\{A_2\} \\ \mathrm{Im}\,\{A_2\} \end{bmatrix}, \qquad \vec{B} = \begin{bmatrix} \mathrm{Re}\,\{B_1\} \\ \mathrm{Im}\,\{B_1\} \\ \mathrm{Re}\,\{B_2\} \\ \mathrm{Im}\,\{B_2\} \end{bmatrix}.$$

Mathematically, what is plotted is $\mathcal{P}(t) = \hat{B} \cdot (\vec{S}(t) - \vec{A})/\|\vec{B}\|$ where $\|\cdot\|$ is the Euclidean norm and $\hat{B} = \vec{B}/\|\vec{B}\|$ is the normalized (unit) vector. This projection starts at 0 before time-zero, and converges to 1 in the limit of large pump-probe time-delay. I found that this projection captured the majority of the information in the data; the data-components orthogonal to this projection were dominated by noise.

References

[1] E. Riedle, M. Beutter, S. Lochbrunner, J. Piel, S. Schenkl, S. Spörlein, and W. Zinth. Generation of 10 to 50 fs pulses tunable through all of the visible and the NIR. *Applied Physics B*, **71**:457–465, (2000).

APPENDIX B

Choice of chirp-scanning range for the SPEAR method

In the SPEAR method, the numbers $\phi_2^{(i)}$ define the applied pulse-shapes used to measure the spectral phase. They should be chosen so that the second derivative of the total phase $\varphi''(\omega) + \phi_2^{(i)}$ is far from zero over the whole spectral range. In the case where the pulse is close to compressed, then $|\phi_2| \gg \tau_{\text{TL}}^2$ is usually a good choice, where τ_{TL} is the compressed (transform-limit) pulse duration. In many situations, a simple scan of quadratic phase makes the pulse at least roughly compressed so this condition is relatively easy to meet. However, if the higher-order phase terms are particularly strong then some experimentation may be necessary to get $\phi_2^{(i)}$ right. I often have ~ 12 to ~ 30 fs pulses, and to compress them I typically use two or four values of ϕ_2, on the order of $\pm 2\tau_{\text{TL}}^2$, after doing a coarse compression. I find in practice that this is sufficiently larger than τ_{TL}^2 for most cases.

More generally, the magnitude of ϕ_2 defines a spectral resolution because in a time-frequency picture only a bandwidth of order $1/\sqrt{|\phi_2|}$ will be available for sum-frequency-generation at any point in time. In many experimental situations, only the second- and third-order spectral phase functions are appreciable, and so relatively low spectral resolution compared to the spectral bandwidth is required and therefore relatively small values of ϕ_2 are needed as compared to τ_{TL}^2. In other situations that exhibit significant ripple in the group-delay dispersion (in the presence of chirped mirrors, for example), a higher amount of spectral resolution may be required, so that ϕ_2 is dictated by the spectral bandwidth between ripples rather than the spectral bandwidth of the pulse.

APPENDIX C

Details of the computational simulation comparing several pulse compression methods

For the computer simulation used in Chapter 6, the action of a pulse-shaper was simulated by multiplying the spectral field by a complex spectral filter with absolute value no greater than one. To simulate second-harmonic-generation, the fields were Fourier-transformed to the time domain, squared, Fourier-transformed back into the frequency domain, and multiplied by a spectral filter to take into account the finite phasematching bandwidth of a 10 micron BBO as pictured in Figure C.1. There were then losses from mirrors, the spectrometer slit, the 600 groove/mm spectrometer grating, and the finite quantum efficiency of the CCD. There was spectrometer blurring to approximate a 50-micron slit, and discretization onto a 1340-pixel CCD with 20-micron pixels to approximate the experimental camera. Shot noise and read noise (11 photoelectron standard deviation) were added, again approximating the experimental camera. For comparison, the intensity of a transform-limited pulse's SHG was about 1400 photoelectrons at the peak. Since the camera detects linearly in wavelength, the noisy data were resampled back into the frequency domain, taking into account the varying frequency width of the pixels. The resulting data were analyzed using the published methods, with the exception of the FROG data and the chirp-scan data which were analyzed using an algorithm described below.

To compute the spectral filter associated with the finite phasematching bandwidth of a 10 mi-

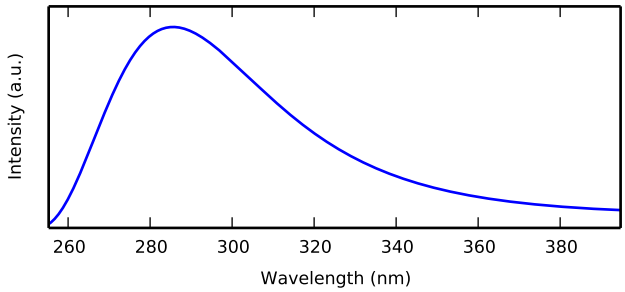

Figure C.1: Intensity of the spectral filter associated with the finite phasematching bandwidth of a 10-micron-thickness BBO crystal, cut at 42 degrees. The cut angle was chosen to ensure there was appreciable amplitude over the full second-harmonic laser bandwidth.

cron BBO, I started with the nonlinear wave equation:

$$\frac{\partial^2}{\partial x^2}\mathbf{E} - \frac{n^2}{c^2}\frac{\partial^2}{\partial t^2}\mathbf{E} = \frac{\chi^{(2)}}{c^2}\frac{\partial^2}{\partial t^2}\mathbf{E}^2. \tag{C.1}$$

Using peturbation theory, I assumed the second-harmonic light is small and does not affect the first-harmonic light, and the first-harmonic light propagates essentially linearly, and the light only propagates in the x-direction defined as normal to the BBO, yielding separate wave equations for the first-harmonic and second-harmonic. Assuming pure polarization of both first and second harmonics leads to a scalar form of these equations:

$$\frac{\partial^2}{\partial x^2}E_{\text{1st}} - \frac{n^2}{c^2}\frac{\partial^2}{\partial t^2}E_{\text{1st}} = 0; \tag{C.2}$$

$$\frac{\partial^2}{\partial x^2}E_{\text{2nd}} - \frac{n^2}{c^2}\frac{\partial^2}{\partial t^2}E_{\text{2nd}} = \frac{\chi^{(2)}}{c^2}\frac{\partial^2}{\partial t^2}E_{\text{1st}}^2. \tag{C.3}$$

The simulation represented fields F in units of $\sqrt{\text{nJ/fs}}$ in the time domain, with a separate spot size σ so

$$E\left(x,y,z,t\right) = F\left(x,t\right)\frac{1}{\sqrt{2\pi}\sigma}\exp\left(-\frac{y^2+z^2}{4\sigma^2}\right). \tag{C.4}$$

Since the BBO is only 10 microns thick, there is negligible group-velocity dispersion of the first-harmonic, leading to the following solution of the wave equations, transforming first-harmonic F

to second-harmonic F:

$$F_{\text{2nd}}(x,\omega) = \frac{\chi^{(2)}\omega}{4n(\omega)c}\frac{1}{\sqrt{2\pi}\sigma}\frac{\exp\left(-iT\left(-k(\omega)+\omega/v_g-2\omega_0^2\,\frac{dn}{d\omega}\big|_{\omega_0}/c\right)\right)-1}{\left(-k(\omega)+\omega/v_g-2\omega_0^2\,\frac{dn}{d\omega}\big|_{\omega_0}/c\right)}\int dt\, e^{-i\omega t}F_{\text{1st}}^2(t) \quad \text{(C.5)}$$

This defined the spectral filter associated with a 10-micron-thick BBO, pictured in Figure C.1. Here, T is the BBO thickness, ω_0 is the central frequency of the first-harmonic light, v_g is the group velocity of the first-harmonic light, ω is the second-harmonic frequency, $n(\omega)$ is the index of refraction of the second-harmonic light, $\frac{dn}{d\omega}\big|_{\omega_0}$ is the derivative of the index of refraction of the first-harmonic light, evaluated at ω_0, and $k(\omega)$ is $\omega n(\omega)/c$, the angular wavenumber corresponding to the frequency ω. $\chi^{(2)}$ is represented in units of nm/$\sqrt{\text{nJ/fs}}$. According to Shoji et al. [1], the effective nonlinearity in the phase-matched direction for 650 nm light in BBO is approximately $d_{\text{eff}} = 2$ pm/V, which after change of units is 40 nm/$\sqrt{\text{nJ/fs}}$.

The FROG and chirp-scan data were analyzed using a general direct-fitting algorithm that minimized a weighted least-squares objective function $\mathcal{L}$.

$$\mathcal{L} = \int d\omega \sum_i R_{i,\,\text{weighted}}^2(\omega) \quad \text{(C.6)}$$

$$R_{i,\,\text{weighted}}(\omega) = \frac{1}{n_{\text{estimate}}^{(i)}(\omega)}\left[I_{\text{measured}}^{(i)}(\omega) - V_i(\omega)\right] \quad \text{(C.7)}$$

$$V_i(\omega) = U_i(\omega)\,U_i^*(\omega) \quad \text{(C.8)}$$

$$U_i(\omega) = \mathcal{F}_{t\to\omega}\left\{T_i^2(t)\right\} \quad \text{(C.9)}$$

$$T_i(t) = \mathcal{F}_{\omega\to t}^{-1}\left\{S_i(\omega)\,E(\omega)\right\} \quad \text{(C.10)}$$

Here, $R_{i,\,\text{weighted}}^2(\omega)$ is a residual comparing the measured data $I_{\text{measured}}^{(i)}(\omega)$ to the computed result $V_i(\omega)$, weighted by an estimate of the noise $n_{\text{estimate}}^{(i)}(\omega)$ (both read noise and shot noise). The unknown spectral filter imposed by the BBO was ignored, but that did not significantly affect

the accuracy of reconstruction. $V_i(\omega)$ is the second-harmonic spectral intensity of pulse-shape i. $U_i(\omega)$ is the second-harmonic spectral field of pulse-shape i. T_i is the time-domain of pulse-shape i. $S_i(\omega)$ is the known complex spectral filter (amplitude and phase) imposed by the pulse-shaper. $E(\omega)$ is the current estimate of the complex field to be measured. The free parameters are the values $E(\omega)$. It is straightforward to analytically differentiate this objective function with respect to the unknowns; this speeds the minimization.

The actual minimization of the objective function was performed using the L-BFGS-B algorithm [2] implemented in the open-source `scipy.optimize` module [3]. The starting points for minimization were random pulses, roughly localized in both time and frequency. I did not use CRT or SPEAR to provide starting points to the minimization algorithm for chirp-scan because none of the applied chirps were far-field. The minimization was performed from multiple initial guesses to ensure convergence to the global minimum. The minimization was performed in two stages: first the above objective function was minimized, and that provided the initial guess to a slightly different objective function that allowed for an unknown Gaussian spectral filter, as a coarse approximation to the BBO's SHG efficiency curve. Once the nonlinear minimizer found the least-squares estimate of $E(\omega)$, the spectral phase of this field was smoothed and then differentiated to yield spectral group-delay.

References

[1] Ichiro Shoji, Hirotaka Nakamura, Keisuke Ohdaira, Takashi Kondo, Ryoichi Ito, Tsutomu Okamoto, Koichi Tatsuki, and Shigeo Kubota. Absolute measurement of second-order nonlinear-optical coefficients of β-BaB_2O_4 for visible to ultraviolet second-harmonic wavelengths. *Journal of the Optical Society of America B*, **16**:620, (1999).

[2] Richard H. Byrd, Peihuang Lu, Jorge Nocedal, and Ciyou Zhu. A Limited Memory Algorithm for Bound Constrained Optimization. *SIAM Journal on Scientific Computing*, **16**:1190–1208, (1995).

[3] The Scipy community. Optimization and root finding (scipy.optimize). URL `http://docs.scipy.org/doc/scipy/reference/optimize.html`.